TU Delft

Delft University of Technology

Flocculation and deep-sea mining plumes

Ali, W.

DOI
10.4233/uuid:155b3071-c74c-4296-9dd2-512ccb2e1006

Publication date
2024

Document Version
Final published version

Citation (APA)
Ali, W. (2024). *Flocculation and deep-sea mining plumes*. [Dissertation (TU Delft), Delft University of Technology]. https://doi.org/10.4233/uuid:155b3071-c74c-4296-9dd2-512ccb2e1006

Important note
To cite this publication, please use the final published version (if applicable).
Please check the document version above.

Copyright
Other than for strictly personal use, it is not permitted to download, forward or distribute the text or part of it, without the consent of the author(s) and/or copyright holder(s), unless the work is under an open content license such as Creative Commons.

Takedown policy
Please contact us and provide details if you believe this document breaches copyrights.
We will remove access to the work immediately and investigate your claim.

This work is downloaded from Delft University of Technology.
For technical reasons the number of authors shown on this cover page is limited to a maximum of 10.

FLOCCULATION AND DEEP-SEA MINING PLUMES

FLOCCULATION AND DEEP-SEA MINING PLUMES

Dissertation

for the purpose of obtaining the degree of doctor
at Delft University of Technology
by the authority of the Rector Magnificus
Prof.dr.ir. T.H.J.J. van der Hagen
chair of the Board for Doctorates
to be defended publicly on
Thursday 16 May 2024 at 12:30 o'clock

by

Waqas ALI

Master R STS I MEI / Simulation and lnstrumentation in Mechanics,
University Grenoble Alpes, Grenoble, France,

born in Rawalpindi, Pakistan.

This dissertation has been approved by the promotors.

Composition of the doctoral committee:

Rector Magnificus,	chairperson
Dr. C. Chassagne,	Delft University of Technology, promotor
Dr. A. Kirichek,	Delft University of Technology, copromotor

Independent members:

Prof. dr. A.J. Manning,	University of Plymouth
Dr. J. Spearman,	HR Wallingford, UK
Prof. dr. it. M. van Koningsveld,	Delft University of Technology
Prof. dr. ir. T. Hoitink,	Wageningen University & Research
Prof. dr. ir. Z. Wang,	Delft University of Technology, reserve member

This research is funded by NWO and industrial partners and carried out within the framework of the MUDNET academic network.

Keywords: Flocculation; Plumes; Turbidity current; Floc size; Settling velocity; Organic matter

Printed by: Gildeprint B.V.

Cover picture by: Waqas Ali

Copyright © 2024 by W. Ali

ISBN 978-94-6366-859-0

An electronic version of this dissertation is available at http://repository.tudelft.nl/.

To the people who cherished my success
My uncle: Iftikhar Ali Malik (Late)
My friend and brother: Mujtaba Haider (Late)

CONTENTS

Summary xi

Samenvatting xiii

1 Introduction 1
- 1.1 Problem statement . . . 2
  - 1.1.1 Deep sea mining . . . 3
  - 1.1.2 Polymetallic nodule mining . . . 3
  - 1.1.3 Mining technology for the deep sea . . . 4
  - 1.1.4 Sediment plumes and turbidity currents . . . 6
  - 1.1.5 Deep sea sediment . . . 8
- 1.2 Flocculation in plumes and turbidity currents . . . 11
- 1.3 Research questions and Thesis outline . . . 12

2 Methods 15
- 2.1 Introduction . . . 16
  - 2.1.1 Floc creation . . . 16
  - 2.1.2 Floc sizes . . . 16
- 2.2 Set-ups for floc creation . . . 17
  - 2.2.1 Lock exchange setup . . . 17
  - 2.2.2 Jar experiments . . . 17
  - 2.2.3 Rotating wheel . . . 18
- 2.3 Floc size and settling measurements . . . 18
  - 2.3.1 Malvern: Particle size distribution . . . 18
  - 2.3.2 FLOCCAM: Floc size and settling analysis . . . 19
  - 2.3.3 Safas . . . 20

3 Flocculation in turbidity currents 23
- 3.1 Introduction . . . 24
- 3.2 Material and experimental methods . . . 26
  - 3.2.1 Clay . . . 26
  - 3.2.2 Flocculant . . . 26
  - 3.2.3 Water . . . 27
- 3.3 Results and discussion . . . 28
  - 3.3.1 Distance travelled by plume heads . . . 28
  - 3.3.2 Mean floc size as function of travel distance . . . 29
  - 3.3.3 Settling velocity distributions as function of size and travel distance . . . 30
- 3.4 Conclusions . . . 31

4 Effect of the concentration on settling velocity of flocs **35**
4.1 Introduction . . . 36
4.2 Material and experimental methods . . . 37
4.2.1 Clay . . . 37
4.2.2 Flocculant . . . 38
4.2.3 Water . . . 38
4.3 Results and discussion . . . 38
4.3.1 Individual vs collective settling . . . 38
4.3.2 Clay Concentration dependence . . . 40
4.4 Conclusions . . . 41

5 Flocculation and settling of deep-sea clay from the Clarion Clipperton Fracture Zone **43**
5.1 Introduction . . . 44
5.2 Material and experimental methods . . . 45
5.2.1 Clay . . . 45
5.2.2 Flocculation experiments in a jar . . . 45
5.2.3 Shear cycle experiments . . . 47
5.2.4 Residence time at the bottom of the jar . . . 47
5.2.5 Rotating wheel experiment . . . 47
5.3 Results and discussion . . . 48
5.3.1 Influence of mixing time and concentration . . . 48
5.3.2 Shear cycle experiments . . . 50
5.4 Conclusions . . . 53

6 Towards implementation of flocculation in numerical modeling **57**
6.1 Introduction . . . 58
6.2 Theory . . . 60
6.2.1 Logistic growth model (LG Model) . . . 60
6.2.2 Smoluchowski model (S model) . . . 61
6.2.3 Comparison between models . . . 66
6.3 Material and experimental methods . . . 68
6.3.1 Clay . . . 68
6.3.2 Flocculant . . . 68
6.4 Results and discussion . . . 68
6.4.1 Flocculation kinetics . . . 68
6.4.2 Dependence on clay concentration . . . 70
6.4.3 Dependence on shear . . . 73
6.5 Conclusions . . . 74

7 Conclusions and Recommendations **77**
7.1 Conclusions . . . 78
7.1.1 Effect of flocculation on turbidity flow . . . 78
7.1.2 Effect of concentration on the evaluation of a particle's settling velocity in turbidity currents . . . 79

7.1.3 Effect of clay concentration, shear rates and floc rest time on flocculation of deep-sea clay collected from Clarion Clipperton zone 80
7.1.4 Parametrization of Flocculation models 81
7.2 Summary and recommendations 81

A Appendix A **83**

B Appendix B **89**

C Appendix C **93**

D Appendix D **99**

References **103**

Acknowledgements **117**

Curriculum Vitæ **121**

List of Publications **123**

SUMMARY

Deep-sea mining Industry and academia are presently investigating the potential of deep-sea mining for valuable resources such as poly-metallic nodules. Nevertheless, the process of manoeuvring, excavating, and processing these resources poses a threat to the deep-sea environment through the generation of plumes of suspended fine-grained solids, which have the potential to damage benthic fauna by smothering or burying them. Assessing the impact of plumes requires an understanding of how far they disperse through bottom currents and how their suspended loads change over time. The affected area may be overestimated by current numerical simulations as they neglect the crucial process of flocculation, whereby fine particles aggregate into larger and faster-sinking clumps. The effect of flocculation on plume dispersion is still not well comprehended, engendering ambiguity in monitoring techniques dependent on optronic and acoustic sensors that are sensitive to particle size but do not take into account flocculation. To tackle these concerns, it is essential to undertake research that centres on studying flocculation characteristics in marine sediments. This includes carrying out controlled laboratory experiments to gain a better understanding of the critical conditions for flocculation. Additionally, it involves scaling up these experiments to replicate real-world plume dispersion and devising precise measuring methods for flocculated particle suspensions. This thesis focuses only on benthic sediment plumes.

In the course of this work, laboratory experiments were conducted to gain a better understanding of the impact of flocculation on turbidity currents, focusing on clays that are representative of deep-sea mining areas. Turbidity currents were generated in a lock exchange and the results are presented in Chapter 3. The study's findings however are quite generic and might be applied to other types of fluid flows, such as sediment plumes created during dredging activities. The experiments were specifically focused on the influence of salt and organic material as flocculant agents. The experiments demonstrated that the presence of organic matter resulted in flocculation within a short amount of time, leading to decreased current propagation and notable changes in both floc sizes and settling velocities.

The impact of particle concentration on floc size and settling velocity was investigated using a high-magnification digital video camera with a settling column. An important question was how much settling velocities of individual particles would differ when compared to batch settling. Anionic polyelectrolyte in combination with illite clay was used at various clay concentrations in these experiments, at a given flocculant to clay ratio. Experiments demonstrated that the average settling velocity of flocs is strongly dependent on the concentration of transferred flocs. Although the same flocculant to clay ratio was used and mixing time was kept constant (enabling particle sizes to reach steady-state), the size of flocs and their settling velocity differed with clay concentration.

Elevated clay concentrations yielded larger flocs. The reason is linked to flocculation kinetics, as described in Chapter 4.

In Chapter 5, laboratory experiments are presented regarding the flocculation ability of deep-sea clay samples collected from two different regions of the Clarion Clipperton Fracture Zone (CCFZ). The findings indicated that the clay particles aggregated into larger flocs in a brief period of 2.5 minutes, ranging from 50 to 150 microns, and up to 500 microns due to the presence of natural organic matter. The study also reveals that at high shear (larger than 125 s^{-1}) an increase in floc sizes with shear is observed, while below that threshold floc sizes would decrease with increasing shear. This peculiar behaviour of floc size as a function of shear was attributed to the hydrophobic (surfactant) nature of organic matter. This feature of organic matter could also explain the dynamic particle size changes observed in resting-time behaviour experiments.

In Chapter 6, two flocculation models were compared, which describe the time evolution of floc size. One model (LG) is based on logistic growth theory while the other one (S model) originates from Smoluchowski's theory. It was shown that these models exhibit different flocculation kinetics. Through a series of laboratory experiments where the flocculation of mineral clay by polyelectrolyte was studied as a function of clay concentration and shear rate, it was found that the LG model effectively replicates the observed time-dependent floc sizes, unlike the S model. The LG model was subsequently parameterized and could serve as input to a sediment transport model.

SAMENVATTING

Vanuit de diepzeemijnbouwindustrie en de academische wereld wordt momenteel onderzoek gedaan naar het potentieel van diepzeemijnbouw voor de winning van waardevolle bronnen, zoals polymetallische nodules. Het proces van manoeuvreren, uitgraven en verwerken van dit materiaal vormt echter een bedreiging voor het diepzeemilieu doordat pluimen van fijnkorrelig materiaal ontstaan, die de bentische fauna kunnen beschadigen via verstikking of begraving. Het beoordelen van de impact van pluimen vereist inzicht in hoe ver ze zich verspreiden door bodemstromingen en hoe hun eigenschappen in de loop van de tijd veranderen. Het getroffen gebied van de pluimen kan overschat worden door de huidige numerieke simulaties, omdat ze het cruciale proces van flocculatie verwaarlozen, waarbij fijne deeltjes samenklonteren tot grotere, en sneller zinkende, klonten. Het effect van vlokvorming op de verspreiding van pluimen wordt nog steeds niet goed begrepen. Dit leidt tot onduidelijkheid in monitoringtechnieken die afhankelijk zijn van optronische en akoestische sensoren die gevoelig zijn voor de grootte van de deeltjes, maar geen rekening houden met flocculatie. Om deze problemen aan te pakken, is het essentieel om onderzoek te doen dat zich richt op het bestuderen van flocculatie eigenschappen in mariene sedimenten. Dit omvat het uitvoeren van gecontroleerde experimenten om een beter begrip te krijgen van de kritische parameters voor flocculatie. Daarnaast moeten deze experimenten worden opgeschaald om de verspreiding van pluimen in de echte wereld na te kunnen bootsen en moeten nauwkeurige meetmethoden worden ontwikkeld voor het meten van suspensies van samengeklonterde deeltjes. Dit proefschrift richt zich alleen op bentische sedimentpluimen.

In de loop van dit werk zijn laboratoriumexperimenten uitgevoerd om een beter begrip te krijgen van de invloed van flocculatie op turbiditeitstromen, waarbij de nadruk lag op klei die representatief is voor diepzeemijnbouwgebieden. De turbiditeitstromen werden opgewekt in een zogenaamde “lock-exchange” en de resultaten hiervan zijn gepresenteerd in Hoofdstuk 3. De bevindingen van het onderzoek zijn echter vrij algemeen en kunnen worden toegepast op andere soorten vloeistofstromen, zoals sedimentpluimen die ontstaan tijdens baggerwerkzaamheden. De experimenten waren specifiek gericht op de invloed van zout en organisch materiaal als vlokmiddel. De experimenten toonden aan dat de aanwezigheid van organisch materiaal resulteerde in vlokvorming binnen een korte tijd, wat leidde tot opmerkelijke veranderingen in zowel vlokgrootte als bezinkingssnelheden. Met als effect een verminderde verspreiding van de pluimen.

De invloed van de deeltjesconcentratie op de vlokgrootte en bezinkingssnelheid werd onderzocht met behulp van een bezinkkolom en digitale videocamera met een hoge vergroting. Een belangrijke vraag was in hoeverre de bezinkingssnelheden van individuele deeltjes zouden verschillen in vergelijking met bezinking in groepen. In deze experimenten werd anionisch polyelektrolyt in combinatie met illietklei gebruikt bij verschillende

kleiconcentraties en een gegeven verhouding tussen vlokmiddel en klei. De experimenten toonden aan dat de gemiddelde bezinkingssnelheid van vlokken sterk afhangt van de concentratie van overgedragen vlokken. Hoewel dezelfde verhouding vlokmiddel-klei werd gebruikt en de mengtijd constant werd gehouden (zodat de deeltjesgrootte de stationaire toestand kon bereiken), verschilde de grootte van de vlokken en hun bezinkingssnelheid afhankelijk van de kleiconcentratie. Verhoogde kleiconcentraties resulteerden in grotere vlokken. De reden hiervoor is gekoppeld aan de vlokkinetiek, zoals beschreven in Hoofdstuk 4.

In Hoofdstuk 5 worden laboratoriumexperimenten gepresenteerd met betrekking tot het flocculatie vermogen van diepzeekleimonsters uit twee verschillende gebieden van de Clarion Clipperton Breukzone (CCFZ). De bevindingen gaven aan dat de kleideeltjes samenklonterden tot grotere vlokken in een korte periode van 2,5 minuten, variërend van 50 tot 150 micron, en tot 500 micron door de aanwezigheid van natuurlijk organisch materiaal. Het onderzoek toont ook aan dat bij hoge shearing (groter dan $125\,s^{-1}$) een toename in vlokgrootte met shearing wordt waargenomen, terwijl onder die drempelwaarde de vlokafmetingen afnemen met toenemende afschuiving. Dit vreemde gedrag van vlokgrootte als functie van afschuiving werd toegeschreven aan de hydrofobe (oppervlakteactieve) aard van organisch materiaal. Deze eigenschap van organisch materiaal zou ook de dynamische veranderingen in de deeltjesgrootte die werden waargenomen in experimenten met rusttijden.

In Hoofdstuk 6 werden twee vlokmodellen vergeleken die de evolutie van vlokgrootte door de tijd beschrijven. Het ene model (LG) is gebaseerd op de logistische groeitheorie, terwijl het andere model (S-model) is gebaseerd op de theorie van Smoluchowski. Er werd aangetoond dat deze modellen verschillende flocculatiekinetiek vertonen. Door middel van een reeks laboratoriumexperimenten waarbij de flocculatie van minerale klei door polyelektrolyt werd bestudeerd als functie van de kleiconcentratie en afschuifsnelheid, werd gevonden dat het LG-model de waargenomen tijdsafhankelijke vlokafmetingen reproduceert, in tegenstelling tot het S-model. Het LG-model werd vervolgens geparametriseerd en kon dienen als input voor een sedimenttransportmodel.

1

INTRODUCTION

The chapter introduces key concepts crucial in the context of deep-sea mining: deep-sea organic matter, sediment, polymetallic nodule mining, mining technology, sediment plumes, turbidity currents, and flocculation. It explores the composition of deep-sea organic matter and sediment layers while delving into mining technologies and the environmental impact of sediment plumes and turbidity currents. Additionally, the concept of flocculation in deep-sea contexts is elucidated. This chapter establishes the foundation for the thesis, with definitions, a literature review, and an outline for subsequent discussions.

1

1.1. PROBLEM STATEMENT

Over the past few decades, the global demand for metals and rare earth elements has experienced a remarkable surge. This growth can be attributed to several factors, including the rapid expansion of economies, advancements in technology, the push for green energy solutions, and the ongoing development of civilizations (Beyond-mining, 2011; Hein et al., 2020).

In 2015, the United Nations Climate Change Conference marked a crucial milestone with the unanimous approval of the "Paris Agreement". This landmark international treaty established legally binding commitments to combat climate change and laid the foundation for global climate action. Embracing the Paris Agreement, the European Union (EU) set an ambitious target of going climate-neutral by 2050 to fulfil its obligations. By the year 2030, the EU aims to generate at least 32.5% of its energy from renewable sources. To accomplish this, the EU strategically focuses on developing renewable energy sources while being faced with the challenges of harnessing the essential raw materials necessary for clean technology development.

In this context, the utilization of vital raw materials such as lithium, cobalt, and rare earth metals becomes essential. These elements play a pivotal role in developing renewable technologies, including wind turbines, electric vehicles, and solar panels, which are crucial for sustainable energy solutions (European Commission et al., 2018).

However, the increasing demand for these critical raw materials comes with a downside, as the diversity of their supply diminishes. Even though prudent resource management and sustainable extraction practices are crucial in ensuring a steady and reliable supply (Ragonnaud, 2023), there is an escalating demand for metals, which has placed immense pressure on the global supply chain, depleting terrestrial deposits in the process. Consequently, extracting these metals has become more arduous and costly, leading to a host of issues like skyrocketing prices, supply shortages, and heightened competition for resources. These challenges have prompted a growing interest in exploring unconventional sources that could potentially offer access to new reservoirs of vital raw materials.

One such promising source is the deep sea, known to hold a wealth of metals like cobalt, nickel, manganese, and other valuable minerals (Wedding et al., 2015). The estimated resources of critical mineral deposits, such as nickel and cobalt, in certain parts of the abyssal ocean, particularly the Clarion-Clipperton Fracture Zone (CCFZ) in the Pacific Ocean, surpass global land-based reserves by multiple times (Hein et al., 2020). For this reason, industries and countries are now turning to enriched mineral deposits in the deep-sea environment as a potential solution (Hein and Koschinsky, 2014; Wedding et al., 2015).

The extraction of minerals from the ocean floor is done by deep-sea mining (DSM). It is a relatively new and rapidly evolving industry, and it is seen by some as controversial and complex, involving potential environmental risks and uncertainties linked, for instance, to the spreading of sediment plumes and density currents (Kaiser et al., 2013; Peacock and Alford, 2018). This thesis aims to provide a better understanding of the chemo-physical processes occurring in sediment plumes and density currents during their propagation.

1.1.1. DEEP SEA MINING

Similar to the terrestrial landscape, the seabed displays a complex and diverse terrain, having a wide array of topographic features and geological structures. Three potential resources (Figure 1.1) with significant economic potential are under consideration for extraction (Boschen et al., 2013; Hein and Koschinsky, 2014; Hein and Petersen, 2013; Miller et al., 2018; Sharma, 2017): ferromanganese crusts on seamounts, massive sulfides beneath hydrothermal vents, and polymetallic nodules on the seafloor (the focus of this PhD thesis). In all three cases, mineral ore is obtained using operational vehicles or a combination of vehicles, which are then lifted to the surface through a vertical transport system. An operational vessel handles the mineral ore at the ocean surface and may perform preliminary preparations before shipping it to a land-based processing facility. In some cases, there might be a return water discharge into the ocean. The main difference between the three types of mining lies in the nature of the mineral-gathering activity. For polymetallic nodules, which are centimetre-scale concretions found partially buried in the seabed at depths of around 5,000 meters, a collector vehicle system is used to pick up the nodules from the abyssal plain while minimizing disturbance and resuspension of the upper sediment layer in which they are located. For seafloor massive sulfide deposits around hydrothermal vents, a more direct form of mining is required to remove overburden and extract buried ores. When it comes to cobalt crusts, the machinery needs to operate on the seamount's slopes and extract the desired crust which are centimetre-thick metallic layers that form on the flanks, and sometimes the summits, of submarine volcanoes (WOR, 2014; Yeo et al., 2019). Over the past seven decades, the extraction of marine minerals from the deep sea has been a subject of extensive research and development. However, in the last decade, interest in this field has surged significantly (Hein and Koschinsky, 2014; Miller et al., 2021; Miller et al., 2018).

1.1.2. POLYMETALLIC NODULE MINING

The exploration conducted during the HMS Challenger expedition in 1868 led to the discovery of polymetallic nodules. Polymetallic nodules (Figure 1.2), which are abundant in metals and rare earth elements, are located on the surface of abyssal plains in the oceans, typically at depths ranging from 4 to 6 km. Over millions of years, these formations are created through the precipitation of minerals from seawater, gradually accumulating around a central nucleus, which could be a rock or a shell fragment. They are marine concretions which range from 1-12 cm (Kuhn et al., 2017). On average, polymetallic nodules exhibit a slow growth rate of 10 – 20 mm per million years (Kuhn et al., 2017), rendering them one of the slowest geological formations found on Earth. Among the most extensive known nodule deposits, significant findings have been made in the CCFZ within the Pacific Ocean and the Indian Ocean Nodule Field. The northeast equatorial Pacific, specifically the CCFZ, is believed to have around 21 billion dry tons of polymetallic nodules (Hein et al., 2020). These nodules are known to contain over 6 billion dry metric tons of valuable metals like manganese, nickel, copper, and cobalt (Petersen et al., 2016). The finding of these nodules in the CCFZ and other deep-sea floor regions has sparked significant interest in the possibility of DSM operations to extract these valuable minerals.

The extraction of polymetallic nodules poses a significant challenge in developing technology that can efficiently and cost-effectively retrieve these minerals from the seabed

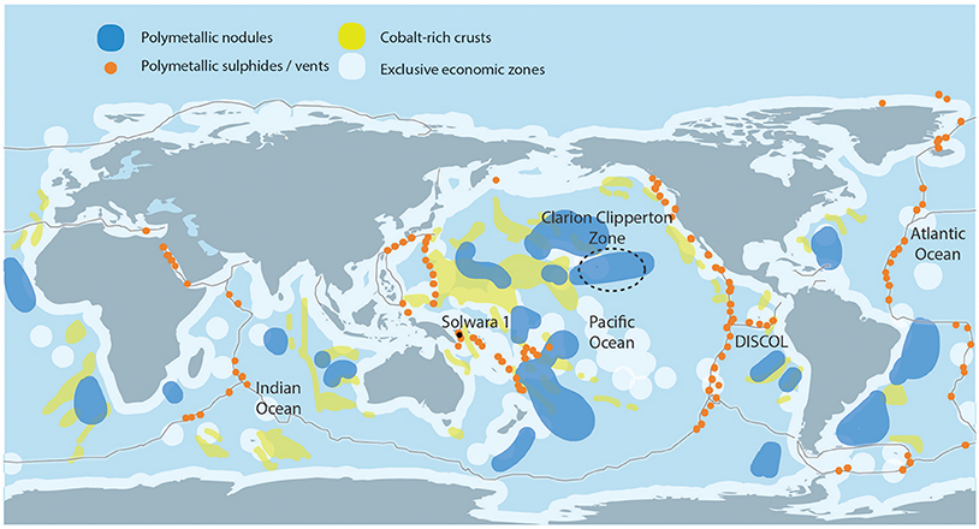


Figure 1.1: On the world map, the locations of the three primary marine mineral deposits are displayed with distinctive colours: polymetallic nodules (blue), polymetallic or seafloor massive sulfides (orange), and cobalt-rich ferromanganese crusts (yellow) (Miller et al., 2018).

while minimizing environmental impact. Specialized equipment and techniques must be developed to ensure safe and precise extraction.

To address these challenges and, in particular, study the environmental impact of sediment plumes, various companies and research institutes worldwide are collaborating to create the necessary technology and expertise for mineral extraction. Their collective efforts aim to innovate new solutions, reduce production costs, enhance efficiency, and mitigate environmental impact.

The primary focus of interest in mining marine minerals lies in international waters, creating a necessity to regulate DSM operations in these regions. In response to this need, the International Seabed Authority (ISA) was established as an intergovernmental organization responsible for managing, regulating, and overseeing all mineral-related activities in the international seabed area. This mandate is driven by the goal of benefiting humanity, as outlined by countries that have signed the United Nations Convention on the Law of the Sea (UNCLOS).

Since 2001, the ISA has entered into contracts with 29 contractors to explore deep-sea minerals, including polymetallic nodules. These contractual arrangements play a pivotal role in advancing the understanding and responsible extraction of valuable resources from the ocean floor.

1.1.3. MINING TECHNOLOGY FOR THE DEEP SEA

The two main methods for extracting minerals from the ocean floor are seabed mining and subsea mining. Seabed mining involves dredging the ocean floor with large machines,

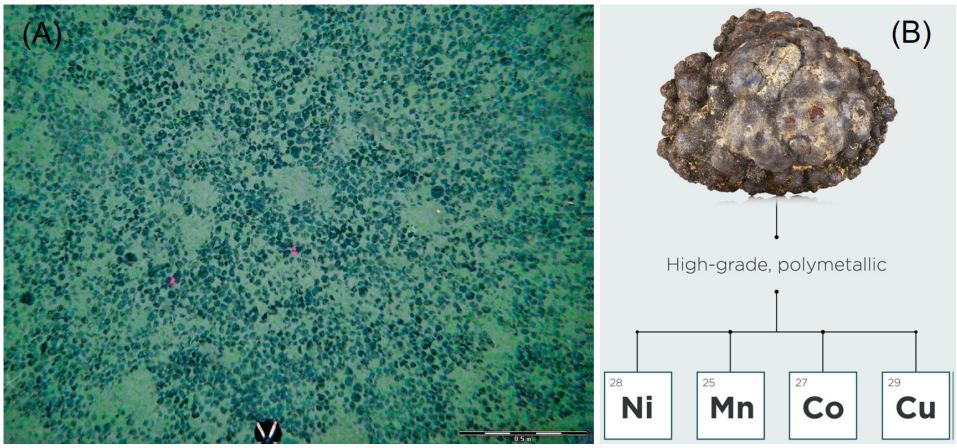


Figure 1.2: (A) This is a close-up view of a polymetallic nodule resting on the seafloor of the Pacific Ocean (WOR, 2014). (B) Polymettlic nodule (Green-car-congress, 2021).

while subsea mining involves drilling into the ocean floor and extracting minerals from rock formations. Both methods require specialized equipment and technology, including remotely operated vehicles (ROVs), autonomous underwater vehicles (AUVs), and deep-sea drilling equipment.

Technological constraints have limited the success of mining trials in extracting nodules from the seafloor, but these attempts have been instrumental in advancing the development of the next generation of deep-sea mining nodule collectors. Notably, in 1978, two pilot mining tests were carried out by Mining Inc. (OMI) and Ocean Mining Associates (OMA) in the North Equatorial Pacific, employing the first hydraulic collector system described in the literature (Ozturgut et al., 1981). This system utilizes a water jet with low pressure and scouring action to lift nodules from the seafloor. Over the years, mining technology has matured, leading to the development of various versions of polymetallic nodule mining tools. Among these, the hydraulic Polymetallic Nodule Mining Tool (PNMT) stands out as the most commonly utilized method (Elerian et al., 2021). A polymetallic nodules mining system comprises three main components: the Polymetallic Nodule Mining Tool (PNMT), the Vertical Transport System (VTS), and the Production Support Vessel (PSV) (see Figure 1.3). The PNMT is responsible for collecting nodules from the sea floor, primarily separating them from excess water and fine sediments, which are discharged back into the surrounding environment. Subsequently, the VTS transfers the nodules to the PSV, where they undergo further separation from Sediments, Waste, and Other Effluents (SWOEs). Lastly, the VTS returns the water-SWOEs mixture back to the deep sea. This mining concept is based on the work of Bath and Greger, 1988 and Oebius et al., 2001. Deep sea mining equipment is nowadays still in the development and testing stages (Helmons et al., 2022).

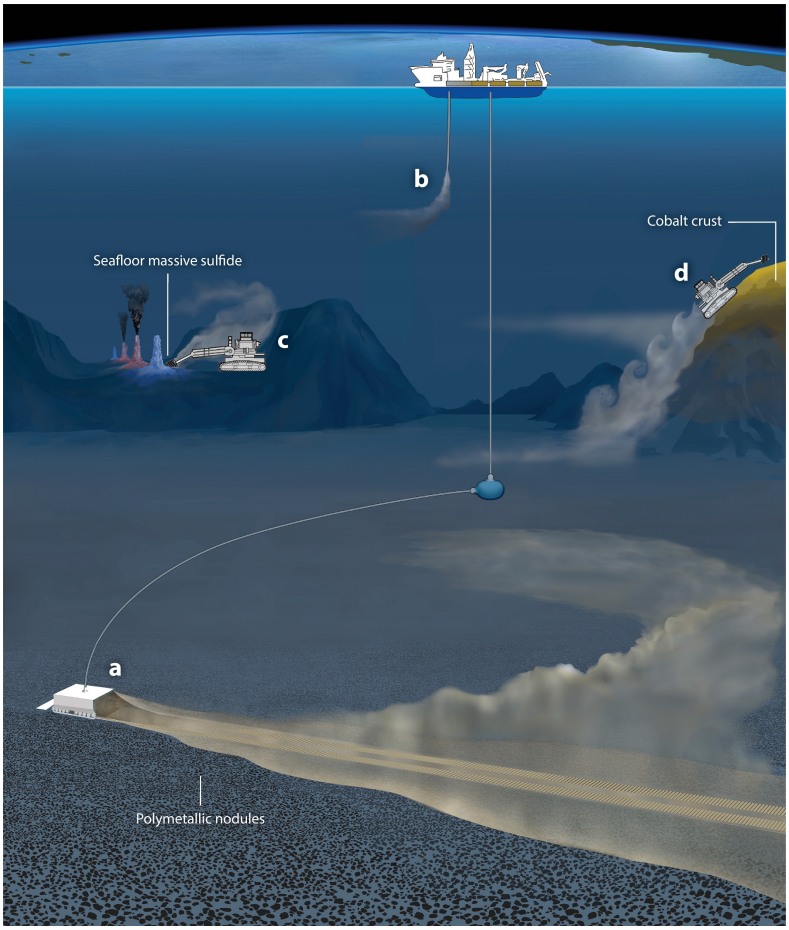


Figure 1.3: This illustration depicts three distinct types of proposed deep-sea mining activities, along with their associated sediment plumes (please note that the plumes and vehicles are not drawn to scale, and the mining operations are located in distant geographic areas). (a) A polymetallic nodule mining operation is shown using a single collector vehicle, and (b) a potential associated return water discharge. (c) A massive seafloor sulfide mining operation is depicted around a hydrothermal vent site. (d) Lastly, a cobalt crust mining operation is illustrated on the flank of a seamount. (Peacock and Ouillon, 2023).

1.1.4. SEDIMENT PLUMES AND TURBIDITY CURRENTS

Sediment plumes are a common environmental consequence of human activities such as dredging, mining, and construction in aquatic environments (Decrop et al., 2013; Sharma et al., 2001). These plumes consist of suspended particles, including sediment, organic matter, and potentially pollutants, released into the water column during disturbances of the seafloor or water column. They can travel long distances from their source and have ecological and economic impacts, including smothering habitats, altering water quality, and reducing light penetration, which can harm marine life (Gollner et al., 2017; Jones et al., 2017; Ramirez-Llodra et al., 2011; Van Reusel et al., 2016), though these hypothesised

potential outcomes require confirmation by measurements from test mining.

DSM also has the potential to significantly alter the deep sea environment by disturbing seafloor habitats (burying benthic organisms), releasing toxic metals from sediment pore water and contaminating food supplies for marine life (Gollner et al., 2017; Jones et al., 2021; Smith et al., 2020; Weaver et al., 2022). Seafloor mining, in particular, can destroy or alter habitats that support unique and sensitive ecosystems (Oebius et al., 2001) by releasing sediment plumes (see Figure 1.3). Small individual grains and low density particles (such as organic matter flocculated sediment) have low settling velocities, which implies that ocean currents can transport them over considerable distances. The potential impacts of DSM are complex and difficult to predict, and there is still much to be learned about the ecological consequences of this emerging industry.

There are four primary origins of sediment plumes associated with PNMT, with three of them being in close proximity to the seabed. The first source arises from the discharge of the sediment-water mixture remaining after the separation process in a PNMT (Decrop and Wachter, 2019). The second source occurs after the completion of the dewatering and ore handling process on the PSV, where the Sediment-Water Ore Mixture (SWOE) is discharged from the VTS (Rzeznik et al., 2019). The third source is the sediment disturbance caused by the movement of the PNMT tracks. Lastly, the fourth source of sediment plumes results from spillage during the hydraulic collection process.

There are three distinct phases in the evolution of sediment plumes associated with deep-sea mining (Elerian et al., 2021; Elerian et al., 2022; Peacock and Ouillon, 2023). The discharge phase is distinguished by the dominance of inertial and turbulent processes in the immediate vicinity of the mining equipment. The second phase is buoyancy-driven, in which the suspended sediment's negative buoyancy and any persistent induced turbulence interact with the surrounding ocean environment. The third and final phase is passive transport, which is characterized by the passive advection of a dilute plume by background currents, horizontal and vertical diffusion by ambient turbulence, and sediment settling and deposition. The spatial and temporal scales linked to each of these three phases increase progressively from the discharge to the passive-transport phase. However, the specific points at which these transitions occur and the existence of all three phases are heavily influenced by the design and operation of the mining equipment and the surrounding environmental factors.

At present, the exact size of the affected area and the severity of the resulting environmental impact remain unknown. To address this, two key technical objectives are of utmost importance: firstly, accurately predicting the trajectory of these plumes and the resulting deposition layers, and secondly, minimizing the area impacted by these near-bed plumes.

Turbidity currents studied in this thesis are generated by negative buoyancy and are expected to be representative of the ones generated by the mining vehicle during mining activities. Turbidity currents generated by a lock-exchange experiment will be used in this thesis to study the properties of sediment flows. They will be created such as to mimic, the near-bed plumes created by the mining vehicles.

The combination of water, sediment, and fine-grained nodule debris released behind the

mining vehicle can be described as a negatively buoyant jet or plume. Owing to its greater density, the plume will rapidly sink to the seabed and then continue to move as a turbidity current. PNMT-generated turbidity flows exhibit two distinct regions: the near-field and far-field regions. The near-field region, situated close to the PNMT, is characterized by relatively small lengths and time scales, usually measured in meters and minutes. This area is of particular engineering interest as it is where potential solutions can have a direct impact.

On the other hand, the far-field region extends beyond the near-field and encompasses much larger spatial and temporal scales, typically in the order of kilometres and days. The precise transition between these two regions remains poorly understood. Nonetheless, the classification of turbidity flows into these two categories provides valuable insights into their nature in each region, thereby influencing the development process of the PNMT. Although there is still much to uncover regarding the link between these regions, this classification framework serves as a solid foundation for studying and comprehending the flow dynamics associated with the PNMT.

During the exploitation phase of nodule mining, a typical seafloor mining tool is designed with a width of 10–20 m and moves forward at a speed of approximately 0.3–0.5 m per second (Global Sea Mineral Resources NV, 2018). Various estimates of seabed disturbance or erosion depth exist, with some sources indicating around 7 cm (Lang et al., 2019), while others propose a range of 5–15 cm (Global Sea Mineral Resources NV, 2018) or 10–15 cm (Nauru Ocean Resources Inc, 2021). Information on the amount of excess water discharged by the collector system is limited in the public domain, but some studies suggest a range of 125 to 375 litres per second per meter width of the collector (Lang et al., 2019). Considering the estimated erosion depth and discharge flow rate, a volumetric sediment concentration of approximately 1–3% is anticipated, equivalent to 25–80 $g\,L^{-1}$ (Jones et al., 2021).

Sharma et al., 2001 conducted experimental investigations to examine the impact of sediment disturbance caused by DSM applications, specifically focusing on benthic life in the disturbed area. Decrop et al., 2013 and De Wit et al., 2014 studied the changes in velocity and concentration profiles of sediment plumes resulting from dredging operations. Numerous numerical studies have been conducted alongside experimental investigations on DSM. Grunsven et al., 2018 presented comprehensive numerical and experimental findings related to plume discharge from a VTS. Decrop and Wachter, 2019 performed a Computational Fluid Dynamics (CFD) analysis to investigate the effects of different discharge conditions for a horizontal discharge from a PNMT. Ouillon et al., 2021 recently employed DNS simulations to study the discharge process of a moving PNMT using the Boussinesq approach. Elerian, 2023 introduced a novel numerical model for predicting turbidity flow behind a PNMT. Their model combines the drift-flux modelling approach with the population balance model. All these numerical models require a comprehensive amount of input data for calibration and ultimately prediction of turbidity flows.

1.1.5. DEEP SEA SEDIMENT

Deep-sea environments cover 65% of the Earth's surface and host 95% of the global biosphere (Herring, 2001; Thistle, 2003; Tyler, 2003). Surprisingly, it remains the most

enigmatic biome, as only 0.001% of it has been sampled and described concerning biodiversity (Danovaro et al., 2014). Deep sea sediment encompasses diverse materials, including mineral particles, organic matter, and microorganisms, that are amassed on the ocean floor in deep-sea regions. These sediments play a pivotal role in shaping the Earth's geological and environmental processes. The composition of these deep-sea sediments varies depending on their location and the contributing factors to their formation. They commonly consist of clay, silt, sand, small rock fragments, and organic matter derived from the remnants of marine organisms (BGR Environmental Impact Assessment, 2019; Bischoff et al., 1979; Global Sea Mineral Resources NV, 2018; Lang et al., 2019; Zawadzki et al., 2020). The local clay composition in each location of the deep sea can show significant variations, but smectite and illite remain the most prevalent components across all publicly reported cases(Bischoff et al., 1979; Global Sea Mineral Resources NV, 2018; Zawadzki et al., 2020).

The origins of deep-sea sediment can be traced to various sources. Terrigenous sediment comprises particles eroded from the continents, carried by rivers, wind, and ice, and ultimately deposited in the ocean basins. Biogenous sediment, on the other hand, arises from the remains of marine organisms, such as shells, skeletons, and calcareous or siliceous structures. For instance, the shells of tiny planktonic creatures like foraminifera and coccolithophores contribute to this type of sediment. Additionally, volcanic ash resulting from volcanic eruptions may be ejected into the atmosphere and eventually settle in the ocean, becoming part of the sediment. Authigenic sediment is formed in situ on the ocean floor through chemical reactions, often involving the precipitation of minerals from seawater.

Accumulation rates of deep-sea sediment can significantly differ depending on the region. Some areas experience relatively rapid sediment accumulation, while others witness a much slower rate of deposition. This variation plays a crucial role in shaping the deep-sea environment's geological features and ecological dynamics. The deep-sea sediment accumulation rates are typically less than 30 meters per million years, with some cases as low as 0.1 meters per million years (Lyle, 2015).

Due to the substantial depth of large portions of the abyssal seafloor, which lies well below the carbonate compensation depth (CCD), the biogenic carbonate settling from the euphotic zone tends to be mostly unrecoverable. Consequently, deep-sea clay is typically deficient in carbonate content and mainly consists of a blend of clay minerals and siliceous remnants of plankton, such as diatoms and radiolarians. The preservation of carbonate in the sediment only occurs below biologically productive surface waters, such as equatorial upwelling zones, where the biogenic carbonate supply exceeds the dissolution rate below the CCD. The supply of fresh organic matter to the seabed, a factor that potentially influences the aggregation of suspended sediment, exhibits significant variation depending on the overall productivity regime of the surface water and the water depth (Fettweis and Baeye, 2015). Generally, as water depth increases, the organic matter flux to the seabed decreases due to the progressive degradation and remineralization of organic matter as it sinks to greater depths. Seamounts located at shallower depths beneath biologically productive surface waters experience a substantially higher influx of fresh organic matter compared to abyssal plains. This disparity is reflected in the

abundance and biomass of benthic life, which relies on the vertical flux of organic matter. In the CCFZ, the upper few centimetres of sediment contain less than 0.5% carbon content relative to the sediment mass. Below 30 cm depth, this carbon content decreases further to 0.1% of the sediment mass (Volz et al., 2018).

In the CCFZ, the oxygen penetration depth in the sediment ranges from 1 to 4.5 meters (Kuhn, 2015). This suggests that the surface sediment experiences high POC degradation due to aerobic conditions. In contrast, anoxic sediments, such as those in continental margins, exhibit 10 to 100 times lower degradation than oxic conditions (Aller, 1994). Surprisingly, even under oxic, cold (1.5 °C), and high-pressure conditions, the sediment microbial community is known to undergo significant changes and fluctuations within just one week when exposed to phytodetritus (Kanzog et al., 2009). In these environments, benthic remineralization of POC is primarily driven by microbes, while metazoans and macrofauna play a minor role (Sweetman et al., 2019).

The physical and biological carbon pumps (see Figure 1.4(A)) are two mechanisms that play essential roles in the global carbon cycle. The ocean serves as the second-largest carbon reservoir on Earth (Finkel, 2014; Le Quere et al., 2018; Passow and Carlson, 2012). In the context of the carbon cycle, the physical carbon pump refers to the process by which carbon dioxide (CO2) from the atmosphere is absorbed and transported into the deeper layers of the ocean. This constitutes the most substantial carbon pool in the ocean (Falkowski et al., 2000), known as dissolved organic carbon (DOC). This occurs through various physical processes like ocean circulation, upwelling, and mixing. Once carbon is transferred to the deep ocean, it can remain stored there for long periods, sequestering carbon and reducing its concentration in the atmosphere, thus helping to mitigate the impacts of climate change.

Only, around 3% of this annual carbon pool (Ducklow et al., 2001), undergoes a further transformation into biomass and is transferred from the ocean surface to the deep sea. This process is termed the biological carbon pump. The biological carbon pump involves the uptake of CO2 by marine organisms, such as phytoplankton, during photosynthesis. These tiny organisms use carbon dioxide to produce organic matter, which serves as food for other marine organisms. When phytoplankton and other marine life die, their organic matter sinks to the ocean floor in the form of marine snow (see Figure 1.4(B)), where it can be buried and eventually form sedimentary rocks, further locking away carbon from the atmosphere.

The biological carbon pump is a vital pathway in the ocean carbon cycle, where dissolved inorganic carbon (DIC) is transformed into particulate organic carbon (POC) and DOC through the photosynthesis of phytoplankton (Turner, 2015). This newly generated biomass becomes part of the upper ocean's marine food web and undergoes a series of interconnected processes, including cell death, grazing by zooplankton, and microbial respiration. These processes play a crucial role in cycling carbon within the marine ecosystem. Ultimately, the reconverted mixture of biomass and residual cells will give rise to dissolved organic matter (DOM) and particulate organic matter (POM), including aggregates like marine snow and faecal pellets. These particles sink out of the euphotic zone (sunlight zone), descend to the deep ocean, and effectively export carbon from

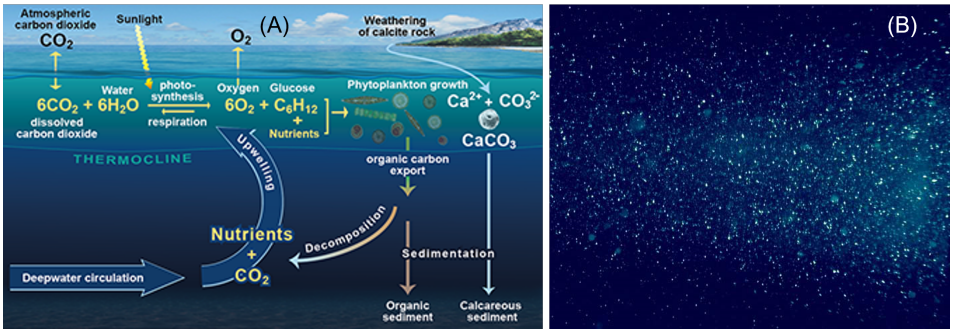


Figure 1.4: (A) The ocean carbon cycle (Image credit: NOC/V.Byfield). (B) Marine snow consists of detritus particles that descend gradually through the water, resembling the gentle descent of snowflakes through the air (Image credit: Atlantic BiogeoChemical Fluxes).

the ocean's surface layers (Lutz et al., 2002). Within the upper ocean, the attenuation of carbon flux appears to be primarily influenced by zooplankton grazing (Iversen and Ploug, 2010). On the other hand, in the deep ocean, microbial degradation takes dominance in carbon flux attenuation (Iversen and Ploug, 2010; Stemmann et al., 2004).

1.2. FLOCCULATION IN PLUMES AND TURBIDITY CURRENTS

The ocean bed sediment is composed of a mixture of mineral sediment and organic matter. The interaction between mineral and organic particles leads to the formation of a cohesive sediment, commonly known as "mud." In the water column, the mineral and organic particles can undergo aggregation and break-up processes, leading to the formation of entities called "flocs" (aggregates). The aggregation (flocculation) rate is a function of the particle collision efficiency. The particle's efficiency to collide is influenced by particle size, concentration, settling velocity, and shear, while the particle's sticking probability is related to the particle composition (in particular surface properties, like surface charge) (Chassagne, 2020; Deng et al., 2019; Kiørboe, 2001; Safar et al., 2019). On the other hand, break-up, leading to a decrease in floc size, is predominantly a function of shear (Chassagne, 2020; Deng, 2022; Manning and Dyer, 1999; McCave, 1984; Safar, 2022). Other mechanisms, like structural changes in the floc, can lead to a decrease in floc size without loss of mass (Shakeel et al., 2020). These mechanisms collectively contribute to the dynamic particle interactions and transformations occurring within the marine environment.

The mechanisms of flocculation are specific to each type of sediment, making it challenging to predict particle behaviour accurately. Smith and Friedrichs, 2011 work investigated flocculation's impact on dredging plumes. The findings indicated a gradual increase in both settling velocity and floc sizes over time. Additionally, it was observed that higher concentrations of suspended sediments were conducive to the formation of flocs. Some early studies (Gillard, 2019; Spearman et al., 2020; Spearman et al., 2019) on DSM operations have also suggested that the aggregation of sediment particles can enhance the settling potential of suspended sediment resulting from mining activities. This could lead

to reduced turbidity levels in both near-field and far-field regions, potentially minimizing environmental impact.

The sediment plume evolves quite rapidly behind the mining vehicle (Figure 1.5). Particle size develops through the flocculation process. The key parameters to affect the flocculation of clay are organic matter, salinity and hydrodynamic conditions (Deng, 2022; Ho et al., 2022; Safar et al., 2023; Skinnebach et al., 2019). In the case of deep sea clay there is some evidence that the same parameters play a role for flocculation (Gillard, 2019; Gillard and Thomsen, 2019; Helmons et al., 2022; Munoz-Royo et al., 2022; Spearman et al., 2020; Spearman et al., 2019). In the work of Gillard (Gillard et al., 2019) one can for instance infer from the microscope pictures that the observed floc contains some organic material. We expect that the deep sea temperature does not play a significant role in the flocculation of deep-sea clay as it will not change during the mining process (the effect of temperature will be studied in Chapter 5 and it will be shown that the laboratory results are not temperature-dependent). As hydrostatic pressure is isotropic at the scale of the volume where flocculation takes place, polyelectrolytes are by nature not affected by hydrostatic pressure and mineral particles are incompressible, it can safely be assumed that flocculation do not depend on hydrostatic pressure. Experiments performed in the laboratory are in that respect to be compared with in situ observations.

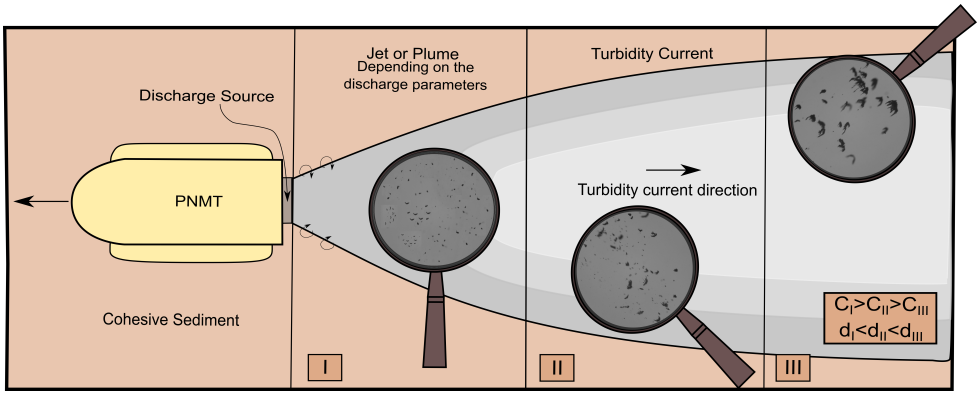


Figure 1.5: Categorization of near-field turbidity flow and particle size evolution through flocculation in the near-field region. Concentration and particle size are denoted by C and d, respectively (figure adapted from Elerian, 2023).

1.3. RESEARCH QUESTIONS AND THESIS OUTLINE

Gaining a comprehensive understanding of the role of flocculation in the dispersion of sediment plumes and turbidity currents could help to understand better the impact of deep-sea mining on the local ecosystem. In particular, the main hypothesis tested within this thesis is whether (or not) flocculation due to the presence of organic matter impacts sediment plume propagation and local turbidity levels.

Field studies involving full-scale discharge processes are intricate and challenging, as they require advanced measurement techniques to quantify the physical processes during

mining operations precisely. Despite recent efforts (DEME-Group, 2021; Haalboom et al., 2023; Haalboom et al., 2022; Munoz-Royo et al., 2022) to conduct field experiments, it is still impractical to test all discharge scenarios in the field because of the significant costs and difficulties involved and the numerous variables at play. It is also unfeasible at this stage to properly monitor flocculation in situ.

Laboratory studies are, therefore, essential for understanding how particle size and flocculation affect the dispersion of turbidity flows. In particular, laboratory experiments enable one to study the influence of relevant parameters (like shear and concentration) on flocculation individually. At present, there is limited literature on the impact of concentration and shear on floc growth and none about the specific case of deep-sea sediment.

The PhD thesis is structured as follows. First, chapter 2 presents a comprehensive overview of the methods employed. In addition to the generic research question mentioned above, this thesis is organised around the following key research questions that serve as the foundation for individual chapters.

1. **Can flocculation reduce the spread of turbidity currents?** This research question is addressed in Chapter 3.
2. **What is the effect of concentration on the evaluation of a particle's settling velocity in turbidity currents?** In Chapter 4, the settling behaviour is investigated as a function of the number of flocs transferred to the settling column.
3. **What is the effect of different in-situ conditions on the flocculation of deep-sea clay collected from Clarion Clipperton zone?** In Chapter 5, the flocculation of deep-sea clay is studied. This chapter pinpoints the role of several key parameters, including temperature, concentration, shear and resting time, on the flocculation process.
4. **How to parameterize a flocculation model to be used in sediment transport modelling?** In Chapter 6, a comparison is made between a recently published flocculation model, which is based on logistic growth theory, and a model based on the population balance equation.

The final chapter provides a general summary and outlook.

2

METHODS

This chapter presents the experimental methods (including jar, rotational wheel, and lock exchange) used for the analysis (such as Malvern for particle size distribution, FLOCCAM for floc size and settling analysis, SAFAS for video analysis) presented in the thesis. All details of the methods and techniques used in the following chapters are explained here.

2.1. INTRODUCTION

The process of fine (colloidal)particles coming together to form aggregates is called flocculation. These aggregates, or "flocs", are usually rather polydisperse in natural environments, both in saline and in freshwater systems (Alldredge and Silver, 1988; Gregory and O'Melia, 1989; Manning and Dyer, 1999; Ransom et al., 1998). Flocculation is driven by hydrodynamics and the settling of particles, and flocs are composed of a mixture of organic matter (like plankton and exopolymers) and mineral clay.

2.1.1. FLOC CREATION

The mechanisms that lead to floc creation in situ are challenging to duplicate in a laboratory setting, as samples need to be constrained in small volumes. This implies in particular that numerous experiments should be set up to replicate the conditions found in situ, in terms of various particle concentrations and shear stresses for example. This will be done in the present thesis.

Previous studies have demonstrated that flocs created in jars and that are subsequently pumped to a particle sizer (as the one described below) are prone to reconform or erode under shear (Chassagne, 2020; Jarvis et al., 2005; Kim et al., 2001). These experiments have nonetheless the advantage that flocculation tests in jars are standardized, and this enables a better comparison between studies. In order to get a flocculation process that is more representative of in situ conditions, three new experimental protocols were used. First, flocs created in the jars were not pumped through the particle sizer but rather studied using the FLOCCAM device (described below). Secondly, flocs were created using a rotating wheel (described below) and then studied using the FLOCCAM. Thirdly, flocs were created in a mixing tank (described below), and then released in a lock exchange, whereupon samples were taken at different positions in the lock and analyzed for size.

2.1.2. FLOC SIZES

Various methods (laser or image-based) are available to characterize the size and structure of flocs (Abbireddy and Clayton, 2009; Li et al., 2005; Liang et al., 2015; Manning et al., 2007). The irregularity in floc shape poses challenges in measurement and quantification. Specific equivalent diameters are therefore commonly utilized to define floc size and facilitate comparisons across various floc systems (Xu and Guida, 2003). Laser diffraction techniques have the advantage of being able to record a full particle size distribution (from a few nm to a few mm) in 10 seconds. This makes laser diffraction (static light scattering, (SLS)) a useful tool for studying flocculation dynamics (Govoreanu et al., 2009; Zhou and Franks, 2006). SLS has also the advantage over video microscopy to be able to measure particles of sub-micrometre sizes. However, SLS performs poorly when particles are anisotropic in shape and have low or inhomogeneous refractive index.

Microscopy, while informative about floc shape and structure, is time-consuming and demands extensive sample preparation. However, settling analysis with video can be applied to most floc systems, also for samples with low concentrations (Manning and Dyer, 2007; Ye et al., 2020). Experimental set-ups and associated software are not yet available on the market, owing to, in particular, the difficulty in image analysis, due to the contrast to be found between flocs and background. In this thesis, we worked

with a homemade set-up and an open-source software package developed in our group (described below). From this set-up, besides particle size, it is also possible to record particle settling velocity, from which, assuming that the particles settle according to Stokes settling velocity, their effective density can be estimated.

2.2. SET-UPS FOR FLOC CREATION

2.2.1. LOCK EXCHANGE SETUP

Turbidity currents have been extensively studied in the laboratory using lock-exchange experiments (Baker et al., 2017; Craig et al., 2019; Nogueira et al., 2013). Lock exchange experiments or fixed-volume turbidity currents, are caused by the release of dense material in a fixed volume. Frontal propagation in a traditional lock-release turbidity current is equivalent to frontal propagation of the front moving orthogonal to the direction of motion of the source. (Ouillon et al., 2021).

Lock exchange experiments were performed in a 3 m long and 0.40m high (see figure Figure 2.1), set up by mixing dry clay in water in the lock exchange's mixing section for an hour before opening the lock gate. This mixing ensured that homogeneous suspensions with a well-defined mean particle size could be obtained. The initial clay size obtained by such a process might not be similar to that obtained through the DSM operation, in which the sediment passes through the SMT for a brief period of time exposed to high shear rates. The turbidity flow was filmed with a Navitar 17 mm lens on an IL5HM8512D: Fastec high-speed camera. The camera was set 4.75 m from the lens to the front wall of the tank, and it recorded at a rate of 130 frames per second. The camera captured the 2.40 m to the left of the lock. Samples were collected from four locations (L1, L2, L3, L4 in Figure 2.1) at the end of the experiments from the collection points located at the bottom of the lock exchange.

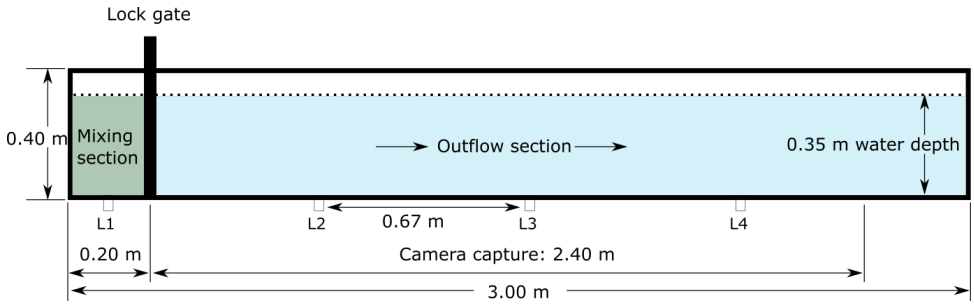


Figure 2.1: Schematic representation of the Lock exchange setup. The samples are taken at L1, L2, L3 and L4 locations.

2.2.2. JAR EXPERIMENTS

Flocculation experiments were carried out using a JLT6 jar set-up provided by VELP Scientifica, Italy. The jar had dimensions of 95 mm in diameter and 110 mm in height. A single rectangular paddle with dimensions of 25 mm in height and 75 mm in diameter

was used to stir the suspension. The paddle was positioned 10 mm above the bottom of the jar within the suspension (Figure 2.2).

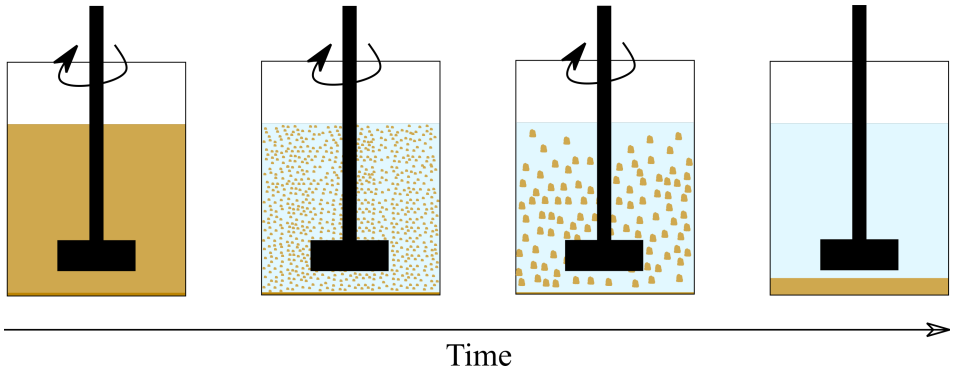


Figure 2.2: Schematic representation of the flocculation experiment steps in a jar.

2.2.3. ROTATING WHEEL

A rotating wheel (Figure 2.3) is used to induce differential settling flocculation alongside low-shear conditions. The wheel has an internal diameter of 34 cm and a depth of 7 cm. Below the permanent thermocline in the interior of the ocean, where currents are significantly weakened, the dominant process driving particle aggregation is differential settling. This aggregation process significantly impacts the dispersion of sediment plumes as particles with different settling velocities come together to form aggregates.

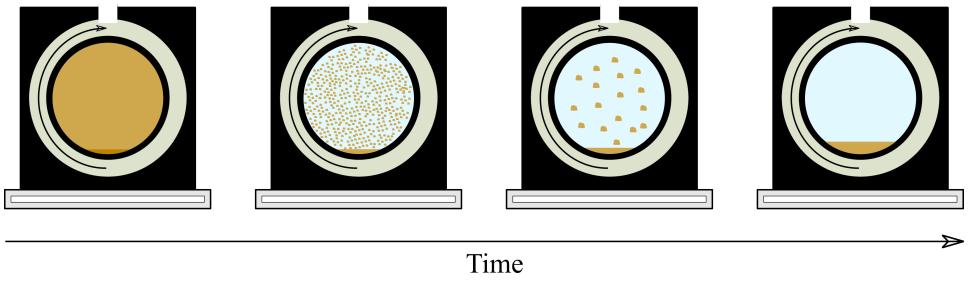


Figure 2.3: Schematic representation of the flocculation experiment steps in a wheel.

2.3. FLOC SIZE AND SETTLING MEASUREMENTS

2.3.1. MALVERN: PARTICLE SIZE DISTRIBUTION

Malvern Mastersizer is a brand of instruments used for particle size analysis. It uses laser diffraction technology to measure the size distribution of particles in a sample, ranging from nanometers to millimetres. The instrument sends a laser beam through a sample and measures the scattered light's angle and intensity to calculate the particle size distribution. It is important to take into account several constraints of this tool, including

(i) the use of Mie theory to convert raw data to PSD assumes that all particles are spherical; (ii) measurements are limited to a certain concentration range due to laser obscuration; and (iii) inaccurate (D_{50}) values may be obtained for samples containing significant sand fractions due to data smoothing by the software (Sanz, 2018).

Particle Size Distribution (PSD) analysis was conducted on the obtained samples using a Malvern Master Sizer 2000 (Figure 2.4), a technique based on static light scattering (SLS). This setup can record a full PSD within a few seconds. The suspension was pumped through the Malvern Master Sizer 2000 from the mixing jar to the Mastersizer and then back to the mixing jar using a peristaltic pump (Figure 2.4). In addition to PSD measurements of pure clays, this setting was also used for shear rate experiments. Previous studies have shown that organic matter-rich flocs are not affected by breaking/or reconformation at short timescales (a few minutes) when transported through the piping of the setup (Safar, 2022; Shakeel et al., 2020).

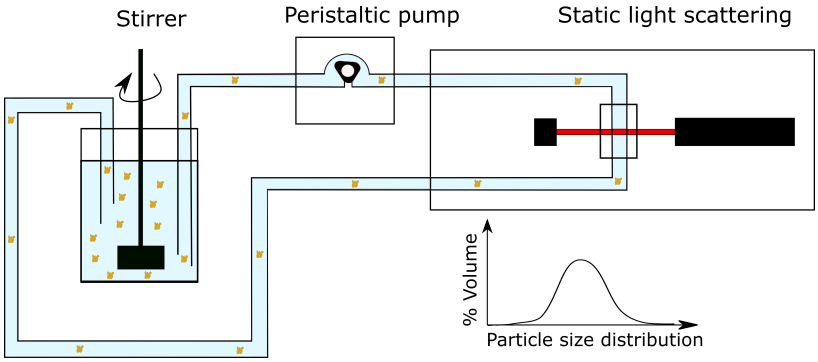


Figure 2.4: Schematic representation of the Malvern master Sizer 2000 for particle size measurement.

2.3.2. FLOCCAM: FLOC SIZE AND SETTLING ANALYSIS

The FLOCCAM device is based on video microscopy and can be used to estimate PSDs (> 20 µm) and settling velocities of flocs samples (Manning et al., 2007; Mietta et al., 2009; Shakeel et al., 2021; Ye et al., 2020). Figure 2.5 shows a schematic representation of the equipment. The PSD, shape, and settling velocity of the flocs are calculated from recorded videos of settling flocs in a settling column using a software package called Safas (MacIver, 2019).

FLOCCAM setup consists of several components. Firstly, a settling column was employed, which was a cylindrical structure with dimensions of 10 cm x 10 cm x 30 cm. It featured glass front and rear panels and plastic sides. A 5MP CMOS camera with a resolution of 2592x2048 pixels and a pixel size of 4.8 um was utilized to capture the video footage. The camera was equipped with a Global Shutter and identified as iDS UI-3180CP-M-GL Rev.2.1 (AB02546). Complementing the camera, an S5VPJ2898 telecentric lens with a tunable working distance and C-mount manufactured by Sill Optics GmbH & Co. KG was utilized. This camera and lens combination produced an approximate pixel size of 8.6 mm. A Flat Lights TH2 Series Red LED light panel with dimensions of 63x60 was used

to provide adequate lighting during the experiments, known for its high directivity. A DC 24V Input Controller for LED Lights, model PB-2430-1 by CCS Inc., was employed to control the light source. The data recording and analysis were facilitated using a Dell Inspiron-15-7590 laptop. Additionally, a feed well prototype, which was a conical piece of plastic, was utilized to direct the flow of flocs. It terminated in a 2 mm x 10 mm rectangular opening. A pipette is employed for the careful extraction of flocs to be sampled, followed by the measurement and recording of settling velocities approximately 30 cm below the injection point.

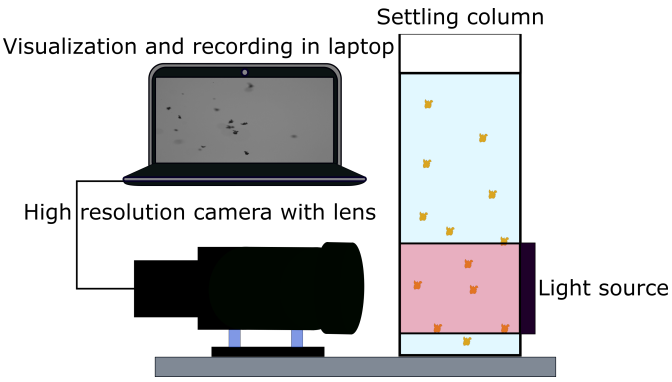


Figure 2.5: Schematic representation of the FLOCCAM setup.

2.3.3. SAFAS

Safas (MacIver, 2019), which stands for Sedimentation and Floc Analysis Software, is a Python module tailored to process and interpret images and videos of flocs, commonly known as aggregates or cohesive sediments. This package empowers users to directly analyze such images and videos, facilitating the measurement and storage of vital data such as size, morphology, and settling rate in a user-friendly format.

Furthermore, Safas is an open-source Python software that allows users to access and extend its image filters. These filters have been meticulously designed and rigorously tested to serve the specific purpose of segmenting and quantifying images of flocs. They harness a range of functions to achieve precise and reliable results.

The parameters presented below were derived from the videos of the flocs:

MEAN DIAMETER

Following the convention used by multiple authors (Manning et al., 2007; Ye et al., 2020), the mean diameter (d_m) in micrometres (µm) was determined by calculating the average of the major axis diameter (d_{major}) and the minor axis diameter (d_{minor}) of the object present in an image.

$$d_m = \sqrt{(d_{major} \times d_{minor})} \tag{2.1}$$

A discussion about mean floc size (in the case of organic matter rich flocs), floc structure, anisotropy and uncertainty regarding 2D measurement of flocs can be found in (Safar,

2022; Spencer et al., 2022).

ASPECT RATIO

To estimate the aspect ratio (AR) of the flocs, their major axis diameter (d_{major}) and minor axis diameter (d_{minor}) were utilized in the following manner:

$$AR = \frac{d_{major}}{d_{minor}} \tag{2.2}$$

EFFECTIVE FLOC DENSITY

The effective floc density (ρ_f) is given as follows (assuming that Stokes is valid):

$$\rho_f = \rho_w + \frac{9\eta v}{2gR_f^2} \tag{2.3}$$

where ρ_w represents the density of the water, η represents the dynamic viscosity of water, v represents the floc settling velocity, g stands for the acceleration due to gravity, and R_f denotes the radius of the floc. To estimate the mean density of the flocs, the approach involves averaging the density values obtained for each size.

FRACTAL DIMENSION

In the context of flocs being considered fractal entities and composed of primary particles of size a, the volume fraction of solids (ϕ_s) within a floc is expressed as follows:

$$\phi_s = \frac{N.a^3}{R_f^3} = \left(\frac{R_f}{a}\right)^{D-3} \tag{2.4}$$

where N represents the number of solid particles in a floc, and D is the fractal dimension of flocs. The density of flocs is correlated to the volume fraction through the following relationship:

$$\frac{(\rho_f - \rho_w)}{\rho_s} = \frac{\phi_s(\rho_s - \rho_w)}{\rho_s} \tag{2.5}$$

By incorporating the solid (clay) density, denoted as ρ_s, the combination of Equation (2.4) and Equation (2.5) results in the following expression:

$$(\rho_f - \rho_w) = (\rho_s - \rho_w)\left(\frac{R_f}{a}\right)^{D-3} \tag{2.6}$$

The fractal dimension D can be determined by fitting the function $\rho_f - \rho_w$ as a function of R_f, as demonstrated by Manning and Dyer, 1999 and Guo et al., 2021. However, these objects are not true fractals when dealing with natural flocs. Hence, it is more suitable to refer to "pseudo-fractal dimension", a term used by Malarkey et al., 2015 and Chassagne, 2020.

3

FLOCCULATION IN TURBIDITY CURRENTS

In this chapter, the significance of flocculation in the dynamics of turbidity currents within marine environments is explored. Understanding this process is crucial to mitigate the impact of activities like dredging, trenching, and deep-sea mining. In the present study laboratory experiments using lock exchange techniques are conducted. Clays akin to those found in abyssal regions where deep-sea mining occurs are used to create turbidity flows. The flow propagation in time and particle sizes along its path are recorded and analysed. The impact of salt and organic material as flocculants are studied, as a function of various clay and organic flocculant concentrations. The flocculant chosen was an ionic polyelectrolyte, quite representative of natural organic polyelectrolytes like polysaccharides. Through video analysis and particle size/settling velocity measurements, it was found that turbidity currents in fresh and saline water, without the addition of flocculant, exhibit similar velocities and the currents reached the end of the lock in all cases. In the presence of organic matter, it was found that the flocs released from the lock flocculated while propagating, hereby changing in sizes and settling velocities, diminishing current propagation. Interestingly, salt ions enhanced flocculation in this case. The findings of the study are quite generic and therefore expected to be of interest for various types of turbidity currents and dredging plumes studies.

Parts of this chapter have been published in Frontiers in Earth Science 10 (2022). ISSN: 2296-6463 Ali et al., 2022b.

3.1. INTRODUCTION

DREDGING is commonly used for land reclamation, creating or deepening ports and waterways, and a lot of studies have been conducted on the impact of dredging on the environment (Newell et al., 1998; Pennekamp and Quaak, 1990; Varriale et al., 1985). Underwater mining is used for mineral extraction from underwater deposits. Over the last decade, the interest in the latter has substantially increased since the demand for minerals and metals has grown as the result of the World's population and economic activity surge. Mining activities produce sediment plumes that lead to an increase in suspended solids concentration, thereby impacting benthic ecosystems, especially in deep-sea environments (Glover and Smith, 2003; Kaikkonen et al., 2018; Morgan et al., 1999; Thiel, 1992, 2003).

There is increasing interest in metals, particularly those critical for a successful renewable energy transition (e.g. wind turbines, solar panels and electric car storage batteries)(Hein et al., 2020). Precious metals such as manganese, nickel, and cobalt are mined from terrestrial mining, however, Deep Sea Mining (DSM) might be an alternative to fill the demand for precious metals. Polymetallic nodules, which contain significant amounts of these precious metals, are found in abundance on the abyssal plains in the deep sea. These nodules are distinguished from terrestrial deposits by the presence of many metals in a single deposit; for example, nodules from the Clarion–Clipperton Zone (CCZ) which is a large area with polymetallic nodules, contain cobalt, nickel, copper, and manganese in a single ore (Gillard, 2019; Harbour et al., 2020; Hein et al., 2020; ISA, 2019).

In nodule mining, the polymetallic nodule mining tool (PNMT) collects nodules from the seafloor and separates them from excess water and fine sediments. The excess water and fine sediment are released behind the mining vehicle on the seafloor. The key areas of interest in the horizontal discharge of a sediment-water mixture from a PNMT, are shown in Figure 1.5.

1. Discharge source: This includes the preliminary conditions, including momentum, suspended sediment content, and z-distance from the sea bed. The PNMT design affects the physical parameters.

2. Jet or Plume regime: Depending on the flow discharge parameters in this area, the flow may take the form of a jet or plume. Later, when the buoyancy force takes over, the flow transforms into a plume.

3. Impingement region: This area is situated on the ocean floor. Due to the direct connection with the seafloor in this location, the negative buoyant plume changes direction. Within this region, sediment deposition and potential sea bed erosion are anticipated to occur.

4. Turbidity current: This current originates outside the area of impingement. The generated turbidity current's behaviour is governed by the interaction between the discharge and the seabed (Global Sea Mineral Resources NV, 2018; Hage et al., 2019; Ouillon et al., 2021; Rutkowska et al., 2014). Its principal characteristics are determined by the hydraulic characteristics (pipe dimension, flow velocity) previous to the impingement region.

	IOM 1	IOM 2	IOM 3	Site A	Site B	Site C	GSR	IOM
Smectite (%)	12.71	17.33	16.49	52	38	40	36.41	16.3
Illite (%)	13.82	12.05	14.52	31	42	50	48.34	13.2
Kaolinite (%)	0.65	0.43	0.54	17	20	10	10.33	1
Chlorite (%)	1.70	1.85	2.35				4.92	1.5
Amorphic (%)	50.47	47.09	44.42					

Table 3.1: Mineral group percentages in deep-sea sediment: Inter Ocean Metal joint organization (IOM) data (Zawadzki et al., 2020), Global Sea Mineral Resources (GSR) data (Global Sea Mineral Resources NV, 2018), Sites A-C (Bischoff et al., 1979). It is worth noting that for IOM 1, 2, and 3, clay mineral percent is given relative to total sediment. Clay mineral percent is only relative to the sum of clay minerals at Sites A, B, C, and GSR.

Fraction	Diameter range (um)	GSR data average (%)	NTNU data BC062 (%)	NTNU data BC064 (%)	IOM data average (%)	Gillard et al. (2019)
Clay	<2	12.0	11.3	14.5	23.24	25.3
Silt	2-63	76.2	85.7	82.5	70.36	52.11
Sand	63-2000	11.8	3	3	6.13	22.5

Table 3.2: Sediment fraction distribution: GSR and NTNU data (Lang et al., 2019), IOM data (Zawadzki et al., 2020). GSR provides averaged data based on the Belgium license area in the CCZ, while NTNU data is data of specific box-cores of the GSR data average. The IOM data is based on data from the CCZ's IOM license area.

In the near-field region, many flow regimes (such as jet, plume, and turbidity current) are anticipated, and they rely on the discharge characteristics. The focus of this work is on turbidity current. It is estimated that the turbidity current generated from the discharge at the back of the mining vehicle can potentially spread over large distances and remain suspended for an extended period of time (Haalboom et al., 2022; Hein et al., 2020; Nodules, 2020). In particular, Gillard found that the effects of the passive plume settled within 4 km (under typical conditions) and within 9 km (under episodic eddy passages) (Gillard, 2019).

The sediment plume generated by mining activity has the potential to severely affect the deep sea flora and fauna. The settling of the sediment plume and subsequent blanketing has the potential to bury benthic species, obstruct the respiratory surfaces of filter feeders, and contaminate the food source for the majority of benthic organisms (Gollner et al., 2017; Jones et al., 2017; Van Reusel et al., 2016), though this still needs to be confirmed by measurements during test mining. Limiting plume dispersion could help to lower the presumed environmental impact caused by human activities (Weaver et al., 2022).

Particle size distribution (PSD) is an important factor that determines how far deep-sea sediment plumes spread (Gillard et al., 2019; Spearman et al., 2020). The coarse nodule debris settles quickly, but the clay-sized mineral particles (tables 3.1 and 3.2) stay in suspension for long periods of time, which could potentially lead to a wider plume dispersion (Sharma, 2015). Since aggregated particles (flocs) settle quicker, flocculation has been shown to potentially limit plume dispersion (Gillard et al., 2019; Manning and Dyer, 2002; Smith and Friedrichs, 2011; Spearman et al., 2020; Spearman et al., 2019). The size, density, shape, settling velocity and strength of flocs vary over time. These properties are influenced by the medium in which the particles are suspended (salinity, organic matter content, sediment concentration, hydrodynamics) (Chassagne, 2020; Manning and Dyer, 2002; Mietta et al., 2009; Smith and Friedrichs, 2011). The deep-sea

environment is, in principle, favourable for flocculation because of its high salinity and concentration of organic matter (Fettweis and Baeye, 2015; ISA, 2015; Konstantin et al., 2014; Volz et al., 2018). The availability of fresh organic matter on the top layer of the deep sea varies substantially because organic matter gradually degrades and remineralizes with depth. Less than 0.5 percent of the sediment bulk is made up of carbon in the top few centimetres of the CCZ sediment. This decreases to 0.1 percent of the sediment's mass below 30 cm (Volz et al., 2018). Despite the low organic matter content (in mass and volume) as polymeric organic matter has an extremely large surface area only a few milligrams per gram of clay is required to induce flocculation (Deng, 2022; Safar, 2022; Shakeel et al., 2021).

The present work aims to demonstrate the mechanisms that, in the presence of organic matter, can help reduce the extension of the turbidity currents. Flocculation has been shown to occur at very short timescales (in the order of a few minutes) in natural environments in the presence of (microscopic) organic matter (Deng et al., 2019; Safar et al., 2019; Shakeel et al., 2020). The current lab-scale work uses a series of lock exchange experiments to generate a turbidity current and studies the impact of flocculation in short time scales. Properties such as the time and distance of turbidity currents' propagation, particle size, and settling velocities are measured. This chapter is organized as follows: section 3.2 gives an overview of the materials used, section 3.3 presents relevant results and discussion. Finally, the conclusions are presented in section 3.4.

3.2. MATERIAL AND EXPERIMENTAL METHODS

3.2.1. CLAY

Two types of clays were used for the experiments. Initial experiments were conducted by using illite since illite is one of the dominant clay minerals (table 3.2) found of the top layer of the Clarion–Clipperton Zone (CCZ) sediment where Deep Sea Mining (DSM) is performed (Helmons et al., 2022; ISA, 2015). The illite used in the experiments (purchased from Argiletz Laboratoires) was obtained as a dry powder. The d_{50} of illite particles was found to be around 5 µm (Figure 3.1) by static light scattering (Figure 2.4).
A lab-made artificial clay with a composition similar to CCZ clay was also used and will be referred to as Artificial CCZ (ACCZ) (Ali et al., 2022a; Enthoven, 2021). We use this material as a substitute for deep-sea sediment, as CCZ clay could not be supplied in sufficient quantities for lock-exchange experiments. The ACCZ mixture consists of two materials: i) Sibelco FT-S1 (Abidichte Ton) consisting of 64% kaolinite, 10% illite, 19% quartz, and 7% other minerals; ii) Cebo OMCA Betonite consisting of 17% kaolinite, 17% illite and 66% montmorillonite. The precise proportions of these two materials are unknown. The clay was created so that its rheological/mechanical properties match the ones of CCZ clay (Enthoven, 2021). The wet ACCZ clay was dried for 24 hours at 105 °C to determine its dry density, which was found to be 2600 kg m^{-3}. This clay has an average particle size of 10-20 µm, as found by static light scattering device (Figure 3.1).

3.2.2. FLOCCULANT

As discussed on pages 11-12, the organic matter found in the deep-sea region is expected to act as a flocculating agent for the sediment plume. It was not possible, at this stage, to

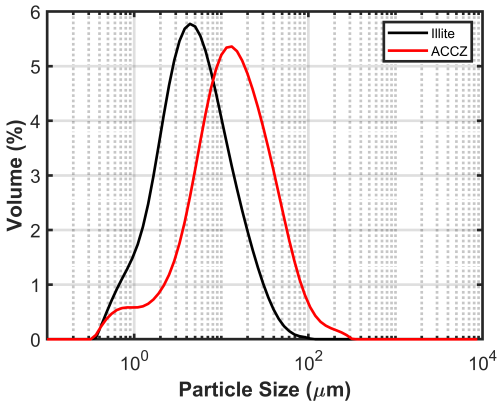


Figure 3.1: Particle size distribution of illite and ACCZ.

obtain or fully characterize this flocculant, which is expected to be composed in parts of polysaccharides. As was done in previous studies (Shakeel et al., 2020), a synthetic flocculant was used as a proxy for organic matter content. The flocculant chosen was an anionic polyacrylamide, referenced Zetag 4120 (BASF company), of medium anionic charge with high molecular weight. Polyelectrolytes with a high molecular weight will better promote flocculation compared to polyelectrolytes with a low molecular weight (Bergaya and Gerhard, 2013).

3.2.3. WATER

Lock exchange experiments (Figure 2.1) were performed in both fresh and saline water. The saline water was produced by mixing $CaCl_2$ to freshwater producing water of ionic strength 10 mM (salinity $1.1 g/kg$). The experiments were conducted for three distinct clay concentrations ($10\,gL^{-1}$, $30\,gL^{-1}$ and $100\,gL^{-1}$) with illite and two different concentrations with ACCZ ($10\,gL^{-1}$ and $30\,gL^{-1}$). Handling and mixing the higher concentration of ACCZ and eventually getting a fully dispersed sample was difficult therefore $100\,gL^{-1}$ was not used. $30\,gL^{-1}$ is the mean case, and $10\,gL^{-1}$ and $100\,gL^{-1}$ are considered to assess whether the design should aim for lower or higher concentrations to identify if and when flocculation has a more significant effect (Nodules, 2020). Two different flocculant dosages ($0.25\,mgg^{-1}$ and $0.75\,mgg^{-1}$ of clay) were used for flocculation based on preliminary studies and are significantly below the optimum flocculant dosage ($2.5\,mgg^{-1}$ as found by Shakeel et al., 2020. Optimum dosage is defined as the dosage at which flocculation rate is highest). The dry clay was mixed in water in the lock exchange's mixing section for an hour before the lock gate was opened. This mixing ensured that homogeneous suspensions with a well-defined mean particle size could be obtained (verified with PSD measurement). The initial clay size obtained by such a process might not be similar to that obtained through the DSM operation, in which the sediment passes through the SMT for a brief period of time exposed to high shear rates. In experiments with flocculant, the flocculant was added and stirred for 30 seconds before opening the lock.

3.3. RESULTS AND DISCUSSION

3.3.1. DISTANCE TRAVELLED BY PLUME HEADS

The 10, 30, and 100 gL^{-1} illite experiments are displayed in Figure 3.2 in terms of the distance travelled by the turbidity current within the video recording range. When no flocculant is used, there is no significant difference observed between experiments conducted in fresh and saltwater and the turbidity current without added flocculant reached the lock exchange's end in all experiments. The current's head velocity scales as the square root of the plume density, as is expected (Huppert, 2006). Salt-induced flocculation time is in the order of 15-30 minutes, even under ideal shear circumstances (Mietta, 2010). Therefore, no significant effect was observed over the experimental period of the current study (< 1 min). Similar results were obtained for both 10 and 30 gL^{-1} experiments done with ACCZ (see Figure 3.3).

Due to the effect of flocculation, the distance travelled in saltwater experiments with flocculant for all clay concentrations was reduced considerably. Figures 3.2 and 3.3 show results for the experiments 0.75 mg/g flocculant where the sediment plume did not reach the lock exchange's endpoint and settled inside the outflow section. For the experiment done in freshwater with flocculant, the sediment plume reached the end of the outflow section or nearly half of the outflow section. The weak flocculation in freshwater accounts for this difference between fresh and saline water experiments. Even though both clay and flocculant have a negative charge, making flocculation difficult, freshwater contains enough cations to promote flocculation (Sanz, 2018). The cation concentration in saltwater promotes flocculation, especially as the cation chosen (Ca^{2+}) is divalent (Chassagne, 2020; Shakeel et al., 2020). For 100 gL^{-1} experiment with illite, it is observed that the system did not properly flocculate as in all cases, the sediment plume reached the end of the outflow section with the same speed, and flocculation had little to no effect on macroscopic scale.

The results using 0.25 mgg^{-1} flocculant are given in Figures A.1 and A.2, and in all cases (illite or ACCZ), the sediment plume reached the end of the outflow section except for one case (10 gL^{-1} ACCZ in saltwater). The results in the 0.25 mgg^{-1} case hint that the low concentration of flocculant has less impact on the plume propagation.

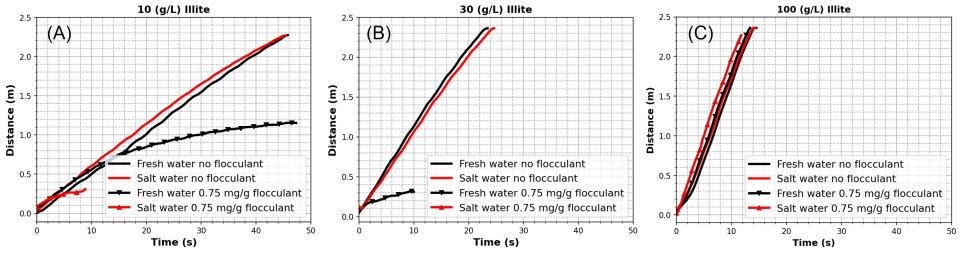


Figure 3.2: Change in distance as a function of time for 10 gL^{-1} (A), 30 gL^{-1} (B) and 100 gL^{-1} (C) of illite. Black lines represent experiments done in freshwater, and red lines show experiments done in saltwater. Only results with 0.75 mgg^{-1} of flocculant are shown in these figures.

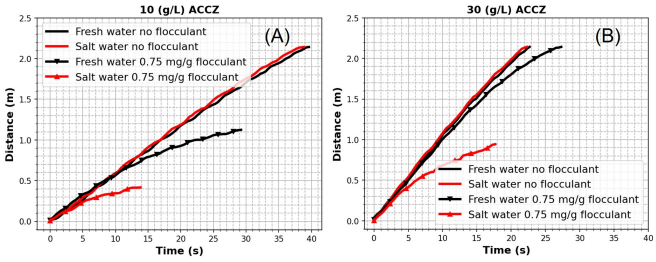


Figure 3.3: Change in distance as a function of time for 10 gL^{-1} (A) and 30 gL^{-1} (B) of ACCZ (Ali et al., 2022a). Black lines represent experiments done in freshwater, and red lines show experiments done in saltwater. Only results with 0.75 mgg^{-1} of flocculant are shown in these figures.

3

3.3.2. MEAN FLOC SIZE AS FUNCTION OF TRAVEL DISTANCE

Figure 3.4 (Illite) and Figure 3.5 (ACCZ) show the mean floc size of the samples taken at locations L1–L4. No flocculation occurred without the flocculant in both fresh and saltwater, as for each location, the d_{50} was found equal to the mean clay size. For both experiments with illite, d_{50} was found to be around 5 µm at all locations, whereas for the experiment with ACCZ, it was found to be between 12-20 µm. These sizes are in line with the d_{50} found by SLS (5 and 10-20 µm respectively, see section 3.2.1). The bars given in Figures 3.4 and 3.5 (A) represent the standard deviation around the mean floc size based on the SLS device, whereas the box plots in Figures 3.4 and 3.5 (B) represent the median particle sizes with interquartile range and outliers based on FLOCCAM.

In the presence of flocculant, it was found that freshwater flocs were larger than saltwater flocs. Because of the electrostatic repulsion between the charged groups on the polymeric flocculant backbones, the flocculant in freshwater is less coiled in fresh than in salt water (Chassagne, 2020). As a result of shear during propagation, it is observed that the d_{50} of flocs created in saltwater with illite clay reduced as a function of travel distance. This difference is not observed for the ACCZ clay (Figures 3.4 and 3.5).

The results obtained with 0.25 mgg^{-1} flocculant are shown in the Figures A.3 and A.4, where the difference in flocs size in fresh and saltwater is not significant.

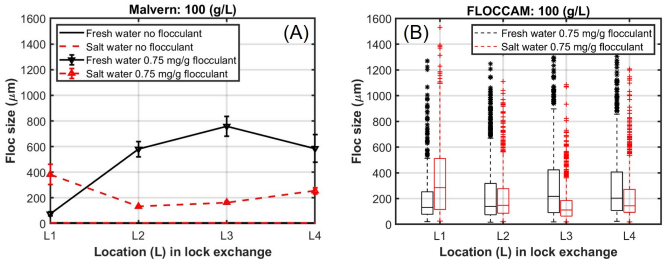


Figure 3.4: Hydrodynamic diameter of illite flocs for 100 gL^{-1} experiments at L1-L4 locations of the lock exchange. Figure A, results obtained by SLS and Figure B, results obtained from FLOCCAM. Black and red lines represent experiments done in freshwater and saltwater, respectively. Only results with 0.75 mgg^{-1} of flocculant are shown.

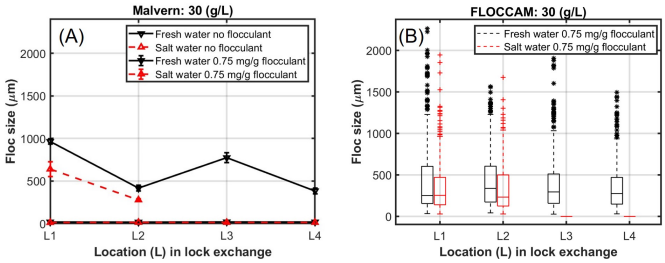


Figure 3.5: Hydrodynamic diameter of ACCZ flocs for 30 $g L^{-1}$ experiments at L1-L4 locations of the lock exchange Ali et al., 2022a. Figure A, results obtained by SLS and Figure B, results obtained from FLOCCAM. Black and red lines represent experiments done in freshwater and saltwater, respectively. Only results with 0.75 $mg g^{-1}$ of flocculant are shown.

3.3.3. SETTLING VELOCITY DISTRIBUTIONS AS FUNCTION OF SIZE AND TRAVEL DISTANCE

Figures 3.6 and 3.7 show the settling velocities and particle size for 100 $g L^{-1}$ illite with 0.75 $mg g^{-1}$ flocculant at L1 and L4 for freshwater and saltwater, respectively. Figures 3.8 and 3.9 show the settling velocities and particle size for 30 $g L^{-1}$ ACCZ with 0.75 $mg g^{-1}$ of flocculant at sites L1 and L4 (for freshwater) and L1 and L2 (for saltwater), respectively. At the point when the turbidity current settles down, on average, the settling velocities in freshwater are smaller than in saltwater. This is due to the fact that the flocculant is less coiled in freshwater than in saltwater (Chassagne, 2020), where flocs are denser and have a faster settling velocity. This was confirmed by the video images (see Figures 3.6 and 3.7 (A,D)).

The settling velocities increased in the case of saltwater for 100 $g L^{-1}$ illite between L1 and L4, as a result of coiling, flocs got compacted right after opening the lock (Figure 3.7). In the case of 30 $g L^{-1}$ ACCZ, the settling behaviour and floc size for the saltwater sample did not change between L1 and L2, indicating that optimum flocculation (Shakeel et al., 2020) has occurred in the mixing tank. The bridging between anionic polyelectrolyte and clay is complete because of saltwater cations. The flocculation in the mixing tank for the freshwater sample is most likely incomplete due to the scarcity of cations. Flocs, clay particles, and unbounded flocculant are released when the lock is opened. Freshwater containing cations comes into contact with the clay particles and unbounded flocculant. Because polyelectrolyte flocculation is quick (on the scale of seconds) (Ali and Chassagne, 2022; Sanz, 2018; Shakeel et al., 2020), these cations can act as a binding agent, inducing flocculation. As a result, flocs form, resulting in a particle size change, as shown between L1 and L4. Several flocs formed during the propagation of the sediment plume in 30 $g L^{-1}$ ACCZ experiment in freshwater are observed to be elongated, resulting in flocs with larger equivalent diameters (shown by the red circle in Figure 3.8 (D)). Because they are formed of low-density uncoiled flocculant with some clay linked to it, these big flocs have a very slow settling velocity. These flocs were unable to catch more clay particles and coil due to their limited residence period in the water column. Coiling of flocs happens over longer periods of time when turbulent shear causes the polyelectrolyte's dangling ends to fall onto the floc. The flocs get rounder and denser as a result (Shakeel et al., 2020).

Our experiments show that the amount of flocculant needed correlates to clay concentration. In addition, the results obtained with $30\,\mathrm{g\,L^{-1}}$ with $0.75\,\mathrm{mg\,g^{-1}}$ combination results in a turbidity current that settles faster than other combinations. The results with $0.25\,\mathrm{mg\,g^{-1}}$ of flocculant are shown in Figures A.5 to A.8.

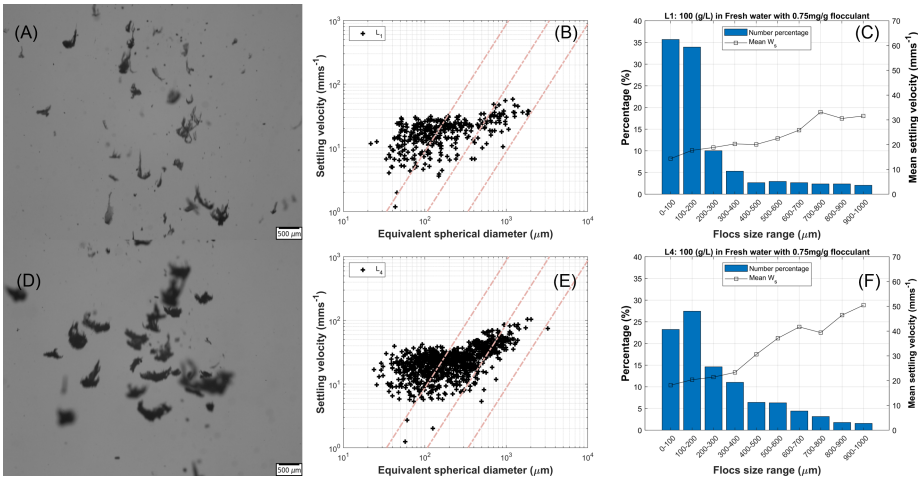


Figure 3.6: Figures (A,D) snapshots of the videos; Figures (B,E): Settling velocity and particle size analysis of the samples collected at location L1 and L4 during lock exchange experiments with $100\,\mathrm{g\,L^{-1}}$ illite and $0.75\,\mathrm{mg\,g^{-1}}$ of flocculant in freshwater. Settling velocity is derived as a function of equivalent spherical diameter, with diagonal dashed lines representing the contours of effective density calculated by using Stokes equation (from left to right: 1600,160,16 ($\mathrm{kg\,m^{-3}}$)). Figures (C,F) show the floc size range and mean settling velocity.

3.4. CONCLUSIONS

Understanding the changes in the propagation of turbidity currents created by human interventions, such as dredging, trenching, and deep-sea mining, is crucial for anticipating, predicting and, where possible, reducing the related environmental impact. Understanding is also crucial for engineers to know in what way the equipment and processes could be optimized to minimize plume dispersion. Previous studies have demonstrated that the flocculation of organic matter to clay occurs in less than 1 minute in a series of laboratory experiments. In this work, the influence of flocculation on turbidity currents was studied inside a lock exchange, where the current propagation time was of the same order of magnitude. It was shown that in the presence of an organic flocculating agent (anionic polyelectrolyte), flocculation was promoted. It was found that in both fresh and saltwater, flocs can be formed in a matter of seconds with the flocculant used in this study. As a result, the sediment plume was able to settle more quickly. The synthetic flocculant used is a proxy for organic matter found in marine environments (usually also negatively charged). It remains to be investigated if the type of flocculant has a significant impact on flocculation. This will be possible once the organic matter found in our area of interest (i.e. the Clarion-Clipperton Zone) has been fully characterized.

The results presented in this chapter are generic and thus apply to a wide range of tur-

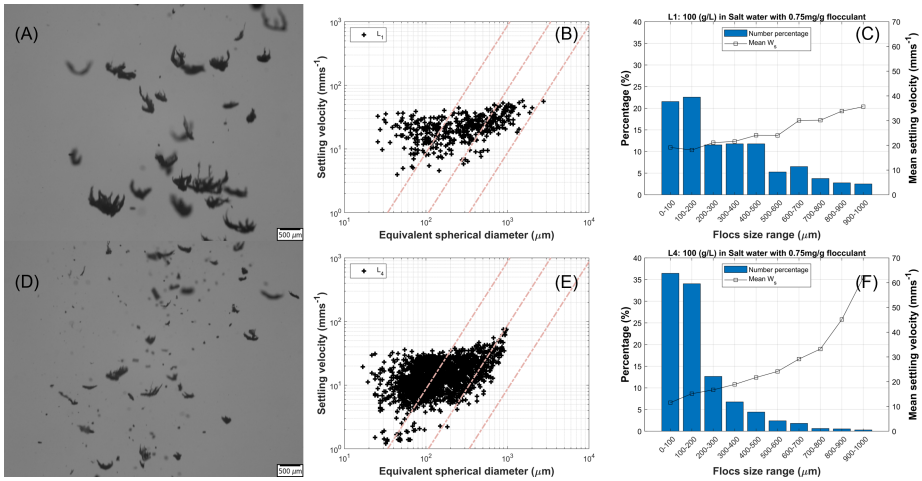


Figure 3.7: Figures (A,D) snapshots of the videos; Figures (B,E): Settling velocity and particle size analysis of the samples collected at location L1 and L4 during lock exchange experiments with 100 gL^{-1} illite and 0.75 mgg^{-1} of flocculant in saltwater. Settling velocity is derived as a function of equivalent spherical diameter, with diagonal dashed lines representing the contours of effective density calculated by using Stokes equation (from left to right: 1600,160,16 (kgm^{-3})). Figures (C,F) show the floc size range and mean settling velocity.

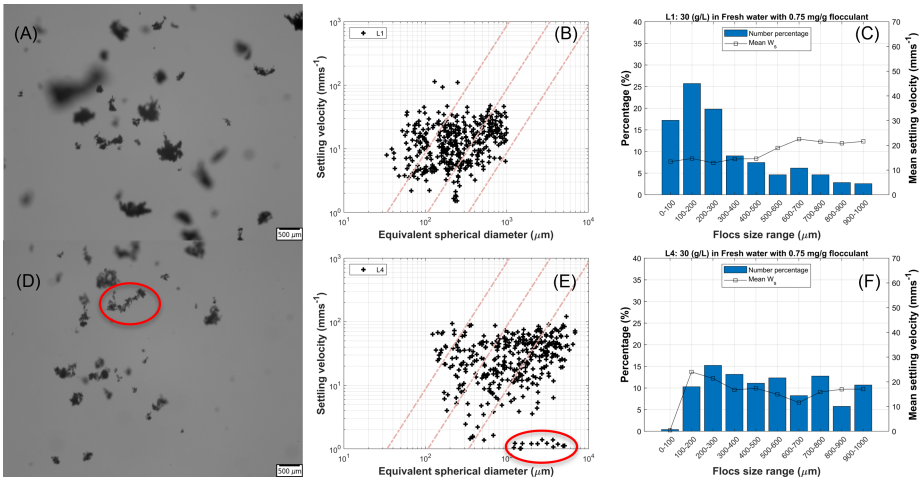


Figure 3.8: Figures (A,D) snapshots of the videos; Figures (B,E): Settling velocity and particle size analysis of the samples collected at location L1 and L4 during lock exchange experiments with 30 gL^{-1} ACCZ and 0.75 mgg^{-1} of flocculant in freshwater (Ali et al., 2022a). Settling velocity is derived as a function of equivalent spherical diameter, with diagonal dashed lines representing the contours of effective density calculated by using Stokes equation (from left to right: 1600,160,16 (kgm^{-3})). Figures (C,F) show the floc size range and mean settling velocity.

bidity currents. We demonstrated that flocculation may occur even in freshwater, where flocculation is supposed to be difficult because of the electrostatic repulsion between organic matter and clay. This means that flocculation should be accounted for in tur-

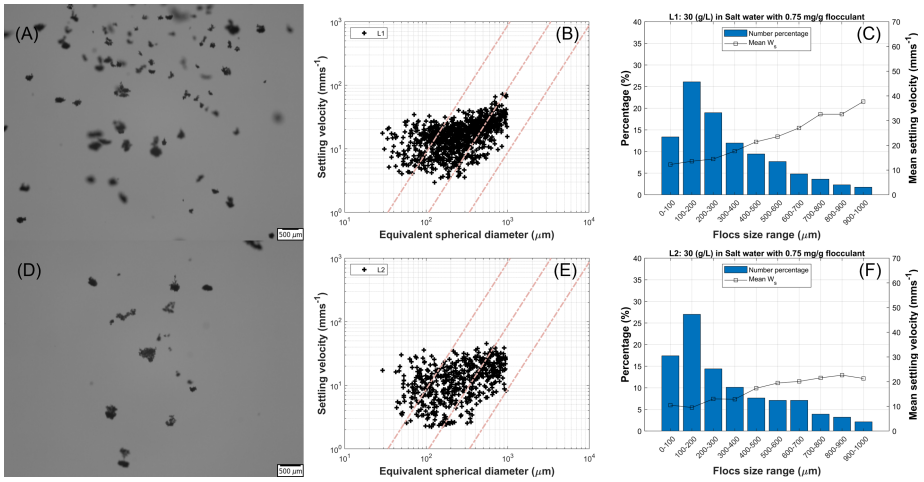


Figure 3.9: Figures (A,D) snapshots of the videos; Figures (B,E): Settling velocity and particle size analysis of the samples collected at location L1 and L2 during lock exchange experiments with 30 gL^{-1} ACCZ and 0.75 mgg^{-1} of flocculant in saltwater (Ali et al., 2022a). Settling velocity is derived as a function of equivalent spherical diameter, with diagonal dashed lines representing the contours of effective density calculated by using Stokes equation (from left to right: 1600,160,16 (kgm^{-3})). Figures (C,F) show the floc size range and mean settling velocity.

bidity current models. The obtained results demonstrate that flocculation is a relevant phenomenon that may already be contributing in the near field. Building experience with more conventional sediments allows us to better understand and design experiments with real CCZ sediment, which is the next step.

4

EFFECT OF THE CONCENTRATION ON SETTLING VELOCITY OF FLOCS

In Chapter 3, the impact of flocculation on turbidity currents generated through lock exchange is studied, whereby floc sizes and settling velocities play an important role. Mainly two types of methods to measure the size and settling velocities of cohesive sediment are traditionally used. Long-term assessments make use of in-situ laser diffraction techniques to evaluate particle size distribution and concentration of suspended material. Shorter-term campaigns employ onboard video microscopy in combination with a settling column. With this technique, individual particle size and settling velocity can be recorded, enabling the estimation of particle density, if Stokes law is assumed to be valid. This chapter's objective is to use such a high-magnification digital video camera alongside a settling column to investigate how particle concentration affects floc size and settling velocity. Illite clay flocculated using an anionic polyelectrolyte, is used in these experiments. It is found that the average settling velocity of flocs correlates with the concentration of transferred flocs. This implies that the application of Stokes settling velocity to estimate the density of flocs during batch settling, as is done in practice, is not appropriate and usually leads to very large errors (the effective density for the smallest particles can be 10 times smaller than the ones estimated). Even the settling velocity of the largest flocs is influenced by the presence of neighbouring particles.

This chapter is submitted for publication and is under review.

4.1. INTRODUCTION

THE size and settling velocity of flocs are significantly larger than those of individual (smaller) mineral sediment particles, but their density is generally lower (Dyer and Manning, 1999; McDowell and O'Connor, 1977). The effective density of flocs is found to decrease as their size increases (Droppo et al., 2000; Khelifa and Hill, 2006; Klimpel and Hogg, 1986). In situ, the structure of flocs can vary significantly, from small aggregated clay particles to centimetre-long stringer-type flocs (Diercks and Asper, 1997; Safar, 2022). It is also found for in-situ flocs that there is a very large spread in settling velocity (and hence in density) for flocs in the range of 50-150 microns (Khelifa and Hill, 2006; Maggi, 2013; Safar, 2022). The settling velocity of solid unaggregated silt and clay is straightforwardly related to the grain size via the Stokes settling velocity equation. In contrast, the settling velocity of flocs depends on the floc size, effective density, shape, and porosity-all of which are subject to fast change in response to local changes in the water column (Dyer and Manning, 1999; Manning, 2004; Manning et al., 2010).

For long-time measurements, in situ laser-based diffraction techniques are used, such as the Sequoia Scientific Laser In-situ Scattering and Transmissometry (LISST) 100x and 200x, that measure particle size and volume concentration (Agrawal and Pottsmith, 2000). From this data, the density of particles can be estimated, and settling fluxes subsequently be derived, based on Stokes' law (Chassagne and Safar, 2020). It was shown that when flocs are heterogeneous in composition and have a non-spherical structure, the results obtained from LISST are subject to caution (Mikkelsen et al., 2005; Smith and Friedrichs, 2011). Furthermore, in salinity-driven pycnoclines where the Schlieren effect influences measured particle sizes, LISSTs may provide ambiguous data (Chapalain et al., 2019; Karageorgis et al., 2015). High particle concentrations are also a technical limitation (Zhao et al., 2018). For these reasons, additional monitoring campaigns are usually planned episodically during the long-time measurement series to sample particles from the water column and assess the properties of the suspended material using video microscopy-based techniques (Fall et al., 2021; Law et al., 1997; Manning, 2015; Manning et al., 2011). These techniques involve transferring a small quantity of the collected sample into a settling column. In our experiments, the particles are collected using a pipette with an aperture of 5 mm, which is large enough to minimize the breaking of the collected particles. The aperture of the pipette is brought into contact with the water surface, allowing the particles to settle under their own weight into the settling column. The particles are then recorded 10 cm above the bottom of the settling column while they are settling, and their size, shape and settling velocity are determined.

The objective of the work presented in this chapter is to estimate the dependency of the settling velocities on the concentration of the transferred particles. Indeed, it is known from studying the physics of the settling of a cloud of particles in quiescent water that the settling velocity of the cloud (also called "blob") is proportional to the number of particles inside the cloud (Guazzelli and Morris, 2011). The settling velocity of the blob is proportional to the density difference between the blob and the surrounding fluid. Consequently, the settling velocity of a particle in a blob can be orders of magnitude larger than the Stokes velocity of the same particle. The set-up used in our experiments makes use of the natural break-up of a blob upon settling. The blob usually evolves into a

torus and breaks into two smaller blobs, which themselves break-up. When the particles are recorded by the camera, it is postulated that each particle has reached its Stokes settling velocity and, hence, is not influenced by the presence of neighbouring particles. It remains to be investigated whether reasonable changes in particle concentration (we used 0.01 to 5.0 gL^{-1}) significantly influence the settling velocity. These concentrations are typically within the range that can be obtained when sampling at one location (Gillard, 2019; Van Leussen, 1999). In this work, mineral clay is flocculated (with the synthetic flocculant), and corresponding settling velocities and sizes were determined using the high-quality video-based setup. The chapter is organized as follows. Section 4.2 gives an overview of the materials used. Section 4.3 presents relevant results and discussion. Finally, conclusions are given in Section 4.4.

4.2. MATERIAL AND EXPERIMENTAL METHODS

4.2.1. CLAY

The illite clay used in the experiments was obtained as a dry powder from Argiletz laboratories. The d_{50} of illite particles was found to be around 5 µm (see Figure 4.1) by static light scattering (Figure 2.4).

Eight different clay concentrations (0.01, 0.025, 0.1, 0.5, 1.0, 1.5, 2.0 and 5.0 gL^{-1}) were used and flocculated by addition of flocculant, keeping the ratio of clay concentration to flocculant concentration constant. All suspensions were flocculated in a jar (Figure 2.2) for 1 hour at 50 s^{-1}. This shear rate was chosen so as to be able to produce large flocs. It was observed that for the samples with clay concentration below 0.1 gL^{-1}, the created flocs settled at the bottom of their respective jars within 5 min. The action of the paddle (located 5 cm above the bottom of the jar) then only mobilized them at the bottom of the jar for the remainder of the hour. For the samples with clay concentration above 0.1 gL^{-1}, the flocs were formed very rapidly and remained in suspension for the whole hour. After one hour of stirring, the stirrer was stopped, flocs settled and were sampled at the bottom of the jar.

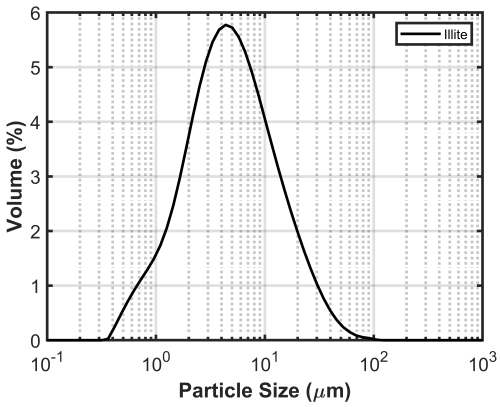


Figure 4.1: Particle size distribution of illite.

4.2.2. FLOCCULANT

Zetag 4110, an anionic polyacrylamide with a medium anionic charge and a high molecular weight, was used as a flocculant in this study. 2.5 mgg^{-1} flocculant to clay ratio was used for flocculation, which is close to the optimum dosage for this flocculant (Shakeel et al., 2020).

4.2.3. WATER

All suspensions were made using tap water. The composition of tap water provided by the drinking water company Evides is shown in Table 4.1 for the days the experiments were conducted.

Parameter	Value	Unit
pH	7.9-8.2	-
Bicarbonate (HCO3)	120-130	mg/L
Sulphate (SO4)	42-45	mg/L
Sodium (Na)	33-35	mg/L
Calcium (Ca)	44-45	mg/L
Magnesium (Mg)	6.9-7.3	mg/L
Chloride (Cl)	46-48	mg/L

Table 4.1: Tap water specifications.

4.3. RESULTS AND DISCUSSION

4.3.1. INDIVIDUAL VS COLLECTIVE SETTLING

The results of 5.0 gL^{-1} illite flocculated with 2.5 mgg^{-1} flocculant to clay ratio are shown in Figure 4.2. All the presented data are number averaged. The comparison between the settling velocities for the two cases ("collective and individual settling") is shown as boxplots for given size bins in Figure 4.2(A). "Collective settling" refers to experiments whereby a subsample of concentration 5.0 gL^{-1} was collected at the bottom of the jar and transferred into the settling column. The figure displays the results obtained for the analysis of three of such measurements. "Individual settling" refers to the experiments whereby very diluted amounts of the flocculated 5.0 gL^{-1} sample are transferred into the settling column. The figure displays the results obtained for the analysis of 5 of such measurements. The flocs selected for the data are the ones that were settling individually (i.e. that were alone in the field of view). The recorded data (settling velocity as a function of particle size for each floc analyzed) is shown in Figure B.1. It is found that in the case of collective settling, the settling velocity is much higher than for individual settling for all size classes. For individual settling, it is observed that the settling velocity is increasing with floc size, see Figure 4.2(A). For collective settling, broad ranges of settling velocities are found for each class of particle sizes. From the video recording, it could be observed that, indeed, flocs settling in the same frames had the same settling velocity, irrespective of their size. In Figure 4.3, the scatter plot of the settling velocity vs equivalent spherical floc size for the collective settling case at three different times during the settling are

shown, labelled “start” (first flocs to be recorded), “mid” (flocs recorded after the first flocs), and “end” (last flocs to be recorded). Snapshots taken during these different times are displayed in Figure B.3. There is no clear dependence of settling velocity as a function of particle size for any time (even though, as expected, particles settling fastest were observed in the start frames and particles settling slowest in the end frames). The mean settling velocity of flocs found in the size range of 20-100 microns is similar to the settling velocity of bigger flocs(> 700 microns) for all times (“start”,“mid” or “end”). From these results, it can be concluded that small particles are always entrained in the wake of the large ones, matching their velocity.

Similar results were obtained by Dyer and Manning, 1999 for the settling velocity of flocs from the Tamar estuary: when only a few flocs are sampled (as in Figure 2, top graph in Dyer and Manning, 1999) the flocs have a settling velocity that increases with floc size, following a constant effective iso-density line of 16 $\mathrm{kg\,m^{-3}}$. When a lot of flocs are sampled (as in Figure 2, the bottom graph in Dyer and Manning, 1999), a large horizontal band of points, representing flocs of sizes in the range 20-500 microns are found in the range of 10 $\mathrm{mm\,s^{-1}}$. This implies that flocs of sizes smaller than 100 microns would have an equivalent effective density much larger than 1600 $\mathrm{kg\,m^{-3}}$ if the Stokes settling formula is applied. Dyer and Manning, 1999 attribute this very high density to the presence of crystals of hornblende and tourmaline, which indeed can have densities as high as 3400 $\mathrm{kg\,m^{-3}}$. However, for 50 microns particles reaching 10 $\mathrm{mm\,s^{-1}}$, it would imply that these particles have a density of 8600 $\mathrm{kg\,m^{-3}}$ (density of brass), which would be unlikely.

Using Stokes equation, the effective density of flocs was estimated, which is shown in Figure 4.2(B-E). The curves in each figure represent the fit according to the equation in insert. For the settling of individual particles, an exponent of n=1.178 is found. In literature, this exponent is often linked to a fractal dimension (Winterwerp, 1998). A fractal dimension as low as 1.178 would indicate that the flocs are very elongated (nearly linear), which is not the case in our experiments (see Figures B.3 and B.4). A discussion about fractal dimension is given in Chassagne, 2021. From video analysis, it was found that the mean aspect ratio of flocs in both individual and collective settling case is 0.7 (see Figure 4.2(F)), indicating that the flocs are rather spherical. However, in both cases (and especially in the collective settling case), some flocs were observed to be obtained from differential settling in the column, see some of the snapshots in see Figure B.3. In line with the literature (Droppo et al., 2000; Khelifa and Hill, 2006; Klimpel and Hogg, 1986), it is seen that the effective density of flocs decreases as their size increases. It is found that the values for density are higher in the collective settling case as compared to the individual settling case, as can also easily be deduced from the settling velocities displayed in Figure 4.2(A). In Figure 4.2(B,C) the effective density is fitted not accounting for the first bin size of 0-100 microns. By comparing the values obtained for the fits with the ones obtained by fitting all bin sizes (Figure 4.2(D,E)), it is found that the exponent “n” varies significantly in both collective and individual settling cases. This variation is due to the large spread in density for flocs in the 0-100 microns size range. The effective density for particles in the 0-100 micron range varies from 1063 $\mathrm{kg\,m^{-3}}$ to 9460 $\mathrm{kg\,m^{-3}}$ for individual settling and varies from 1828 $\mathrm{kg\,m^{-3}}$ to 150×10^3 $\mathrm{kg\,m^{-3}}$ for collective settling. The highest effective densities are found for the smallest particles. For these particles

(around 20 microns in size), the camera detection limit has been reached. As the Stokes settling velocity is a function of the particle size squared, an error in size leads to large errors in the calculated density.

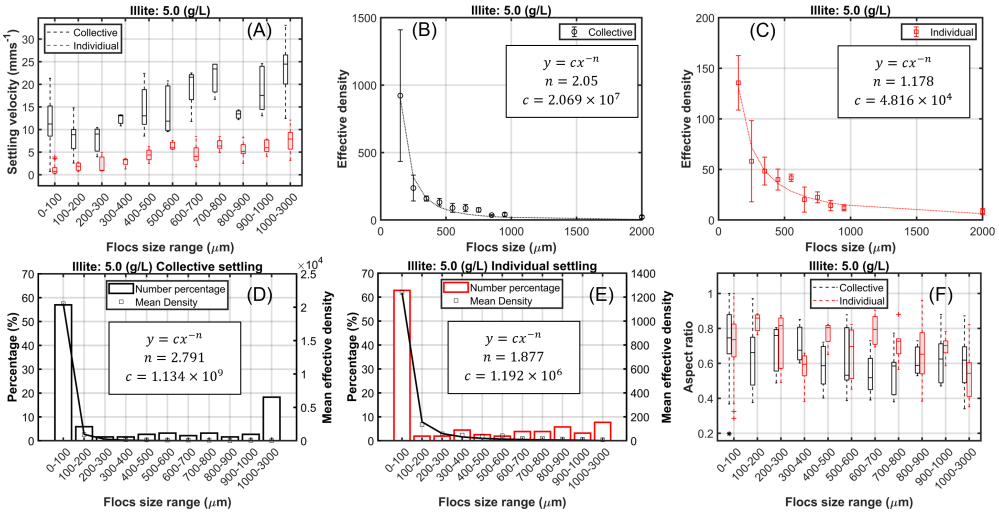


Figure 4.2: A): Settling velocity of 5 gL^{-1} experiment for both collective and individual settling cases for different floc size ranges. B,C): Effective density as a function of the floc size range for both collective and individual cases. The fit is performed for floc sizes above 100 microns. D,E): Mean effective density for different classes of floc size for both collective and individual cases. The fit is performed by accounting for all size classes. The value of the fit parameter is given in each figure. F): Aspect ratio as a function of floc size for both collective and individual settling cases.

4.3.2. CLAY CONCENTRATION DEPENDENCE

For the results presented in this section, subsamples of flocculated material were carefully collected at the bottom of the jars and transferred into the settling column ("collective settling"). The distribution in floc size (boxplots) for the investigated clay concentrations are shown in Figure 4.4. The settling velocities as a function of particle size are shown in Figure B.2. For concentrations up to 0.1 gL^{-1}, it was observed that flocs formed and settled at the bottom of the jar within 5 min. This results in floc size distributions being very similar for these low concentrations. It also indicates that flocs did not further flocculate once they had settled at the bottom of the jar, despite the action of the stirrer that agitated the water for one hour: contacts between flocs at the bottom of the jar did not result in significant sticking between flocs. For concentrations larger than 0.1 gL^{-1}, large flocs could be formed rapidly, resulting in flocs with a density low enough to keep them in suspension for an hour. Large floc sizes are, therefore, observed at high clay concentrations. Figure 4.5 shows the settling velocity for different concentrations of clay for the floc size ranges 20-100 µm and 900-1000 µm. Larger settling velocities are found above 0.1 gL^{-1} for particles in the 20-100 µm range, indicating that both larger flocs are formed in that size range and that collective settling is playing a role, as small particles follow in the wake of the large flocs formed above 0.1 gL^{-1}. This was verified by

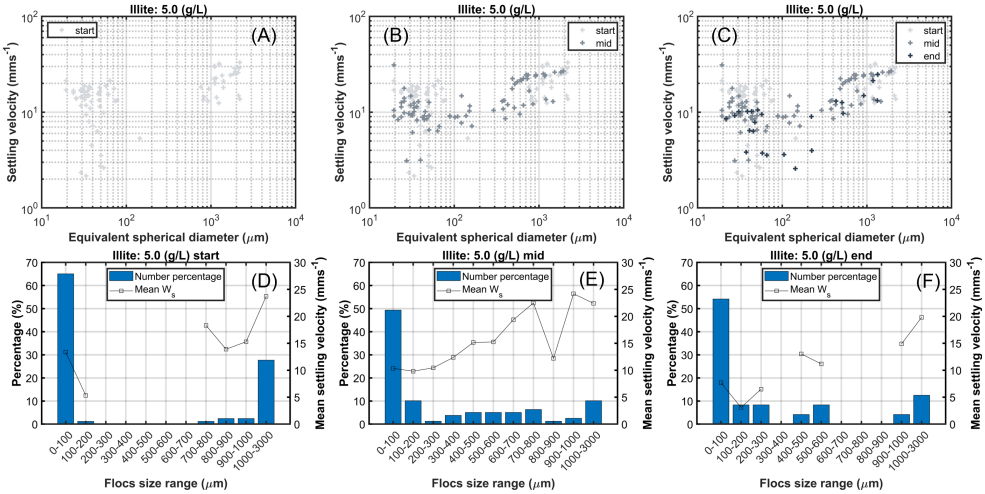


Figure 4.3: A-C) Settling velocity and particle size analysis of 5 gL^{-1} experiment at three different times, e.g. start, middle and end. Settling velocity is plotted as a function of equivalent spherical diameter, with diagonal dashed lines representing effective density iso-lines calculated by using Stokes equation (from left to right: 1600,160,16 (kgm^{-3})). D-F) show floc size range and mean settling velocity corresponding to A-C respectively.

the analysis of the recorded videos. From Figure 4.5(B), it can be seen that in the 900-1000 µm class, there are no flocs for concentrations less than 0.5 gL^{-1} and that flocs are rather monodisperse. This implies that all the flocs settle at the same settling velocity.

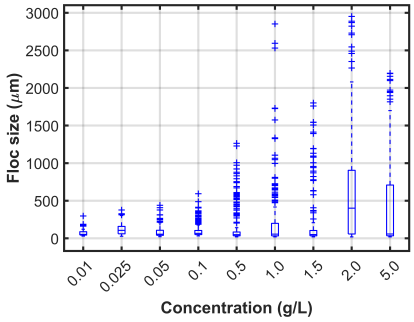


Figure 4.4: Floc size plotted for different concentrations.

4.4. CONCLUSIONS

In this work, a video-based setup is used to study the effect of clay concentration on floc size and, particularly, on the flocs' settling velocities. It was shown that the sampling method used is of great importance to obtain a Stokes settling velocity for each floc. In order to prevent collective settling, whereby particles settle in batches and reach terminal velocities that are orders of magnitude larger than their individual Stokes settling velocity,

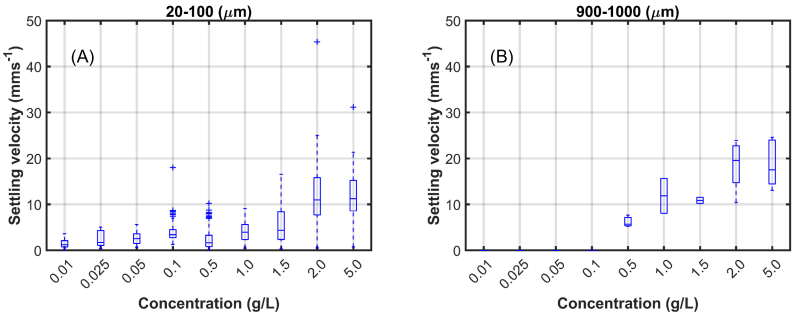


Figure 4.5: Mean settling velocity of illite for different concentrations. A) mean settling velocity of floc size range between 20-100 µm and B) mean settling velocity of floc size range between 900-1000 µm.

only time series where flocs are settling individually should be analysed. This requires carefully subsampling the population of flocs to decrease the concentration of flocs transferred into the settling column. It was, however, also shown that in the case where flocs are rather monodisperse, such subsampling is not necessary, as all flocs then have a similar settling velocity. It was found that both size and settling velocities depend on clay concentration, even though the same flocculant to clay ratio was used to generate the flocs. The reason is linked to flocculation kinetics: at large clay concentrations, (large) flocs can be formed rapidly. At lower clay concentrations, the flocculation kinetics are slower and thus flocs settle to the bottom of the jar within 5 min at mixing clay and flocculant. This is reflected in the density of flocs: large flocs (that remain in suspension in the jar) have a very low density (their effective density is in the range 10-30 $\mathrm{kg\,m^{-3}}$) whereas small flocs (relatively containing more clay) have, on average, a ten times higher relative density. This result can be of interest for the study of in-situ flocculation. Most flocculation occurs in regions of high fine sediment concentration, such as in the water body close to the sediment bed. Not only the flocculant (organic matter) to clay ratio but also clay concentration in the water column are therefore factors determining both the size and density of the floc. At high clay concentrations, flocculation will occur at short timescales (minutes), and large flocs with low density will be formed, that can be transported over large distances. At moderate/low clay concentration smaller and denser flocs will be formed. Further growth of these flocs will be prevented as these flocs will rapidly settle onto the bed. The use of a video image-based device to record floc sizes also enables to pinpointing of the shortcomings of laser diffraction particle sizers for flocs. Flocs have a strong size-dependent density, linked to the fact that flocs of larger sizes contain more flocculant. Consequently, flocs have a size-dependent refractive index. Large flocs also have a complex structure. It is, therefore, not yet clear what errors are made by converting the scattered data into particle sizes. The combined use of video microscopy and laser diffraction techniques will, in the future, enable us to answer this question.

5

FLOCCULATION AND SETTLING OF DEEP-SEA CLAY FROM THE CLARION CLIPPERTON FRACTURE ZONE

This chapter focuses on studying the effect of in-situ conditions on the flocculation of deep-sea clay, using samples from different areas within the Clarion Clipperton Fracture Zone (CCFZ). This chapter pinpoints the role of several key parameters, including temperature, concentration, shear and resting time, on the flocculation process. It is found that temperature does not play a major role in the flocculation of deep-sea clay. Therefore the flocculation of deep sea clay can be studied in laboratory conditions. The experiments show that deep-sea mineral clay quickly undergoes flocculation within a few minutes due to the presence of natural organic matter. A threshold shear rate of around $125\,s^{-1}$ *is found. Above this shear, organic matter effectively binds to clay, leading to a linear increase in steady-state floc size with shear. Below* $125\,s^{-1}$*, the median floc sizes decrease with shear. The residence time of flocs at the bottom of a jar experiments also pinpoints the fact that the organic matter in the deep sea has a hydrophobic nature. This would imply that at low shear the organic matter is in a coiled state and that flocculation is minimized, whereas at higher shear, the organic matter extends in solution and, thanks to an increased collision frequency, flocculation is promoted.*

This chapter is submitted for publication and is under review.

5.1. INTRODUCTION

Below the permanent thermocline in the ocean interior, where currents are significantly weakened, the dominant process driving particle aggregation at these low shears is differential settling, which leads to the formation of large flocs known as marine snow (Alldredge and Silver, 1988). Marine snow is mainly composed of organic matter, such as dead phytoplankton, faecal matter, and natural polymers produced by bacteria and phytoplankton. Most parts of marine snow are consumed by filter-feeding animals within the first 1,000 metres of their sinking. The composition of the sediments in the seabed differs depending on the location and formation factors. Typically, they contain clay, silt, sand, rock fragments, and organic material (BGR Environmental Impact Assessment, 2019; Lang et al., 2019; Zawadzki et al., 2020). Less than 0.5 percent of the sediment bulk is made up of carbon in the top few centimetres of the CCZ sediment. This decreases to 0.1 percent of the sediment's mass below 30 cm (Volz et al., 2018). As discussed on pages 25-26, only a few milligrams of organic matter per gram of clay is required for substantial flocculation.

The abyssal plains of the deep sea possess vast reserves of polymetallic nodules, which, unlike on land, comprise a range of metals in a single deposit. In the Clarion Clipperton Fracture Zone (CCFZ), a large area abundant in these nodules, cobalt, nickel, copper, and manganese, are all present in a single ore (Harbour et al., 2020; Hein et al., 2020; ISA, 2019). There is at present a high demand for metals, such as manganese, nickel, and cobalt, which are necessary for the manufacture of wind turbines, solar panels, and batteries for electric cars (Hein et al., 2020). While these precious metals are typically extracted through land-based mining, deep-sea mining is being viewed as a possible alternative to satisfy the growing demand. However, it is crucial to recognise the environmental consequences of the associated dredging operations, which have the ability to disrupt benthic ecosystems and produce sediment plumes with a high concentration of suspended solids (Kaiser et al., 2013; Peacock and Alford, 2018).

Within the context of deep-sea mining, the nodule mining procedure involves the usage of the Seafloor Mining Tool (SMT), which gathers nodules from the seafloor and separates them from unnecessary water and sediments. During this process, the leftover water and sediment are discharged behind the mining vehicle on the seafloor. The generation of turbidity currents within the near-field region is of particular interest due to its presumed environmental impact in the mining operation. Various flow regimes, including jets, plumes, and turbidity currents corresponding to the ones generated by the SMT have been studied (Ali et al., 2022a; Elerian et al., 2022; Haalboom et al., 2022; Hein et al., 2020; Nodules, 2020; Peacock and Ouillon, 2023). It was found that passive plumes, resulting from entrainment of the turbidity current by the overlying movement of water, could potentially remain suspended for extended periods (Gillard, 2019; Haalboom et al., 2022; Hein et al., 2020; Nodules, 2020). Their settling and subsequent smothering effect could potentially result in the burial of benthic species, hindrance of respiratory surfaces for filter feeders, and contamination of food sources for numerous benthic organisms (Gollner et al., 2017; Jones et al., 2017; Van Reusel et al., 2016).

When studying the propagation of turbidity currents, it was found that flocculation

indeed occurs during the propagation of the sediment (Ali and Chassagne, 2022), thanks to the fast flocculation kinetics resulting from organic matter - clay interactions. This flocculation significantly impacts the propagation of turbidity currents and sediment plumes (Elerian, 2023). In the context of deep-sea clay, the work done by Gillard et al., 2019 showed that at a low shear rate, at a concentration of 0.5 gL^{-1} deep sea clay is flocculating. There is, however, not yet any data available for a wide range of deep-sea clay concentration and shear rates, which are representative of the shear rates, mixing times and concentrations found during mining operations.

The aim of the present study is to investigate the effect of in-situ conditions on the flocculation of deep-sea clay, using samples from different areas within the Clarion Clipperton Fracture Zone (CCFZ). This chapter pinpoints the role of several key parameters, including temperature, concentration, shear and resting time, on the flocculation process. A series of flocculation experiments were conducted using jars, with variations in mixing times, clay concentrations, and shear rates. The influence of the flocs' residence time at the bottom of the jars was also studied. In addition, flocculation experiments at very low shear, resulting in differential settling, were conducted in a novel rotating wheel setup. Particle sizes and their associated settling velocities were measured using an in-house video microscopy set-up coupled with a settling column.

The chapter is structured as follows: materials used are given in Section 5.2. Results and discussions are presented in Section 5.3. Finally, conclusions are summarized in Section 5.4.

5.2. MATERIAL AND EXPERIMENTAL METHODS

5.2.1. CLAY

Two types of clay were used for the experiments; both were collected from two different areas of the Clarion-Clipperton Fracture Zone (CCFZ) at a water depth of approximately 4000 metres. For convenience, we refer to them as Clay 1 and Clay 2. Clay 1 was collected from the German licensing area of CCFZ, while Clay 2 was collected from the NORI-D area of CCFZ. The total organic carbon (TOC) was calculated from the difference between total carbon (TC) and total inorganic carbon (TIC). The TC was measured by utilizing a UNICUBE device made by Elementar Analysensysteme GmbH, while TIC was determined by gas chromatography and acid digestion. TOC in Clay 1 is approximately 0.53 wt.%, and for Clay 2 is 0.55 wt.%. The TOC values align with those observed in previous research conducted in the CCFZ region (BGR Environmental Impact Assessment, 2019). The Clay 1 and Clay 2 samples have a d_{50} around 20 µm, determined through static light scattering, using a Malvern Master Sizer 2000 (Ali and Chassagne, 2022). The Particle size distribution (PSD) before and after the removal (by using loss on ignition method) of organic matter can be found in Figure 5.1. Both Clay 1 and Clay 2 were used as received, implying that no organic matter was removed from the samples.

5.2.2. FLOCCULATION EXPERIMENTS IN A JAR

The flocculation experiments were carried out at room temperature with different clay concentrations and mixing times. The measurements were performed in a JLT6 jar setup

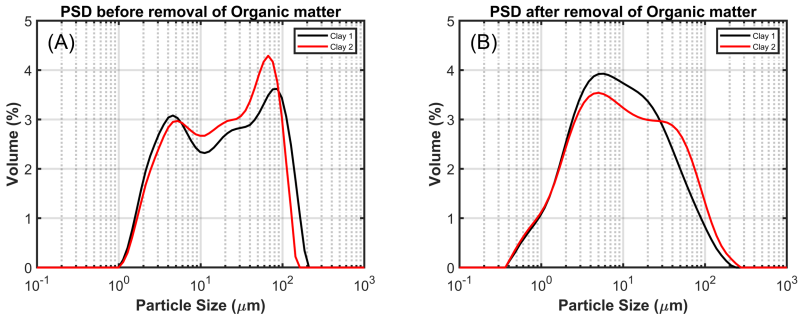


Figure 5.1: PSD of Clay 1 and Clay 2 collected from CCFZ. A) Shows the PSD before the removal of organic matter, whereas (B) shows PSD after the removal of organic matter.

provided by VELP Scientifica, Italy. The jars have dimensions of 95 mm in diameter and 110 mm in height. To stir each suspension, a rectangular paddle was used, measuring 25 mm in height and 75 mm in diameter. The paddle was positioned 10 mm above the bottom of the jar within the suspension. The shear rate employed for the flocculation experiments remained constant at 50 s^{-1}, and the clay was mixed in saline water, having a salinity of 34.68 PSU, which is equivalent to the average salinity of the ocean water. For practical reasons, the saline water was made using NaCl salt (analytical grade, provided by Boom Laboratorium, The Netherlands) and tap water, and some tests with artificial seawater showed that the results are most probably representative of seawater conditions. Other tests showed that the clays did not flocculate in tap water, which highlights the role of salt in flocculation. All clays were fully dispersed in saline water prior to the measurements, as the clay received was in the form of a compact, fully saturated lump (see Figure C.1). To ensure a full dispersion, the required amount of clay was taken from the lump and put in a jar. Then, saline water was added to achieve the desired concentration. The full dispersion of the clay was achieved using a high-stirring mixer with a speed of about 600 RPM for 60 minutes. This protocol was used for all experiments presented in this chapter.

Based on the amount of clay available for experiments, for Clay 1, five different concentrations (0.5, 1.0, 1.5, 2.0, and 5.0 gL^{-1}) were used. Regarding Clay 1, experiments were performed at seven different mixing times (2.5, 5, 10, 30, 60, 90, and 120 minutes). For Clay 2, three concentrations (0.5, 2.0, and 5.0 gL^{-1}) and four mixing times were used (2.5, 30, 60, and 120 minutes). After mixing, the paddle rotation was stopped, and flocs were left to settle to the bottom of the jar for about one hour. The flocs were then carefully collected using a pipette and deposited at the top of the settling column used in the FLOCCAM set-up. The sampling was done in at least three different locations in the jar, and all the data presented incorporated the results of these locations. When collecting samples, a modified pipette with a 50 mL capacity and a 3 mm diameter was employed to extract a sub-sample of floc from the jar with great care. The sub-sample was then transferred directly to the settling chamber of the FLOCCAM, where the aperture of the pipette was in contact with the column water surface. This allowed the flocs to settle naturally and unaided, purely under the influence of gravity. Floc sizes and their corresponding settling

velocities were then measured using the FLOCCAM equipment described below.

5.2.3. SHEAR CYCLE EXPERIMENTS

Shear cycle experiments were conducted in order to investigate the influence of shear rate on the median floc size. Six shear rates (50, 125, 200, 275, 350 and 50 s^{-1}) were used in the shear cycle experiment as shown in Figure 5.2 for 5 gL^{-1}. Each shear step had a duration of 60 minutes to ensure that a steady-state floc size has been reached at the end of the step.

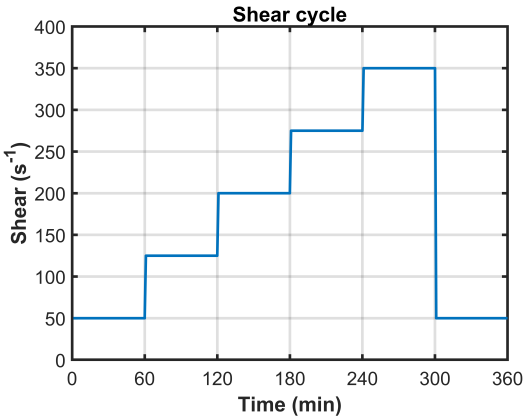


Figure 5.2: Schematic showing shear cycle experiment process.

5.2.4. RESIDENCE TIME AT THE BOTTOM OF THE JAR

Experiments were conducted to study the influence of the residence time of flocs at the bottom of the jar on their size. For Clay 1, various concentrations (0.5, 1.0, 1.5, 2.0, and 5.0 gL^{-1}) were tested. The samples were flocculated in the jar for a duration of 1 hour and then placed in a refrigerator at a temperature of 6 $°C$. The size of the flocs (collected from the bottom of the jar) was measured on days 1, 2, 10, and 30. Regarding Clay 2, two experiments were performed at a concentration of 0.5 gL^{-1}. One jar was placed in the refrigerator at a temperature of 6 $°C$, while the other jar was kept at room temperature (21 $°C$). The size of the flocs (collected from the bottom of the jar) was measured on days 1, 2, 10, and 30.

5.2.5. ROTATING WHEEL EXPERIMENT

Experiments in a novel in-house set-up known as a rotating wheel (Figure 2.3) were conducted to induce flocculation at low shear. The rotating wheel experiments were conducted with Clay 1 at a shear rate of 1 s^{-1}. The inner diameter of the wheel is 34 cm with a depth of 7 cm. The wheel was filled up to the top with suspension for all experiments. Three concentrations were considered (0.5, 2.0, and 5.0 gL^{-1}) with four mixing times (2.5, 30, 60, and 120 minutes). Floc size measurements of flocs created in the wheel and their corresponding settling velocities were also calculated after 2, 10, 20, and 30 days.

5.3. RESULTS AND DISCUSSION

5.3.1. INFLUENCE OF MIXING TIME AND CONCENTRATION

The effect of mixing time and clay concentration on flocculation are given in Figure 5.3. The median floc size for Clay 1 is compared with the median floc size of Clay 2 for different concentrations and mixing times, and it is clear that Clay 2 flocculates much faster than Clay 1 and has a higher median floc size in all cases (see Figure 5.3(G-I)). This can be attributed to the type of organic matter in Clay 2 since organic matter is the main driver for flocculation for natural sediments (Deng et al., 2019; Kranck, 1973; Lee et al., 2019; Mietta et al., 2009). Moreover, it has been observed that at low concentration, $0.5\,\mathrm{g\,L^{-1}}$, (see Figure 5.3(G)), the floc size of both clays increases with increasing mixing time, whereas for higher concentrations, the floc size decreases with increasing time (see Figure 5.3(H, I)). Figure 5.3 shows that at $0.5\,\mathrm{g\,L^{-1}}$, the size of the outliers increases over time (up to 120 minutes), indicating that the flocs formed are open and of the large structure. At 150 minutes of mixing time, both the median size and the size of the outliers (that was only measured for Clay 1) are smaller than at 120 minutes. Furthermore, for Clay 1 at $2.0\,\mathrm{g\,L^{-1}}$, the median size of flocs and the size of the outliers increase significantly between 2.5 and 5 minutes. After 5 minutes of mixing, the median floc size decreases with mixing time. This rapid growth, followed by a size decay, was already observed for clay flocculated using (cationic) polyelectrolyte (Shakeel et al., 2020). A characteristic size is given by the Kolmogorov microscale, which, for the shear rate used in the experiments (about $50\,\mathrm{s^{-1}}$), is of the order of 150–200 microns. Flocs having a size well below this range (as is the case for the $0.5\,\mathrm{g\,L^{-1}}$ experiments until about 100 minutes of mixing) can grow in time. Flocs having a size well above this range (as is the case for the experiments done at higher clay concentrations and for $0.5\,\mathrm{g\,L^{-1}}$ experiments above 100 minutes of mixing) reconform (by coiling the flocs get denser) or are eroded over time due to the experienced shear (Deng, 2022; Dyer, 1989).

It is also observed that Clay 1 and Clay 2 outliers have their size decreasing with mixing time until about 30 minutes of mixing, which is in line with the fact that the size of these outliers is well above the 150–200 micron size range estimated above. These outliers are, therefore, either reconforming or being eroded over time. After 30 minutes of mixing, however, the size of outliers is increasing again. The reason for this increase is related to an increase in “double flocs” (flocs made of two flocs attached together). Some of these double flocs are shown in the Figure C.2.

The mean settling velocities of flocs for different floc size ranges, concentrations and times are given in Figure 5.4. As detailed in (Ali et al., 2024), the measured settling velocities cannot be straightforwardly related to the Stokes settling velocity of flocs, as flocs usually fall in the wake of other flocs, which significantly influence the local hydrodynamics. We note that the mean settling velocity of flocs is clearly increasing with mixing time for all concentrations for Clay 2 flocs. No such trend can be observed for Clay 1 flocs, but the mean settling velocity is generally higher than for Clay 2 flocs. As Clay 2 flocs have an organic matter that differs from Clay 1 flocs, they are probably more prone to reconformation than Clay 1 flocs. Therefore, their density will increase with increasing shearing, which explains why their settling velocity increases with mixing time. As they contain less organic matter, Clay 1 flocs have a higher overall density and, therefore, a

higher settling velocity than Clay 2 flocs. The effect of floc reconformation is probably limited for Clay 1. For 2.0 gL^{-1}, while the mean floc size decreases with mixing time, the average settling velocity increases for all size ranges until 60 minutes of mixing, which is consistent with a reconformation and compaction of flocs. In contrast, the average settling velocity of Clay 1 flocs for all size ranges decreases overall for mixing times of more than 60 minutes. In particular, the fact that flocs in the 20–100 micron size range have a decreasing settling velocity with mixing time would agree with an erosion of flocs, whereby the eroded 20–100 micron flocs have a higher organic matter content than the original unflocculated 20–100 micron clay particles.

Analyzing the video microscopy data for the highest Clay 1 concentration, 2 and 5 g/L, it became clear that there was a complicating factor in the estimation of settling velocities, as long organic matter strings or swirls (see Figures C.2 and C.3) were observed in the videos. Clay particles could, therefore, experience sweep flocculation and be embedded in these long strings, which might also erode or break over time, contributing to lower settling velocities in each size range.

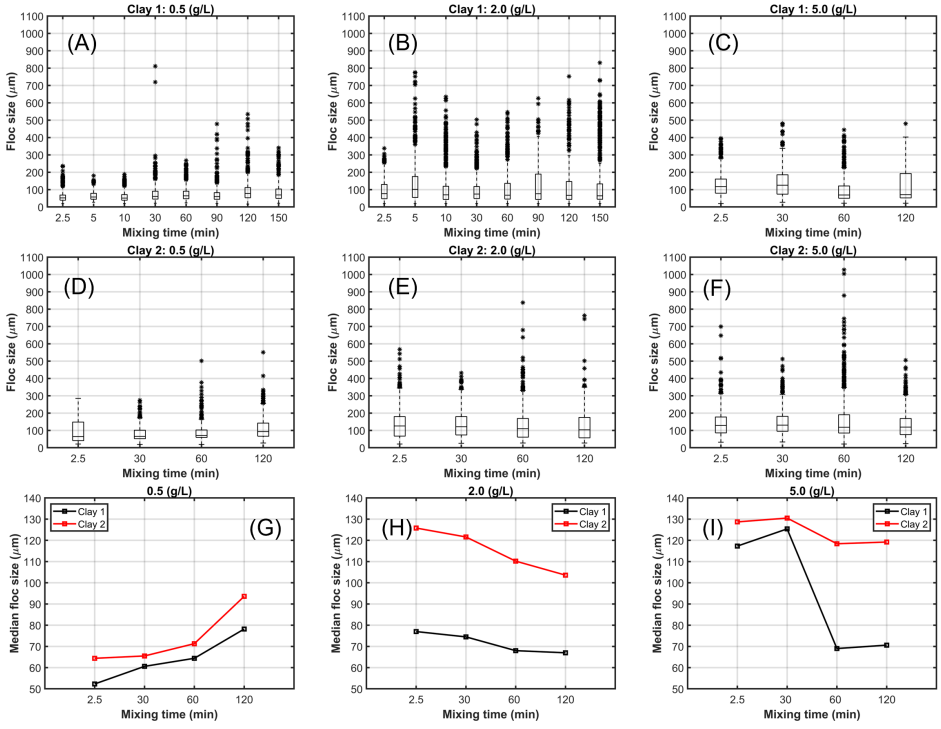


Figure 5.3: Effect of mixing time on flocculation of Clay 1 (A-C) and Clay 2 (D-F) concentrations of (A,D) 0.5 gL^{-1}, (B,E) 2.0 gL^{-1} and (C,F) 5.0 gL^{-1}. Median floc size for Clay 1 and Clay 2 concentrations of (G) 0.5 gL^{-1}, (H) 2.0 gL^{-1} and (I) 5.0 gL^{-1}.

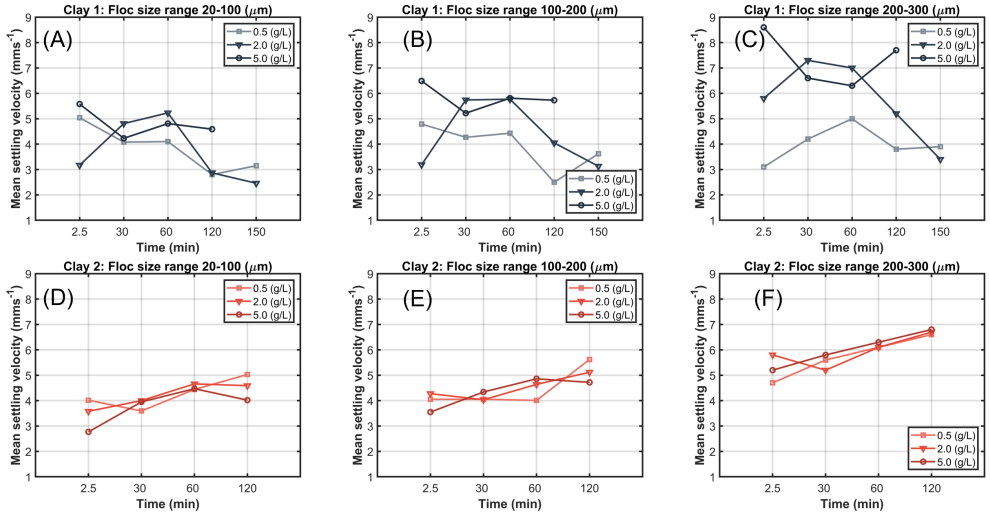


Figure 5.4: Mean settling velocity of flocs for different floc size ranges, concentrations and time for Clay 1 flocs (A-C), Clay 2 flocs (D-F).

5.3.2. SHEAR CYCLE EXPERIMENTS

The floc size distribution and median floc size for both Clay 1 and 2 are shown in Figure 5.5. Both clays show similar behaviour of median steady-state floc size as a function of shear. Due to its higher amount of organic matter, the Clay 2 floc sizes are always larger than the Clay 1 floc sizes. For both clays, it is observed that after the first shear step, the steady-state floc size decreases and then increases with increasing shear. The median floc size at 50 s^{-1} shear is the same before and after the shear cycle (see the green points in Figure 5.5(C), which symbolizes the 50 s^{-1} floc size measured at the end of the shear cycle). For Clay 1, however, it is observed that the size of the outliers after the shear cycle is smaller compared to the beginning of the shear cycle. For Clay 2, there is no significant change in outlier size.

A decrease in median floc size with shear is usually observed in shear experiments (Ali and Chassagne, 2022; Shakeel et al., 2020). When performing shear cycle experiments, it is found that the floc size is either reversible or non-reversible depending on the forces between the constituents of the flocs. If the interaction forces are weak enough, such as between anionic polyelectrolytes and negatively charged clay particles, the floc size is reversible as a stationary floc size is found for each shear rate (Shakeel et al., 2020). When the interaction is stronger, as is the case for flocs formed by cationic polyelectrolytes and negatively charged clay particles, flocs are irreversibly broken at high shear. This implies that, depending on the history of such a floc, different floc sizes can be found: A floc formed at low shear will usually be large, and if this floc has later been subjected to high shear and break, it will never regrow to this large size when the shear is again lowered.

In the flocs studied here, the stationary floc size increases with the shear rate after 125 s^{-1}. This contradicts the expected behaviour, which is a decrease in size with the shear rate.

We ascribe this peculiar behaviour to the specific type of organic matter in the samples. In the samples, we could observe organic matter polymeric chains that, over time, would bind to mineral clay or already flocculated material. In contrast to polyelectrolytes used as flocculants, which have very fast flocculation kinetics, it would seem that the organic matter present in the samples has slow flocculation kinetics. As shown in Figure 5.1, both Clay 1 and Clay 2 flocs contain a small amount of organic matter. However, the amount of organic matter bound or unbound to clay is unknown. We hypothesise that at a higher shear, the interactions between organic matter and mineral clay or between organic matter and flocs are enhanced, and therefore, the flocculation kinetics is promoted compared to a lower shear. At the same time, the decrease in median floc size observed between $50\,s^{-1}$ and $125\,s^{-1}$ and the fact that the steady-state size at $50\,s^{-1}$ at the end of the cycle is the same as the one found at the beginning of the cycle suggests that there is another mechanism at stake. This led us to conclude that the organic matter present in the samples has a low affinity for both water and clay, but that there is a higher affinity for clay than water, implying that at low shear, flocculation is prevented and explains why the steady-state size is decreasing between $50\,s^{-1}$ and $125\,s^{-1}$. At these low shears, the hydrophobic organic matter would be in a state of coiling that does not promote flocculation. At $125\,s^{-1}$, break-up (erosion of flocs) and/or reconformation of flocs lead to a smaller steady-state floc size. At higher shear rates, the organic matter uncoils, and aggregation is promoted. If our hypothesis is correct, it would mean that the steady-state size reached at each shear step is to be found by a balance between aggregation and break-up rates. The aggregation rate would be proportional to the collision frequency, which increases with shear and a small collision efficiency that would be shear-dependent (the collision efficiency being close to zero below $125\,s^{-1}$). The break-up rate would be more weakly dependent on shear than the aggregation rate since the median floc size increases steeply with shear.

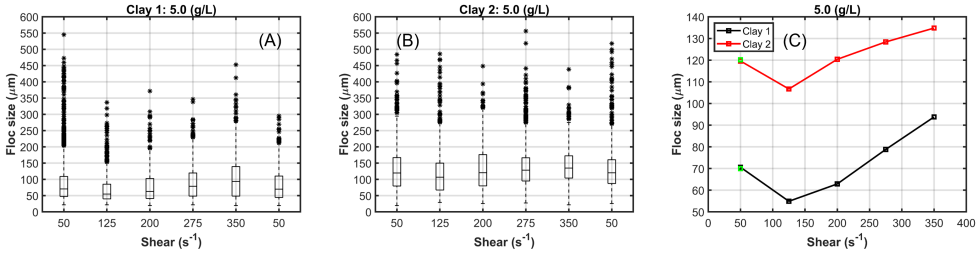


Figure 5.5: Effect of the shear cycle on floc size of Clay 1 (A) and Clay (B). Comparison of median floc size changes during the shear cycle in Clay 1 and 2 (C). The green point represents the values of median floc size at shear $50\,s^{-1}$ at the end of the shear cycle.

INFLUENCE OF RESIDENCE TIME AT THE BOTTOM OF THE JAR

Figure 5.6 shows the median floc size for Clay 1 and Clay 2 presented as a function of the time that flocs have been resting at the bottom of the jars. For Clay 1, it is found for all concentrations except $0.5\,gL^{-1}$ that the median floc size decreases slightly as a function of resting time. For $0.5\,gL^{-1}$ of Clay 1 and for all experiments with Clay 2 at the same concentration, an increase in floc size is observed until day 10, followed by a decrease in

size. From the experiments with Clay 2, it is concluded that temperature does not play a role in the observed trends, and therefore, neither does biological activity (which is temperature dependent).

It was observed while manipulating the jars containing the $0.5\,\mathrm{g\,L^{-1}}$ samples that flocs were not in contact with each other while resting but that the slightest movement induced flocculation, as flocs would roll, getting in contact with each other. The protocol for sampling the flocs was identical for all samples, so the small perturbations induced by the unavoidable handling of the jar and pipetting are expected to be the same for all samples. This is confirmed by the fact that all $0.5\,\mathrm{g\,L^{-1}}$ experiments are consistent. Until day 10, it would appear that the organic matter promotes a very rapid flocculation, as the handling of the jar is happening for a few minutes only. After day 10, breaking and/or reconformation of flocs is occurring. At concentrations above $0.5\,\mathrm{g\,L^{-1}}$, resting flocs are always in contact with each other at the bottom of the jars (see Figure C.4). If our hypothesis of the low affinity between organic matter and water is confirmed, it would imply that there is a structural energy benefit for organic matter to bind with clay at the moment two flocs are put into contact. On the other hand, when the flocs are in contact while resting at the bottom of the jar, the increase in size is minimal (though apparent, see day 2 for Clay 1 in Figure 5.6 (A)). At longer times (after day 2 in all cases), the median floc size decreases with resting time. It could be that the organic matter at that time, through a slow diffusion process, has been rearranging itself around the mineral clay particles in such a way as to minimize contact with water. This would lead to a breakage of flocs so as to increase the available clay surface area for the organic matter. Substances, like phospholipids, which are key components of cell membranes and are found in the deep sea (Parzanini et al., 2018), are a class of lipids that are surfactants (having a hydrophilic "head" containing a phosphate group and two hydrophobic "tails" derived from fatty acids). The properties of the organic matter in our samples (low affinity for water, high affinity for clay) would hint at the fact that it is a surfactant, like a phospholipid.

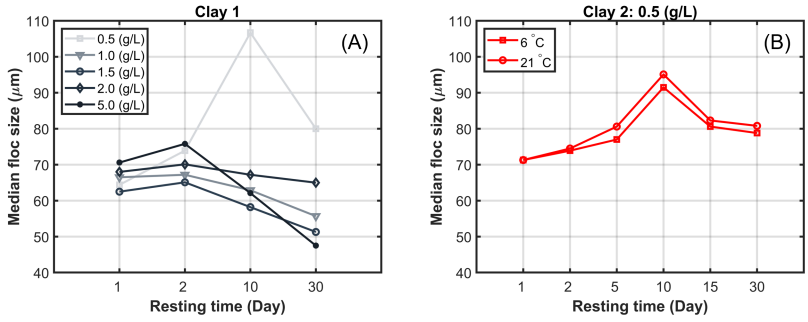


Figure 5.6: Effect of resting time of median floc size: (A) for Clay 1 at different concentrations and (B) for different temperatures.

FLOCCULATION IN THE WHEEL COMPARED TO JAR EXPERIMENT

Experiments with the wheel have been performed with Clay 1 only. During the slow rotation of the wheel, it was observed that the flocs residing at the bottom of the cylindrical

wheel were entrained along the wheel wall and, at a position of about 135 degrees, would fall back to the bottom of the wheel (see Figure C.5). At the same time, due to the sliding of particles along the wheel wall, particles at the bottom of the wheel were disturbing the deposited flocs and led to erosion of the finer particles in the direction opposite to the rotation. This continuing process led to full dispersion of the clay material in the wheel, making the water homogeneously turbid in the wheel, except for a layer of clay at the bottom of the wheel. The hydrodynamics in the wheel were, therefore, quite different from the ones in the jar, where most of the material was always suspended (with the exception of some heavy sand and silt particles) and experienced turbulent mixing. In contrast to jar test experiments, the shear in the wheel is very small and differential settling is expected to play a role in the experiments as the material is continuously entrained along or close to the wheel wall and falls down when gravity starts to dominate. The floc size of the flocculation experiment conducted in the wheel in comparison with the jar is shown in Figure 5.7. The median floc size in the wheel for all concentrations is higher than in the experiments with the jar. The reason for this difference can be attributed to the same reason that has been proposed to explain the residence time experiments: organic matter coming into contact with clay at very low shear will bind and lead to large flocs. Similarly to the resting time tests, this flocculation occurred very rapidly (within 2.5 minutes). After 30 minutes, the median floc size started reducing. An interesting observation was made when analysing the video at 5.0 $g L^{-1}$: flocs started to disintegrate during the settling process (see Figure C.6). This is in line with the hypothesis proposed for the resting time experiments: the rearrangement of the organic material on the clay (minimizing contact with water) causes the flocs to break up.

Residence time at the bottom of a jar experiments with samples of the wheel were also conducted. The samples were collected from the wheel and transferred to jars. Although the concentration in the jars could not be well controlled, the jars were still labelled according to the concentrations used in the wheel experiments. The samples were stored at room temperature. The median floc size with different clay concentrations is shown in Figure 5.8. It can be observed that there is a decrease in floc size after day 1, after which the floc size increases over time. The rate of increase in floc size is decreasing with concentration. As can be seen from the floc size distributions (Figure 5.8 (A-C)), all floc sizes were reduced after the first day. Again, the hypothesis is that the rearrangement of the organic material onto the clay (minimizing its contact with water) causes the flocs to break up. As for the residence time experiments with the jar tests, the later increase in particle size is attributed to the manipulation of the jars during sampling. In contrast to jar experiments, however, size growth is observed for all concentrations, which leads us to conclude that the structure of the flocs is different in this case. Most probably, flocs are overall less reconformed than in jar test experiments, leading to a larger clay surface area onto which organic matter can aggregate.

5.4. CONCLUSIONS

Understanding the alterations in sediment plume dispersion due to human interventions, such as dredging, trenching and deep-sea mining, is key to predicting and, where possible, mitigating the associated environmental impacts. This understanding is essential for

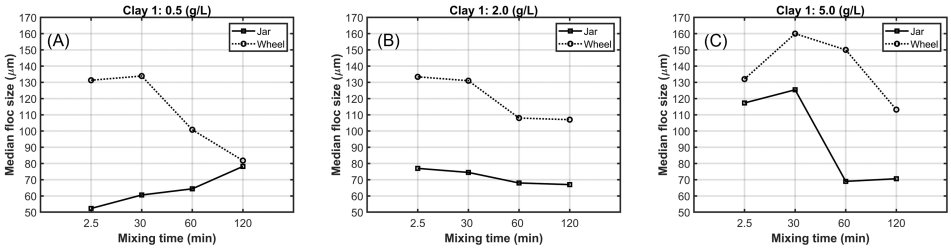


Figure 5.7: Effect of mixing time on flocculation in the jar and the wheel for different concentrations: (A) $0.5\,\mathrm{g\,L^{-1}}$, (B) $2.0\,\mathrm{g\,L^{-1}}$ and (C) $5.0\,\mathrm{g\,L^{-1}}$.

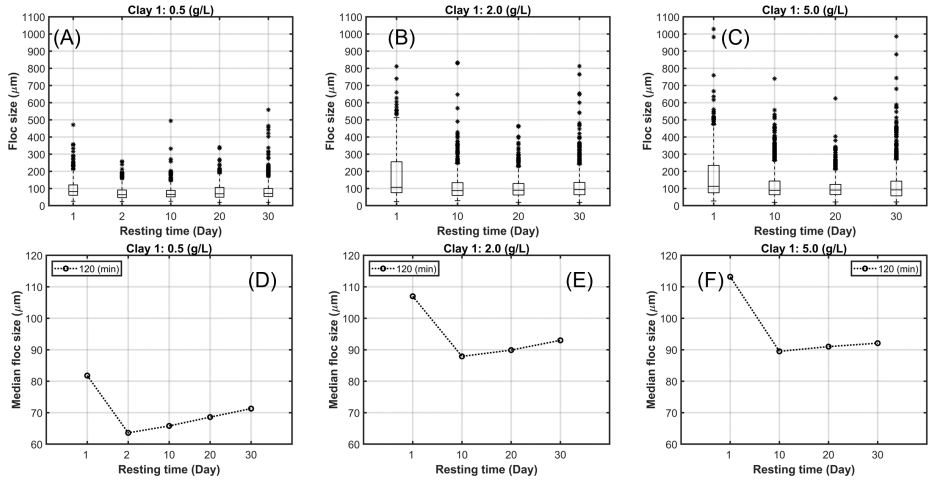


Figure 5.8: Effect of resting time on floc size at different concentrations in the wheel: (A,D) $0.5\,\mathrm{g\,L^{-1}}$, (B,E) $2.0\,\mathrm{g\,L^{-1}}$ and (C,F) $5.0\,\mathrm{g\,L^{-1}}$.

engineers to optimize equipment and processes to minimize plume dispersion. In this study, laboratory experiments were carried out to examine the flocculation of deep-sea clay collected from two different regions of CCFZ. The results showed the importance of shear, particle concentration, and organic matter in flocculation. Temperature was shown not to play a role in flocculation. Two types of mixing were studied: turbulent mixing in a jar and slow mixing in a rotating wheel, whereby differential settling plays a significant role. It was found that even at low mixing time (less than 2.5 minutes), flocculation occurs at all shear and mixing conditions, even at the lowest clay concentration used ($0.5\,\mathrm{g\,L^{-1}}$). The flocs found had a median size that is, on average, 3–6 times larger than the median floc size of the unflocculated material. The organic matter present in the sample was found to be in the form of long strains, and sweep flocculation is likely to occur. The behaviour of median floc size at steady-state upon shear in jar test experiments led us to conclude that the organic matter present in the samples has a low affinity for both water and clay. Because of the peculiar affinity the organic matter has with water and clay, the median floc size displays the following trends:

- With flocs having experienced turbulent mixing, a shear threshold (around $125\,\mathrm{s^{-1}}$) is required for the organic matter to uncoil and successfully bind to the clay with increased collision frequencies (i.e. with increasing shear rate), the median floc size is getting larger; longer mixing times result in an increase in floc size below $125\,\mathrm{s^{-1}}$ when the median floc size is well below the Kolmogorov microscale, which reduces the break-up of flocs since flocs are then simply advected by the flow. At shear rates above $125\,\mathrm{s^{-1}}$, the median floc size decreases with mixing time due to the breaking/reconformation of flocs.
- With flocs having experienced low mixing in the wheel, differential settling promotes flocculation, and the flocs are found to be two or three times larger than the ones formed in turbulent mixing in the jar tests. At long mixing times, floc sizes decrease, most probably due to the rearrangement of organic matter onto clay, which leads to the floc break-up.

Experiments were also performed to study the influence of the floc residence time at the bottom of the jars on their size. It was found that:

- With flocs having experienced turbulent mixing, flocs that were originally not touching one another in the jar would flocculate when put into contact by the gentle handling of the jar. Flocs that were already in contact with one another would see their median floc size decrease. This was attributed to a slow diffusion process that would lead to a rearrangement of organic matter onto the clay to maximize the contact area between organic matter and clay, leading to the breakage of flocs.
- With flocs having experienced low mixing in the wheel, flocs would, in all cases, first break and have a smaller size on day 2 compared to day 1. This was again attributed to the rearrangement of organic matter onto the clay to maximize the contact area between organic matter and clay, leading to a breakage of flocs. After day 2, the median flocs size increased, which was, as for the jar test experiments, linked to the handling of the jars for sampling, as floc-floc interaction is then promoted. The flocs formed by differential settling of the wheel are expected to be of a more

open structure than those formed by turbulent mixing, which is why they would aggregate upon touching (whereas flocs formed in turbulent mixing would not).

These findings highlight the complexity of flocculation kinetics for natural sediments. Most flocculation studies focus on the interaction between solid particles and synthetic flocculants (like polyacrylamides) used in sanitary engineering or mining engineering. Natural flocculants, on the other hand, are quite diverse. Some of these flocculants, known as Extracellular Polymeric Substances (EPS), consist mostly of polysaccharides that are expected to perform like polyacrylamides - in the sense that they are hydrophilic and known to bind to mineral clay easily through specific surface groups, hydrogen bonds or cation bridging. However, other natural substances are surfactants (having a hydrophilic "head" and a hydrophobic "tails"). The results found in this chapter are in line with the hypothesis that the organic matter in the samples is a surfactant, like, for instance, a phospholipid (commonly found in deep-sea areas). An analysis of the organic matter contained in the samples would be required to confirm this hypothesis.

In conclusion, the results found in the present chapter confirm that flocculation plays a significant role in deep-sea areas. Due to the short time scales involved and the (at first surprising) result that flocculation increases with shear, it is expected that flocculation also plays a significant role in plumes generated by mining activities.

6

TOWARDS IMPLEMENTATION OF FLOCCULATION IN NUMERICAL MODELING

This chapter delves into the modelling of flocculation. Models, that can be parameterized using studies like the ones presented in the previous chapters, should be suitable for incorporation into sediment transport modeling, and, above all, rightly capture the kinetics of flocculation. In this chapter, two flocculation models are compared: the LG model, based on logistic growth theory, and the S model, derived from Smoluchowski's theory. Both models can easily be integrated into large-scale sediment transport numerical models. However, they exhibit differing kinetics, as demonstrated using a series of laboratory experiments whereby mineral clay is flocculated by polyelectrolyte. Experiments are carried out at various clay concentrations and shear rates. It was found that the LG model effectively replicates the experimental time-dependent behaviour of floc sizes, while the S model does not. The LG model can be used for the whole large range of clay concentration and shear conditions investigated in the experiments. As an example, a simple relation, function of shear rate and concentration, is given (see 6.53) for the clay and flocculant studied in this chapter. This equation could easily be implemented in a sediment transport model, making the spreading of dredging plumes a function of particle interactions.

Parts of this chapter have been published in Continental Shelf Research (2022) Ali and Chassagne, 2022.

6.1. INTRODUCTION

HYDRODYNAMIC models are used in sediment transport models to calculate the advection and diffusion of suspended particles in the water column. For most applications, the sediment typically is decomposed into two or three fractions with associated settling velocities in the 0.1 to 1 mm s^{-1} range. For a large number of applications, this decomposition makes it possible to correctly predict the Suspended Particulate Matter (SPM) concentration in space and time (Lesser et al., 2004; Manning et al., 2006; Manning and Dyer, 2002; Normant, 2000). Other methods are to calculate a representative overall settling velocity at a point based on environmental parameters (Soulsby et al., 2013). Indeed, changes in particle properties by flocculation and exposure to shear result in a change in settling velocity over time for a given sediment fraction. These changes are currently poorly accounted for in sediment transport models, resulting in inaccurate predictions in coastal regions where these changes occur. Several studies have thus focused on incorporating flocculation into sediment transport models (Fettweis, 2008; Manning et al., 2017; Many et al., 2016; Russel et al., 1989). These models, however, are not physically meaningful because they contain adjustable parameters that are fitted to the data and, more importantly, they do not account for specific physical processes such as organic matter-induced flocculation or particle coiling under shear (Chassagne and Safar, 2020). Previously the models used to describe flocculation in detail have been based on the Population Balance Equation (PBE), in which flocculation is represented by the aggregation and break-up of similar colloidal particles, as in salt-induced flocculation.

Numerous numerical investigations have been carried out on the subject of DSM. Grunsven et al., 2018 presented comprehensive numerical and experimental findings related to plume discharge from a VTS. Decrop and Wachter, 2019 performed a Computational Fluid Dynamics (CFD) analysis to investigate the effects of different discharge conditions for a horizontal discharge from a PNMT. Ouillon et al., 2021 recently employed DNS simulations to study the discharge process of a moving PNMT using the Boussinesq approach. Elerian, 2023 introduced a novel numerical model for predicting turbidity flow behind a PNMT. Their model combines the drift-flux modelling approach with the PBE model. As stated above, the PBE cannot properly account for the role of organic matter, which is a key parameter in deep-sea flocculation, as demonstrated in Chapter 5. For instance, a particle can only change from its size class by breaking or aggregating and not by coiling (keeping its mass but reducing its volume). In a recent article (Chassagne, 2021), it was shown that the analytical model based on logistic growth theory (LG model) presented by Chassagne et al. in (Chassagne and Safar, 2020) could be used to predict the flocculation of suspended mineral clay (kaolinite). The suspensions were destabilized by the addition of salt. In particular, it was demonstrated that the LG model (1) reproduces the classical results found for the salt-induced flocculation kinetics at the onset of the experiments, and (2) enables to study of the flocculation kinetics over the whole duration of the experiment. This last point implies that, by fitting the experimental data over the whole duration of the experiment, it was shown that the measured floc size $L(t)$ time evolution follows the relation $dL/dt = L/t_b - L^2/(L_{eq}\, t_b)$ predicted by the model, where t_b is a characteristic time and L_{eq} a characteristic size, which are obtained from the fits. The advantage of the LG model is that it enables to parameterize the floc size evolution

in time as a function of measurable parameters, such as shear rate, suspended solid concentration and salt, but importantly, also as a function of organic matter properties (concentration, charge, molecular weight...) as shown in Deng et al., 2022 and Safar et al., 2023.

Analytical models like the one presented in (Chassagne, 2021; Chassagne and Safar, 2020) are required in many applications, where estimations of the characteristic timescales of flocculation and the equilibrium floc size of flocs should be done in a fast way. For example, large-scale sediment transport models require flocculation models that can be run on multiple grid cells at the same time. This prevents models like Population Balance Equations (PBE) models from being used for a system of more than 3 equations (Shen et al., 2018). The simplest PBE model that can be thought of is a PBE with a single equation. This equation then represents the time evolution of a single class of particles, usually taken to be the D_{50} class (the class that represents the particles of size L whereby 50 percent of all particles have a size smaller than L). Such an equation can obviously not be used for modelling the sediment mass transfer between classes. A minimum of two classes is required for that purpose (Chassagne and Safar, 2020; Shen et al., 2018). A single PBE equation can nonetheless be used under the assumption that all mineral sediment is contained in flocs and that all flocs have the same size $L(t)$ with L varying in time under the influence of environmental conditions (shear stress in particular). Such a single PBE equation is given by Winterwerp in (Winterwerp, 1998). In-situ studies have demonstrated that floc sizes are indeed dynamic and shear-dependent (Manning et al., 2007; Soulsby et al., 2013; Van Leussen, 1988; Verney et al., 2011). The way to connect the floc size and its Stokes settling velocity - which is the key parameter for large-scale sediment transport models - will not be discussed in the present chapter but is the topic of numerous publications (Dyer and Manning, 1999; Gratiot and Manning, 2004; Khelifa and Hill, 2006; Maggi, 2013; Manning et al., 2007; Mehta, 2013; Spearman et al., 2011; Spencer et al., 2011).

The present chapter aims to compare the model introduced by Chassagne and Safar, 2020 with the one presented by Winterwerp, 1998. In particular, the validity and parametrization of the models will be discussed. A series of laboratory experiments are presented to test the theories, where the flocculation of a mineral clay by polyelectrolyte is studied. This type of flocculation is representative of the flocculation occurring in situ, whereby mineral clay is found to be bound in different amounts to organic matter, usually in the form of complex mixtures of biopolymers (consisting of polysaccharides, proteins, nucleic acids, lipids and humic substances) (Deng et al., 2019; Safar et al., 2019). The experimental setup allows studying the dependence of flocculation on clay concentration and shear rate, two important parameters that are found in the model presented by Winterwerp.

In Section 6.2, both models are presented, and their differences are discussed. In Section 6.3, the material used is presented. The results are presented and discussed in Section 6.4, and the conclusions are given in the Section 6.5.

6.2. THEORY

In this section, the two theoretical models that we aim to compare are recalled. In the first subsection, the model derived by Chassagne and Safar, 2020 is recalled. This model is based on logistic growth theory and hence will be termed "LG model". In the second subsection, the model presented by Winterwerp, 1998 is discussed. This model originates from the work of Smoluchowski and, therefore, will be termed "S model". The differences between the two models are discussed in the third subsection.

6.2.1. LOGISTIC GROWTH MODEL (LG MODEL)

The logistic growth (LG) model is an empirical model that is found to be very convenient to model the time evolution of colloidal suspensions undergoing flocculation. We refer to Chassagne, 2021; Chassagne and Safar, 2020 for further details and examples of application. The change of floc size as a function of time is described by the equation:

$$\frac{dL}{dt} = [b(t) - d(t)]\, L \tag{6.1}$$

whereby the (positive) functions for birth $b(t)$ and decay $d(t)$ are given by:

$$b(t) = \frac{a_b}{t_b} \frac{exp(-t/t_b)}{1 + a_b exp(-t/t_b)} \tag{6.2}$$

$$d(t) = \frac{a_d}{t_d} \frac{exp(-t/t_d)}{1 + a_d exp(-t/t_d)} \tag{6.3}$$

The coefficients a_b, t_b, a_d, t_d are to be parameterized. As stated in Chassagne, 2020, it is emphasized that the names "birth" and "decay" are solely chosen because they appear with a plus and minus sign in the balance equation eq.(6.1). One can easily show that considering only the birth function ($d(t) = 0$) gives as solution a sigmoid function, with a growth that will be limited in time. In other words, at infinite time $dL/dt = 0$ implying that $L(t \to \infty) = L_{eq}$ (even when no decay term is present) where L_{eq} is a value that will depend on parameters such as floc composition, shear rate, salinity, etc. For example, let us consider a flocculation experiment whereby external parameters are fixed (constant shear, given salinity and pH, no addition of organic matter over time), as is the case for flocculation experiments that can be realized in the lab. At $t = 0$ some amount of clay and organic matter are mixed in a jar, at a given shear. By following the evolution of the floc size over time, one will find that the mean floc size indeed follows a sigmoid behaviour, as eventually, the flocs will reach an equilibrium size that is strongly dependent on the amount of organic matter present in the jar and the imposed shear rate (Deng et al., 2019; Safar et al., 2019; Shakeel et al., 2020). The growth of flocs is therefore limited by depletion of free organic matter in the water (unbonded flocculant) and/or because their size is reaching the Kolmogorov microscale, but *not* because there is a steady-state between aggregation and break-up. A steady state would imply that there would be continuous aggregation and break-up of matter at the surface of a floc. This would be the analogue of the adsorption/desorption of molecules from a surface as is studied in thermodynamics (illustrated, for example, by a Langmuir isotherm (Langmuir, 1918). This is a crucial difference between this model and the Smoluchowski model presented in the

next section. By introducing a decay term $d(t)$, as we will show in fig. 6.8, we will be able to model what happens at longer experimental times, after the initial growth (birth) has occurred. It is indeed usually observed that at these longer timescales, a reduction in size is observed. This reduction in size can be due to two effects (not mutually exclusive): (a) an erosion of the flocs under shear and (b) a coiling of particles under shear. Phenomenon (b), in particular, has been observed, both in-situ and in the lab (Safar et al., 2019; Shakeel et al., 2020). This phenomenon leads to flocs of higher density and smaller size. In fig. 6.8, a decrease of about 20% in size is such obtained. If only particle sizes are studied, this significant reduction in floc size could be mistaken for the breaking of flocs over time, but microscopic observation of the flocs over time have confirmed this densification (Shakeel et al., 2020). The analytical solution of eq. (6.1) is given by:

$$L(t) = L_{eq}\frac{1 + a_d exp(-t/t_d)}{1 + a_b exp(-t/t_b)} \tag{6.4}$$

where $L_{eq} = L(t \to \infty)$. The size L_{eq} can be seen as the size that the floc would reach provided that all parameters (concentration, shear stress, salinity...) remain constant over time. Note that the change in number of flocs per unit volume as a function of time can be modelled with an equation similar to eq. (6.4) where a_d, a_b, t_d, t_b are (different) adjustable parameters Chassagne, 2020:

$$n(t) = n_{\infty}\frac{1 + a_d exp(-t/t_d)}{1 + a_b exp(-t/t_b)} \tag{6.5}$$

where $n_{\infty} = n(t \to \infty)$. At times such that $t \to 0$ implying that $t << t_b, t_d$ eq. (6.4) reduces to:

$$L(t \to 0) = L(t = 0) + \left(\frac{dL}{dt}\right)_{t=0} t \tag{6.6}$$

where the flocculation rate $\left(\frac{dL}{dt}\right)_{t=0}$ and size at origin $L(t = 0)$ are defined by:

$$\left(\frac{dL}{dt}\right)_{t=0} = (k_b - k_d)\, L(t = 0) \tag{6.7}$$

$$L(t = 0) = \frac{1 + a_d}{1 + a_b} L_{eq} \tag{6.8}$$

When $L(t = 0) < L_{eq}$ it follows that $a_d < a_b$ and vice versa. The growth and decay rates k_b and k_d as given by:

$$k_b = \frac{a_b/t_b}{(1 + a_b)} \tag{6.9}$$

$$k_d = \frac{a_d/t_d}{(1 + a_d)} \tag{6.10}$$

6.2.2. SMOLUCHOWSKI MODEL (S MODEL)

Smoluchowski introduced in 1917 the Population Balance Equations (PBE), which give the time evolution of classes of colloidal particles (flocs), a class i being defined as a collection of particles with concentration n_i, all particles in class i having the same size

(diameter) L_i. The concentrations n_i can either be given in number, mass or volume of particles per unit of volume (Chassagne, 2020; Elimelech et al., 1995). Many studies have since then proposed aggregation and break-up parameters to be implemented in PBEs (Barthelmes et al., 2003; Elimelech et al., 1995; Flesch et al., 1999; Kusters, 1991; Russel et al., 1989; Spicer and Pratsinis, 1996).

The simplest PBE model that can be proposed is the one equation PBE which we call the "S model". This equation represents the time evolution of a single class defined by a concentration $n(t)$ and an average particle size $L(t)$. Unlike the LG model, the S model contains parameters related to the aggregation and break-up properties of the particles. These parameters are, in particular, functions of concentration and shear.

In order to set up an equation for the average particle size $L(t)$ as a function of time, first, the link between $L(t)$ and the total number of particles (flocs) per unit of volume $n(t)$ and the number of primary particles within a floc $N(t)$ should be made. This is done in the first subsection, where we follow the approach used by Winterwerp (Winterwerp, 1998), who assumes that flocs are fractal objects. The Smoluchowski equation, which expresses the time evolution of $n(t)$, will then be converted into an equation for the time evolution of $L(t)$. This is done in the second subsection.

LINK BETWEEN L, n AND N

We define $n(t) = \sum N_i(t)$ as the total number of particles (flocs) per unit of volume at time t and $N_i(t)$ as the number of primary particles inside a floc of size $L_i(t)$. Primary particles are defined as the smallest size of particles in the system. These particles have a size L_p and it is assumed that primary particles cannot break. By aggregation of primary particles, flocs can be formed. By break-up of flocs, smaller flocs are produced and the particles having the smallest size that can be produced are primary particles.

If one defines $n_0 = n(t = 0)$ to be the number of unflocculated primary mineral sediment particles per unit of volume in a closed volume (as, for example, in a jar test experiment), it follows that n_0 is a constant as a function of time, whereas the size L_i of particles in suspension will be time-dependent as flocs are growing (or breaking). The total number of primary particles per unit of volume is given by:

$$n_0 = \sum_i N_i n_i \tag{6.11}$$

Note that $N_1 = 1$ with $L_1 = L_p$ and that at $t = 0$, $n_0 = n_1$. If it is assumed that, at any moment in time, a suspension is well represented by a characteristic size and concentration, one may write:

$$\begin{aligned} n_0 &= n(t)N(t) \\ 0 &= \frac{dn}{dt}N + n\frac{dN}{dt} \end{aligned} \tag{6.12}$$

We have here made the assumption that only one class i is present at each time and hence $n(t) = n_{i(t)}(t)$, where the number $i(t)$ of the class is changing at each time step. From eq. (6.12), it follows that, when i increases $L = L_i$ and $N = N_i$ increase and hence $n = n_i$

decreases. One may deduce that the rate of decrease of n is given by:

$$\frac{dn}{dt} = \frac{-1}{n_0}\frac{dN}{dt}n^2 \tag{6.13}$$

The relation between the number of primary particles in a floc and floc size is given by Kranenburg, 1994:

$$N(t) = \left(\frac{L(t)}{L_p}\right)^D \tag{6.14}$$

where D is usually termed "fractal dimension", in reference to the study of the flocculation of monodisperse primary particles, where the concept of self-similarity can be used. Experiments have been conducted to assess the fractal dimension for diffusion-limited, and reaction-limited aggregates (Russel et al., 1989), where the initial growth of flocs is also investigated. Combining eqs. (6.12) and (6.14) gives:

$$\frac{1}{n}\frac{dn}{dt} = -\frac{1}{N}\frac{dN}{dt} = -\frac{D}{L}\frac{dL}{dt} \tag{6.15}$$

The volume fraction of primary particles (pp) inside a floc can be evaluated using:

$$\phi_{pp\,in\,floc} = \frac{V_{pp\,in\,a\,floc}}{V} = \frac{N \times V_p}{V} = N\left(\frac{L_p}{L}\right)^3 = \left(\frac{L_p}{L}\right)^{3-D} \tag{6.16}$$

where $V_{pp\,in\,a\,floc}$ is the volume occupied by primary particles inside a floc, V_p is the volume of a primary particle and $V \simeq L^3$ the volume of a floc. We have here implicitly assumed that Class 1 and Class $i(t)$ particles have the same shape. If this is not the case, a corresponding multiplying constant should be inserted in the bracket term. The volume fraction $\phi_{pp\,in\,floc}$ is a measurable quantity, as it can be linked to the floc density ρ_{floc} (to be estimated from the settling velocity of floc, applying Stokes'law) by realizing that:

$$\phi_{pp\,in\,floc} = \frac{\rho_{floc} - \rho_w}{\rho_s - \rho_w} \tag{6.17}$$

where ρ_w is the absolute density of the suspending medium (water), assuming that all the primary particles are contained in flocs (no primary particles are left unflocculated), one gets:

$$\phi_{pp\,in\,floc} = \frac{n \times V_{pp\,in\,floc}}{n \times V} = \frac{\phi_s}{nV} \tag{6.18}$$

where $\phi_s = c/\rho_s = n_0 L_p^3$ is the volume fraction of primary particles in suspension, ρ_s is the absolute density of a primary particle and c the mass concentration (kg/m^3) of primary particles in suspension. Combining eqs. (6.16) and (6.18):

$$\frac{dn}{dt} = -D\frac{c}{\rho_s}\frac{L^{-D}}{L_p^{3-D}}\frac{1}{D}\frac{dL}{dt} \tag{6.19}$$

By comparing with eq. (6.15), one finds the relation between number n of particles in suspension, number N of primary particles in a floc, size L of flocs and concentration of primary particles:

$$n = \frac{c}{\rho_s}\frac{L^{-D}}{L_p^{3-D}} = \frac{c}{NL_p^3\rho_s} \tag{6.20}$$

TIME EVOLUTION OF THE MEAN FLOC SIZE L

One obtains, from the analysis originally performed by Smoluchowski (Chassagne, 2020; Elimelech et al., 1995; Russel et al., 1989) that the rate of change of the number of particles in suspension is given by:

$$\frac{dn}{dt} = -\frac{1}{2}\alpha\beta n^2 \tag{6.21}$$

In eq. (6.21), the collision efficiency α and collision frequency β are class-independent, which is the underlying assumption made by Smoluchowski. The factor 1/2 that appears in eq. (6.21) originates from the fact that each binary collision leads to the loss of two particles of class $i(t)$ and the creation of one particle of class $i(t+dt)$. The dependence of the flocculation rate on shear is usually expressed through the dependence of the collision frequency on shear in the case of orthokinetic flocculation. This dependence can be expressed as (Chassagne, 2020; Elimelech et al., 1995):

$$\beta \simeq 4GL^3 \tag{6.22}$$

in the case that all particles at time t have the same size $L(t)$ as is assumed in this subsection. The collision efficiency α is usually assumed to be independent of shear.

Combining eqs. (6.15), (6.20) and (6.21) one gets:

$$\frac{dL}{dt} = \frac{2\alpha G}{D}\frac{c}{\rho_s}\frac{L^{4-D}}{L_p^{3-D}} = k_A c G L^{4-D} \tag{6.23}$$

which corresponds to eqs.(14,15) proposed by Winterwerp, 1998 but for a different prefactor as is detailed in the Appendix. One notes that k_A is a function of the fractal dimension D and primary particle size L_p and that k_A does a-priori not depend on shear or concentration. This formulation for dL/dt, based on the Smoluchowski approximation, does not account for a limit in growth which implies that L is bound to increase in time to reach unrealistic values. For this reason, breakup functions are introduced to limit the growth (Chassagne, 2020). The approach used by Winterwerp is to use a function that is scaling as:

$$\frac{dn}{dt} = -s \times n \tag{6.24}$$

where s is the break-up rate. Winterwerp expresses the change in particle concentration due to breakage as:

$$\frac{dn}{dt} = e_b \times s \times n \tag{6.25}$$

where e_b is an "efficiency parameter" which is superfluous as it can implicitly be included in s. Note the minus sign difference between eqs. (6.24) and (6.25). The break-up function in the PBE equation appears both with a + and − sign: written like in eq. (6.24) it expresses the reduction in the number of flocs when flocs are leaving the size class by breaking, whereas written like eq. (6.25) it expresses the increase in the number of flocs in a size class due to the breakage of flocs of larger size. In order to limit the size of flocs, eq. (6.25) should be used, as increasing n implies decreasing L. A simple expression for s is of the form (Barthelmes et al., 2003; Spicer and Pratsinis, 1996):

$$s = s_b\left(\frac{\eta G}{\tau^*}\right)^q L^p \tag{6.26}$$

where s_b, q and p are parameters to be fitted, η is the viscosity of the suspension, and τ^* is characteristic shear stress which is a measure for the aggregate strength: the larger τ^*, the less the particles are susceptible for breakage. An expression for τ^* is given by eq.(64). The product ηG is the shear stress in shear flows: the higher the stress, the more flocs are susceptible to break.

Combining eqs. (6.15), (6.20) and (6.26) one gets:

$$\frac{dL}{dt} = \frac{-s_b}{D}\left(\frac{\eta G}{\tau^*}\right)^q L^{p+1} = -k_B G^q L^{p+1} \tag{6.27}$$

which is to be compared with eq.(23) of Winterwerp, 1998:

$$\frac{dL}{dt} = -k_B G^q (L - L_p)^{(p+1)-(2q-1)} L^{(2q-1)} \tag{6.28}$$

The derivation of this expression is given in the Appendix. One notes that k_B is a function of the fractal dimension D, primary particle size L_p, viscosity η and rupture force F and that k_B is a-priori not dependent on concentration c or shear stress G. Combining eqs. (6.23) and (6.27) gives:

$$\frac{dL}{dt} = k_A c G L^{4-D} - k_B G^q L^{p+1} \tag{6.29}$$

The full flocculation model proposed by Winterwerp is given as eq.(26) in Winterwerp, 1998, where aggregation and breakage terms are combined. Winterwerp uses $p = 2$, $q = 1.5$ and $D = 2$ which leads to:

$$\frac{dL}{dt} = \left[k_A c G - k_B G^{3/2}(L - L_p)\right] L^2 \tag{6.30}$$

The reason that Winterwerp introduces the term $(L - L_p)$ in eq. (6.28) as opposed to L in eq. (6.27) arises from the fact that at steady-state (when $dL/dt = 0$), eq. (6.30) then enables to write, see eq.(27) in Winterwerp, 1998:

$$L_{eq} = L_p + \frac{k_A}{k_B} c G^{-1/2} \tag{6.31}$$

The underlying assumption is that particles can never become smaller than the primary particles, which are assumed insensitive to shear. Equation (6.29) leads to:

$$L_{eq}^{D+p-3} = \frac{c k_A}{k_B} G^{1-q} \tag{6.32}$$

Equation (6.31) implies that eq. (6.30) can be written as a function of L_{eq} which gives:

$$\frac{dL}{dt} = k_B G^{3/2}\left(L_{eq} - L\right) L^2 \tag{6.33}$$

One can note that this equation, for a constant shear, can only describe the growth of the mean particle size with time for $L \leq L_{eq}$ since the term at the right-hand side of the equal sign is then positive or zero.

6.2.3. COMPARISON BETWEEN MODELS

In the S model, both aggregation and breakup terms are required to limit floc growth. When no breakup term is present, the aggregation term will ensure that growth is unconstrained, leading to non-physical results. In the LG model, both birth and decay functions are constrained: even with only a birth function $b(t)$ a finite equilibrium size L_{eq} is reached. In flocculation experiments, a suspension of aggregating particles can reach an equilibrium size for different reasons. Growth can be prevented for particles above a characteristic size (related in general to the Kolmogorov microscale) because high shear stresses make it impossible for particles to aggregate. However, growth can also be limited because of a depletion of flocculating agents. This happens when polymeric flocculant is underdosed (Shakeel et al., 2020) even when the shear stresses would allow further growth. In the S model, this would imply that k_B is dependent on flocculant dosage. For the LG model, the evolution of the mean particle size for aggregating particles is described by setting $a_d = 0$ (i.e. $k_d = 0$) in eq. (6.4) which then reduces to

$$L(t) = L_{eq} \frac{1}{1 + a_b \exp(-t/t_b)} \tag{6.34}$$

with

$$\frac{dL}{dt} = \left(\frac{1}{L} - \frac{1}{L_{eq}}\right) \frac{1}{t_b} L^2 \tag{6.35}$$

As was discussed earlier in this chapter, considering only the birth function $b(t)$ only means that the particle size L is an *increasing* function in time. Introducing a decay function $d(t)$ would imply that the size L goes through a maximum as a function of time. Clearly, from considering eq.(6.33) the S model does not allow for L to go through a maximum (provided that k_B and G are constant - which we assume here), therefore, in order to compare both models, eq.(6.35) is to be compared with eq.(6.33). Both equations describe the growth of the mean particle size over time but not with the same kinetics. It was shown in Chassagne, 2021 that eq. (6.35) can be used to follow the time evolution of particle sizes for kaolinite suspensions destabilized by the addition of salt. This meant that by plotting the experimental data according to the function $(dL/dt)/L$ a linear dependence on L was found. The LG model indeed predicts a linear dependence, as is found by rewriting eq. (6.35) as:

$$\frac{1}{L}\frac{dL}{dt} = \frac{1}{t_b}\left(1 - \frac{L}{L_{eq}}\right) \tag{6.36}$$

The S model, on the other hand, predicts a quadratic dependence, see eq. (6.31):

$$\frac{1}{L}\frac{dL}{dt} = k_B G^{3/2} \left(L_{eq} - L\right) L \tag{6.37}$$

The difference between the two models is illustrated in fig. 6.1(A). The S model was plotted according to eq. (6.33) and the LG model according to eq. (6.35). The characteristic growth time, equilibrium floc size and primary particle size were taken to be $t_b = 800s$, $L_{eq} = 20\mu m$ and $L_p = 1\mu m$. We made use of the equivalence between the two models at short timescales to evaluate the other required parameters, which can be found using the

following equalities:

$$k_B G^{3/2} = \frac{k_A c G L_p}{\left(L_{eq} - L_p\right) L_p} = \frac{k_b}{\left(L_{eq} - L_p\right) L_p} = \frac{1}{t_b} \frac{1}{L_p L_{eq}} \tag{6.38}$$

Using these parameters, the LG model would give the dotted curve (LG model (b)). At small timescales, the S model and the LG model (b) overlap as expected. The curve obtained for the S model was then fitted using eq. (6.34), which leads to the dashed curve (LG model). For this fit, it was necessary to use $t_b = 97s$ and $L_p = 0.0046\mu m$. The difference between the flocculation kinetics of the two models is better illustrated in fig. 6.1(B), where $(dL/dt)/L$ is plotted for each model: the LG model predicts a linear dependence on L whereas the S model does not. For salt-induced flocculation, it was shown that the linear dependence of $(dL/dt)/L$ on L is also found for the experimental data (Chassagne, 2021). It remains to be studied whether a similar dependence can be observed for polyelectrolyte-induced flocculation.

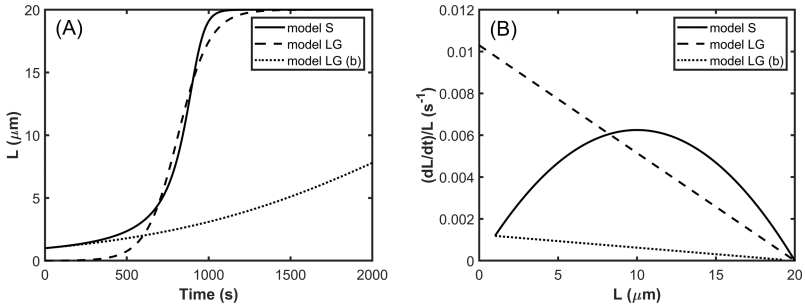


Figure 6.1: A) Comparison between the LG model and S model and (B) their flocculation kinetics. The S model is plotted according to eq.(6.33) and the LG model according to eq.(6.35). The characteristic growth time, equilibrium floc size and primary particle size are taken to be $t_b = 800$ s, $L_{eq} = 20$ μm and $L_p = 1$ μm. The curves corresponding to model LG (b) are obtained using the equivalence of the two models at short timescales, i.e. eq.(6.38). The curve obtained for the S model was fitted using eq.(6.34), which leads to the dashed curve (LG model). For this fit, it was necessary to use $t_b = 97$ s and $L_p = 0.0046$ μm.

SHORT TIMESCALES

At short times, one gets for the LG model, from eq. (6.7), and assuming that $L(t=0) \simeq L_p$:

$$\left(\frac{1}{L}\frac{dL}{dt}\right)_{t\to 0} = k_b(1 - k_b t) \tag{6.39}$$

$$\left(\frac{dL}{dt}\right)_{t=0} = k_b L(t=0) = \frac{a_b/t_b}{(1+a_b)^2} L_{eq} \tag{6.40}$$

with,

$$L(t=0) \simeq L_p = \frac{1}{1+a_b} L_{eq} \tag{6.41}$$

For the S model, eqs. (6.30) and (6.33) lead to

$$\left(\frac{dL}{dt}\right)_{t=0} = k_A c G L_p^2 = k_B G^{3/2} \left(L_{eq} - L_p\right) L_p^2 \tag{6.42}$$

It is, therefore, easy to make the equivalence between the two models:

$$k_b = \frac{a_b}{t_b}\frac{1}{1+a_b} = \frac{1}{t_b}\frac{L_p}{L_{eq}}\left(1-\frac{L_p}{L_{eq}}\right) = k_A c G L_p \tag{6.43}$$

This relation suggests that the birth rate at the onset of aggregation should be linearly dependent on shear and the concentration of primary particles. Note that as it is found in most cases that $a_b >> 1$, we also get:

$$k_b \simeq \frac{1}{t_b} \tag{6.44}$$

6.3. MATERIAL AND EXPERIMENTAL METHODS

6.3.1. CLAY

The clay used in all the experiments referred to as K-10.000, was bought from the VE-KA company (Werkendam, The Netherlands). The original lump of clay's water content was 37.5 %, and the sand content was 21 %. The clay was dispersed in tap water, and the resulting suspension had a conductivity of less than 453.1µs cm^{-1} (Shakeel et al., 2020). A Malvern Mastersizer 2000, a technique based on static light scattering (SLS), was used to determine the Particle Size Distribution (PSD) of the clay Figure 2.4. This clay was chosen because of its fairly monodispersity: the original clay suspension was found to have a mean diameter (d_{50}) of 5.6 µm. The clay is composed of a majority of non-swelling components (Shakeel et al., 2020).

6.3.2. FLOCCULANT

In order to study the effect of clay concentration on the flocculation rate, different clay concentrations were used in combination with the anionic flocculant Zetag 4110 (BASF). The flocculant to clay concentration ratio was kept the same for all experiments and equal to 2.5 mg/g, which is close to the optimal concentration for flocculation (Shakeel et al., 2020). Zetag 4110 has a medium anionic charge with high molecular weight. The flocculation experiments were performed in a jar (Figure 2.2).

6.4. RESULTS AND DISCUSSION

6.4.1. FLOCCULATION KINETICS

In this subsection, the particle size time evolution is given in Figure 6.2 (top panel) for three examples. It can be noted that the c = 0.2 gL^{-1} sample displays multimodal particle size distributions, which makes the analysis in terms of mean particle size (D_{50}) difficult. The data for 0.2 gL^{-1} was therefore not further considered in this study. The data was subsequently plotted in a different way to test eqs. (6.36), (6.37) and (6.39). The result is given in Figure 6.3, where L symbolizes $D_{50}(t)$. From the trends, it appears that at the onset of flocculation, the data plotted as $(dL/dt)/L$ indeed follows the linear dependence predicted by eqs. (6.36) and (6.39). This implies that the flocculation kinetics follow the dependence predicted by the LG model, which is in line with the trends found for salt-induced flocculation discussed in Chassagne, 2021. This dependence cannot be obtained from the S model. The graph indicates that the observed dependence is not predicted

by the S model and is closer to that of the LG model. If the S model is reduced to its aggregation part (the term involving k_A in eq. (6.30)), it would still not reproduce the observed behaviour as the S model predicts an increase of $(dL/dt)/L$ as a function of L, not a decrease as observed. A constant increase in $(dL/dt)/L$ would imply an exponential growth of L with time. Such exponential growth is not observed experimentally.

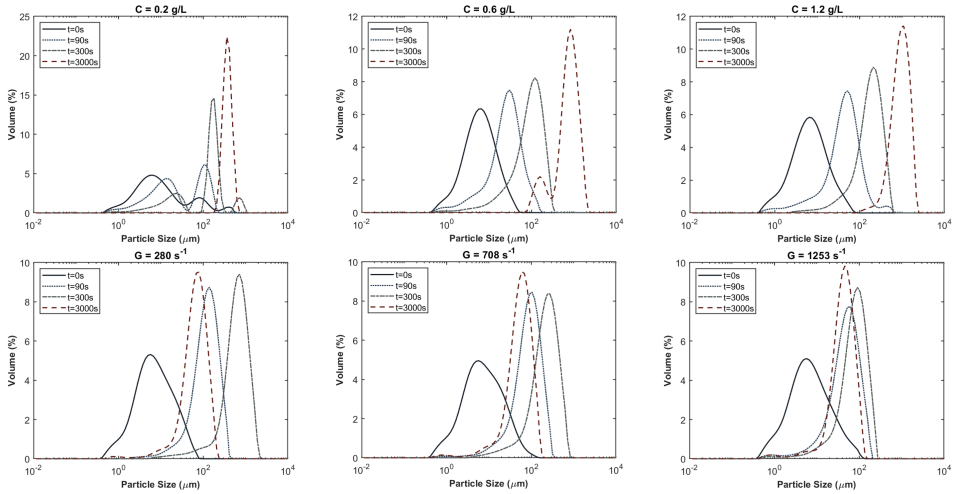


Figure 6.2: (Top panel): Particle size distributions for different clay concentrations (2.5 $mg\,g^{-1}$ flocculant (Zetag 4110) to clay ratio). A constant shear rate of 112 s^{-1} is applied. (Bottom panel): Particle size distributions for different shears (2.5 $mg\,g^{-1}$ flocculant (Zetag 4110) to clay ratio, 1.2 $g\,L^{-1}$ clay.

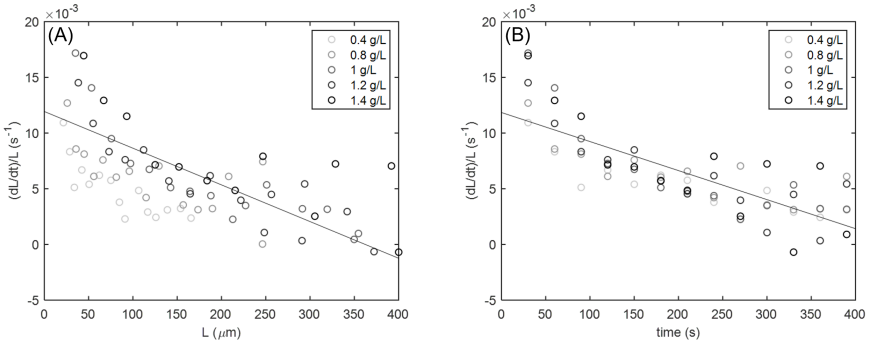


Figure 6.3: (dL/dt)/L as a function of L (A) and time (B), for suspensions having 2.5 $mg\,g^{-1}$ flocculant (Zetag 4110) to clay ratio. A constant shear rate of 112 s^{-1} is applied. The curves represent fits for 1.2 $g\,L^{-1}$.

In order to study the flocculation dynamics as a function of time, the data for c = 1.2 $g\,L^{-1}$ was fitted for different time intervals Δt. These time intervals are defined as $\Delta t = [0\ t_{fit}]$, where t_{fit} can be varied. An illustration is given in Figure 6.4. The LG model is used for fitting. The model results for several time intervals Δt are shown in Figure 6.4 (right). The

relation between L_{eq} and $k_b \simeq 1/t_b$ is represented in Figure 6.4 (left). It is found that both L_{eq} and t_b are increasing linear functions of Δt until $\Delta t = 1000$ s, and

$$\begin{aligned} L_{eq}(\mu m) &= 1.54 t_b^{1.15} \\ t_b &= 0.2\Delta t \end{aligned} \tag{6.45}$$

It was also found that the parameter a_b could be set constant, as it barely varied with the time interval durations. It was set to its average value of 16.6.

The reason that L_{eq} and k_b are functions of the time interval Δt is due to the change in flocculation kinetics. At the start of flocculation, when clay and polyelectrolyte are mixed, the clay particles will extremely rapidly bind to the bare polyelectrolyte strands. For the smallest time intervals giving meaningful results ($\Delta t = 90$ s), it is found that $L(0) = 7.8\ \mu m$, which is in agreement with the clay primary particle size. For longer fitting time intervals, $L(0)$ becomes a function of Δt for $t \lesssim 1500$ s as $L(0)$ and L_{eq} are linked by eq.(6.41). It is then found that $L(0)$ is increasing linearly with Δt. During the period $t \lesssim 1500$ s, two types of flocculation occur : (a) the remaining mineral clay particles in suspension (if any) are captured by the existing flocs, and (b) floc-floc aggregation occurs, leading to a change in flocculation kinetics. This is reflected in a change in L_{eq} and k_b but especially in growth in $L(0)$ as the "primary" particle is not a mineral clay particle anymore but a floc. For time intervals such that $\Delta t > 1500$ s, $L(t)$ is not a function of Δt anymore as $L(t > 1500\text{ s})$ has reached a constant value. In that case, it is found that the average value of $L(0)$ is about 60 μm, which can be considered a good estimate for the primary floc size over the whole experimental range.

From this study and the results illustrated in Figure 6.4(A), it can be concluded that the same fitting parameters can't be used for the (fast) flocculation of unbonded mineral clay and polyelectrolyte strands or for the flocculation of already formed flocs. This is why it was proposed in Chassagne, 2021 to separate SPM into two classes: one class (Class 1) being defined as unflocculated clay mineral particles and one class (Class 2) that is composed of flocs (mineral clay bound to organic matter). The mass transfer from Class 1 to Class 2 then obeys the fast kinetics observed here at small Δt, whereas the flocculation occurring in Class 2 (the aggregation of flocs lead to a new floc, that, by definition, belongs to Class 2) can be modelled, in good approximation, using the parameters found from fitting the data until an equilibrium size is reached ($\Delta t > 1500$ s).

In the following two sections, where the dependence on clay concentration and shear will be investigated, and two-time intervals will be studied: $\Delta t = 400$ s and $\Delta t = \Delta t_{end}$, whereby Δt_{end} represents the time interval between the start and the end of the experiment. In all cases, the mean particle size $L(t)$ has reached a constant value when the time corresponding to the end of the experiment is reached.

6.4.2. DEPENDENCE ON CLAY CONCENTRATION

The dependence of $L(t)$ on clay concentration was studied for concentrations between 0.4 and 1.6 g L^{-1} which is within the concentration range for which the measurements are not limited by light detection issues. A constant shear rate of 112 s^{-1} is used in all experiments. The time evolution of the mean particle size is given in Figure 6.5. Every

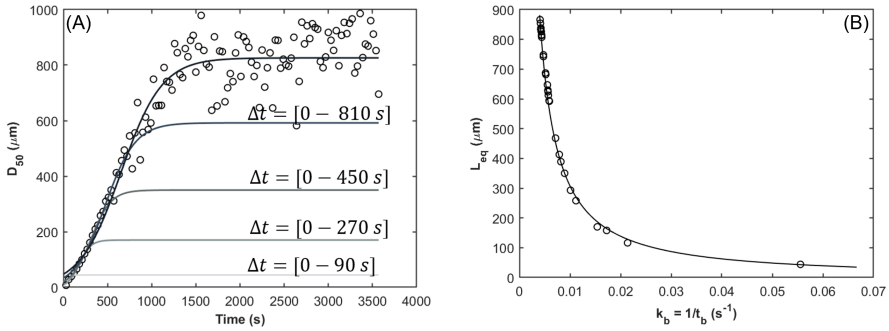


Figure 6.4: (Figure A): Particle size evolution as a function of time for a suspension consisting of 1.2 gL^{-1} clay and 2.5 mgg^{-1} flocculant (Zetag 4110) to clay ratio. A constant shear rate of 112 s^{-1} is applied. The curves represent fits for given time intervals as indicated next to each curve. The curve without indication represents the fit for the whole duration of the experiment. (Figure B): L_{eq} as a function of k_b found from fitting the particle size evolution as a function of time for different time intervals Δt

.

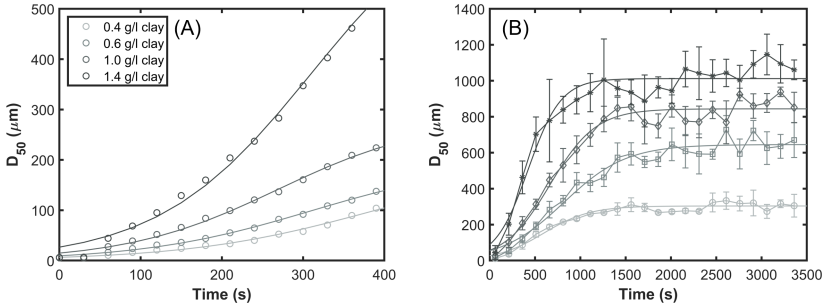


Figure 6.5: (Figure A): D_{50} as a function of time for the onset of flocculation; (Figure B): D_{50} as a function of time for the whole duration of the experiments. The error bars indicate the differences observed when averaging over 3 or 4 measurements; the curves indicate the fits; the parameters for the fit are given in table 6.1. The flocculant (Zetag 4110) to clay ratio is 2.5 mgg^{-1}.

experiment was replicated 3 or 4 times. The error bars in Figure 6.5 (right) represent the standard deviation when averaging over all experiments. The parameters used for fitting the data shown in this figure are given in table 6.1. As the parameter a_b was not changing much with clay concentration, the average value of a_b overall concentrations was chosen for each time series.

From the fit values for all clay concentrations used, the concentration dependence of L_{eq} and $k_b \simeq 1/t_b$ can be studied, see Figure 6.6 and Figure 6.7. Eq.(6.43) tells that at short Δt the flocculation rate should be linearly proportional to concentration. This is indeed found, even though the dependence on clay concentration is rather mild. For $\Delta t = \Delta t_{end}$ it is found that $t_b \simeq 1/k_b$ does not significantly depend on clay concentration. At short times, see Figure 6.7, it is observed that the flocculation rate $(dL/dt)_{t\to 0}$ is increasing

Table 6.1: Fit parameters related to Figure 6.5.

	$\Delta t = 400$ s				$\Delta t = \Delta t_{end}$			
$c(g/L)$	$L_{eq}(\mu m)$	$t_b(s)$	a_b	$k_b(s^{-1})$	$L_{eq}(\mu m)$	$t_b(s)$	a_b	$k_b(s^{-1})$
0.4	151	79	20	0.011	620	423	10.5	0.0021
0.6	145	98	20	0.009	598	368	10.5	0.0025
0.8	210	81	20	0.011	660	257	10.5	0.0035
1.0	269	81	20	0.011	928	277	10.5	0.0032
1.2	297	75	20	0.012	889	295	10.5	0.0030
1.4	469	85	20	0.011	918	202	10.5	0.0045
1.6	460	83	20	0.011	1013	208	10.5	0.0043

with clay concentration. It follows that $(dL/dt)_{t\to 0}$ scales with L_{eq} (not shown) since L_{eq} is increasing linearly with clay concentration, see Figure 6.6. It was observed that the low shear rate of 112 s^{-1} did not produce a continuous flow of flocs in the pipes. Repeated measurements have confirmed that this shear rate leads to a large experimental error, as is clear from Figure 6.5. For this reason, this shear rate was not used in subsequent shear rate dependence measurements, where only higher shear rates were used, which produced a continuous flow of flocs in the pipes. The advantage of working at 112 s^{-1} is that, in contrast to the shear experiments presented in the next section, the data can be fitted using only a birth function.

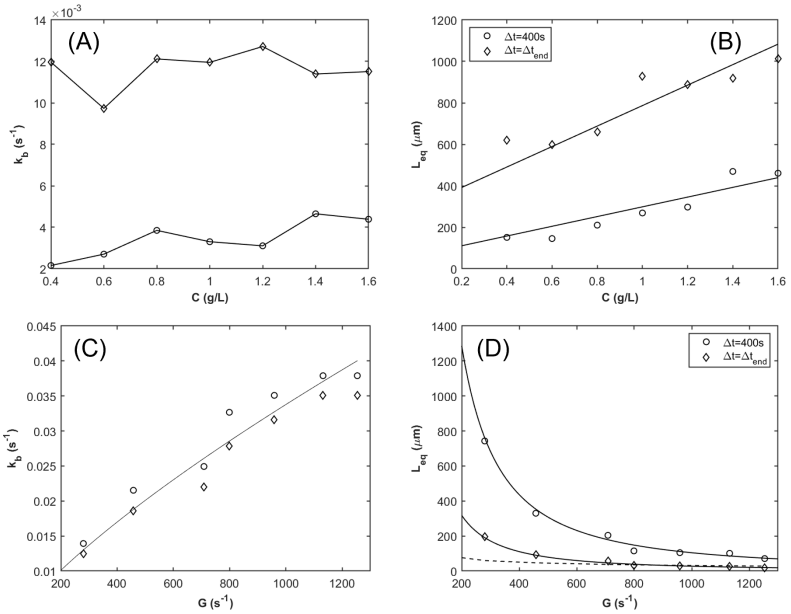


Figure 6.6: k_b and L_{eq} as function of clay concentration c (gL^{-1}) and shear G (s^{-1}). All suspensions have 2.5 mgg^{-1} flocculant (Zetag 4110) to clay ratio. A constant shear rate of 112 s^{-1} is applied for the concentration dependence figures. A clay concentration of 1.2 gL^{-1} is used on the shear rate dependence figures. The curves represent fits as indicated in the text.

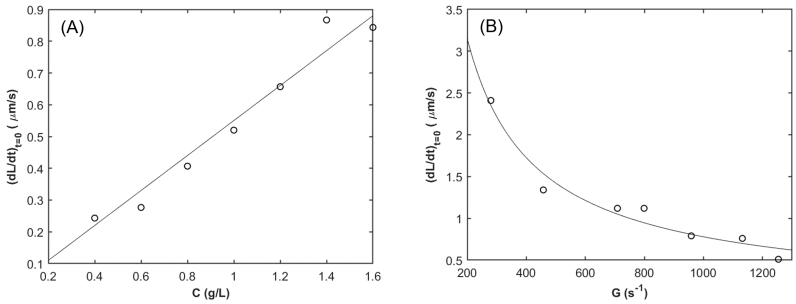


Figure 6.7: The slope at origin $(dL/dt)_{t\geq 0}$ as function of clay concentration c (gL^{-1}) and shear G (s^{-1}). All suspensions have 2.5 mgg^{-1} flocculant (Zetag 4110) to clay ratio. A constant shear rate of 112 (s^{-1}) is applied for the concentration dependence figures. A clay concentration of 1.2 gL^{-1} is used on the shear rate dependence figures. The curves represent fits as indicated in the text.

6.4.3. DEPENDENCE ON SHEAR

In order to study the effect of shear on the flocculation rate, experiments were performed at different shears for a given clay concentration of 1.2 gL^{-1} and flocculant (Zetag 4110) to the clay concentration ratio of 2.5 mgg^{-1}. Three examples of particle size distribution at different shears are given in Figure 6.2(bottom panel). The time evolution of the mean particle size is given in Figure 6.8. Every experiment was reproduced 3 or 4 times, leading to the error bars represented in the figure. The parameters used for fitting the data shown in this figure are given in Table 2. As the parameter a_b was not changing much with shear and time Δt, the average value of a_b overall shears was chosen for the all-time series. At short times ($\Delta t = 400$ s) only a birth function was used for the fit.

As discussed in (Shakeel et al., 2020), after a shearing period at sufficiently high shear, the dangling ends of flocs tend to coil, and the flocs get smaller until they reach a size that is in good approximation equal to the Kolmogorov microscale, see Figure 6.8. In order to fit the decrease of L over time, it is necessary to introduce a decay term, as shown in section 6.4.3. This decay is associated with a large characteristic time t_d resulting in a small k_d as in good approximation $t_d \simeq 1/k_d$. The associated parameters are given in Table 2. It was found that the parameter a_d was not changing much with shear, and it was therefore taken equal to its average value over all shears. From the fit values for all shears

Table 6.2: Fit parameters related to Figure 6.8.

	$\Delta t = 400$ s				$\Delta t = \Delta t_{end}$						
$G(s^{-1})$	$L_{eq}(\mu m)$	$t_b(s)$	a_b	$k_b(s^{-1})$	$L_{eq}(\mu m)$	$t_b(s)$	a_b	$k_b(s^{-1})$	$t_d(s)$	a_d	$k_d(s^{-1})$
281	743	68	18	0.014	195	76	18	0.012	3382	3.5	2.3×10^{-4}
427	330	44	18	0.021	93	51	18	0.018	1319	3.5	5.9×10^{-4}
635	204	38	18	0.025	56	43	18	0.022	1246	3.5	6.2×10^{-4}
807	115	29	18	0.032	32	34	18	0.027	869	3.5	8.9×10^{-4}
958	105	27	18	0.035	28	30	18	0.031	931	3.5	8.3×10^{-4}
1147	101	25	18	0.038	26	27	18	0.035	1249	3.5	6.2×10^{-4}
1336	71	25	18	0.036	17	27	18	0.033	2198	3.5	3.5×10^{-4}

used, the shear dependence of L_{eq} and k_b can be studied, see Figures 6.6 and 6.7. The decrease of L_{eq} with shear is modelled by:

$$\begin{aligned} L_{eq}(\Delta t = 400s) &= 5\times10^{6}G^{-1.56} \\ L_{eq}(\Delta t = \Delta t_{end}) &= 1\times10^{6}G^{-1.52} \end{aligned} \tag{6.46}$$

where it should be noted that L_{eq} is given in μm. For both $\Delta t = 400$ s and $\Delta t = \Delta t_{end}$ it is found that k_b is proportional to shear between 281 s^{-1} and 1336 s^{-1} (see Table 2 and Figure 6.6) according to:

$$k_b \simeq \frac{1}{t_b} \simeq 1.9\times10^{-4}G^{0.75} \tag{6.47}$$

This leads to the following correlation between L_{eq} and k_b:

$$\begin{aligned} L_{eq}(\Delta t = 400s) &\simeq 0.022k_b^{-2.07} \\ L_{eq}(\Delta t = \Delta t_{end}) &\simeq 0.1k_b^{-2.07} \end{aligned} \tag{6.48}$$

where again L_{eq} is given in μm. At high shear ($> 700s^{-1}$) and $\Delta t = \Delta t_{end}$ it is found that L_{eq} follows the trend predicted by the Kolmogorov microscale, and therefore can be approximated by:

$$L_{eq}\left(\Delta t = \Delta t_{end}, G > 700s^{-1}\right) = \left(\frac{G}{\upsilon}\right)^{-0.5} \tag{6.49}$$

where $\upsilon = 10^{-6}$ m^2/s is the kinematic viscosity of water. As is clear from fig. 6.6, for $G > 700s^{-1}$ the curves representing eqs.(6.46,6.49) are in close agreement, and the difference in power of G is not noticeable. Eqs.(6.46) can therefore be used for the whole range of shear investigated.

The slope at origin $(dL/dt)_{t\to0}$ decreases with G, which is in line with the estimation obtained from section 6.4.3, using eq. (6.8):

$$(dL/dt)_{t\to0} = k_B L(t\to0) \simeq k_b^{-1.07} \simeq G^{-0.8} \tag{6.50}$$

The fit (black curve in Figure 6.7) gives, with $(dL/dt)_{t\to0}$ in μm/s :

$$(dL/dt)_{t\to0} = 313G^{-0.8} \tag{6.51}$$

6.5. CONCLUSIONS

In this chapter, two models for flocculation, one based on logistic growth theory (LG model) and the other on Smoluchowski's approach (S model), have been compared. Two series of experiments have been used for the comparison to explore the dependence of the model parameters on shear and clay concentration. It was found that the kinetics of flocculation can be modelled with the LG model, whereas the S model does not reproduce the observed dependence on time of the mean floc size (D_{50}) represented by $L(t)$. By fitting the time evolution of $L(t)$, it was found that both the equilibrium floc size L_{eq} and t_b which are parameters for the LG model, are a function of the time interval used for

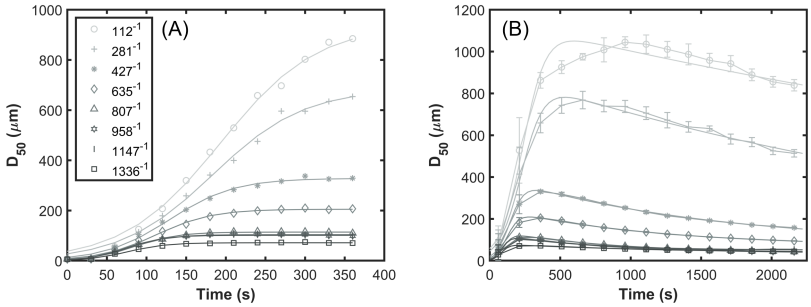


Figure 6.8: A): D_{50} as a function of time for the onset of flocculation; the curves indicated the fits; B): D_{50} as a function of time for the whole duration of the experiments. The error bars indicate the differences observed when averaging over 3 or 4 measurements; the parameters for the fit are given in table 6.2; The flocculant (Zetag 4110) to clay ratio is 2.5 mgg^{-1} for 1.2 gL^{-1} clay.

fitting. This was linked to the change in flocculation kinetics over time: at the onset of the experiment, the flocculation is dominated by the aggregation of unbonded mineral clay to polyelectrolyte strands, whereas at larger times, the flocculation is dominated by floc-floc aggregation. It was found that the floc-floc aggregation could be modelled over the whole experimental time interval with the same parameters, using the LG model. As has already been reported (Elimelech et al., 1995; Shakeel et al., 2020), flocs created by the addition of polyelectrolyte re-conform in the flow over time. This leads to a decrease in floc size at long time scales. The LG model can be used to model both growth and decay occurring over time, from which the characteristic timescales for growth and decay can be found. Not accounting for this decrease occurring at a long time, a general fitting function for a system of suspended clay destabilized by the addition of flocculant is found using Eqs.(6.46,6.47) and is given by:

$$L(t) = a_L c G^{-1.5} \frac{1}{1 + a_b exp\left(-a_t G^{0.75} t\right)} \tag{6.52}$$

where a_L, a_b and a_t are empirical parameters that do not depend on concentration nor shear. These parameters, however, are expected to be a function of the flocculant-to-clay ratio, which in the present study was kept constant. To give an order of magnitude, based on the fits reported in the current chapter, $a_L \simeq 5 \times 10^6$ (μm.L.g^{-1}.$s^{1.5}$), $a_b \simeq 20$ and $a_t \simeq 2 \times 10^{-4}$ ($s^{-0.25}$). Eq.(6.52) can be differentiated to:

$$\frac{dL}{dt} = a_b a_t G^{0.75} \frac{exp\left(-a_t G^{0.75} t\right)}{1 + a_b exp\left(-a_t G^{0.75} t\right)} L \tag{6.53}$$

Eq.(6.53) is of the type that can be implemented in a sediment transport model. The measurement protocol used in this chapter is on clay in the presence of polyacrylamide flocculant can be used to study any kind of system, in particular sediment collected from the CCZ zone. The reason this was not done in the present thesis is that not enough material was available at the time of the study.

7

Conclusions and Recommendations

This chapter summarises the outcomes of the dissertation in the form of answers to the sub-questions and the main research question presented in Chapter 1. The main findings of the research are given, along with critical comments. Finally, recommendations for further research are presented.

7.1. CONCLUSIONS

In order to control the spread of turbidity flows originating from DSM, one needs to get a better understanding of these flows. In particular, it is important to study how sediment particle size and settling velocity impact the propagation of turbidity currents. A working hypothesis in this thesis has been that particle aggregation, which enhances particle size and settling velocity, would lead to a reduction of this propagation. The main objective of this thesis has been to study how flocculation influences turbidity currents as a function of different parameters, such as flocculant type and dosage and shear stresses.

Chapter 3 showed a series of lock-exchange experiments, that were conducted for various sediment types, to study the influence of flocculation on the propagation of turbidity flows. Subsequently, in Chapter 4, a thorough analysis of floc size distributions and settling velocities as a function of sampling methods was presented. In Chapter 5, the flocculation of deep-sea clay was studied, as a function of clay concentrations, shear rates and mixing times. In Chapter 6, a recently proposed flocculation model was compared to an established one. The model was subsequently parameterized to be of use in a sediment transport model.

7.1.1. EFFECT OF FLOCCULATION ON TURBIDITY FLOW

The objective of the lock exchange experiment was to investigate the effect of flocculation on the spread of turbidity current. The experiments conducted in lock exchange have shown that:

1. The propagation behaviour of a lock-exchange turbidity current is influenced by particle size and initial sediment concentration. Larger particles possess higher settling velocities due to their increased mass and are more prone to rapid settling when compared to smaller particles. This will lead to a limited propagation of the turbidity current. On the contrary, smaller particles, being lighter, tend to remain suspended for longer durations, leading to a slower settling rate and thus a larger stretch of the turbidity current. The initial sediment concentration (the concentration in the mixing tank of the lock) significantly influences the current's behaviour. Higher initial sediment concentrations lead to denser turbidity currents. These denser flows have increased momentum, allowing them to travel further distances and carry more substantial sediment loads. Conversely, lower initial sediment concentrations result in lighter turbidity currents with reduced momentum and sediment-carrying capacity. These results are in line with previous studies (Elerian, 2023; Hallworth et al., 1998; Hallworth and Huppert, 1998).
2. When an organic flocculating agent, specifically an anionic polyelectrolyte, was used in the mixing tank, leading to the creation of flocs, it was found that the propagation of the turbidity currents was limited, following the reasoning of point 1 (the flocs were larger than the unflocculated sediment particles). It was found that the propagation in saline water extended less than in freshwater, as it was shown that flocs in a saline environment had a higher settling velocity than in fresh water.
3. When studying the particle size distributions as a function of the position in the lock, it was found that the particle sizes varied depending on the environmental conditions: for the same flocculant to clay ratio, flocs created in freshwater were

larger than in salt water, and their mean size increased as the distance from the mixing tank increased. This showed that aggregation occurred during the small residence time of the flocs in the water (a few minutes).

4. In fresh water, the flocculation in the mixing tank is incomplete due to the scarcity of cations that act as a binding agent between negative clay and negative polyelectrolyte. Flocs, clay particles, and unbounded flocculant which are released in the lock can therefore flocculate during the current propagation. In saline water, on the other hand, flocs are fully formed in the mixing tank, and releasing them in the lock compartment just advect them. In saline environments, flocs are smaller than in fresh water owing to the coiling of the polyelectrolyte, due to the screening of the electrostatic repulsion between the charged groups of the polyelectrolyte. This leads to the fact that saline water flocs have a higher density (and higher settling velocity) compared to freshwater flocs.

It can be concluded that flocculation indeed reduces the spread of turbidity currents. As flocculation is quite rapid (over a timescale of a few minutes), flocculation impacts the propagation of density currents in lock exchange experiments.

7.1.2. EFFECT OF CONCENTRATION ON THE EVALUATION OF A PARTICLE'S SETTLING VELOCITY IN TURBIDITY CURRENTS

The experiments conducted to study the effect of the concentration of particles on floc size and settling velocities have shown that:

1. It has been demonstrated that the number of sampled flocs significantly changes the settling velocity of flocs. The settling velocity of single flocs is always smaller than the settling velocity of flocs of the same size observed using batch sampling.
2. Due to collective settling, flocs with different sizes fall with the same settling velocity. Even the largest flocs are affected by the hydrodynamics of collective sampling. In turbidity current, collective settling can play a significant role in the settling of particles.
3. There is an increase in floc settling velocity with clay concentration, at a given flocculant to clay ratio, after one hour of mixing at low shear. Denser and larger flocs are created at larger clay concentrations.

Sampling methods, and in particular the number of particles transferred in the settling column for video analysis, strongly impact the settling velocities of the sampled particles, although the settling velocities are recorded about 30 cm below the injection point, where collective effects were expected to be minimal. It is also known that the settling of particles is dependent on the size of the container even for very dilute suspensions (Guazzelli and Morris, 2011). This implies that settling column experiments cannot be used to evaluate the effective density of flocs assuming Stokes settling velocity, as is often done.

7.1.3. EFFECT OF CLAY CONCENTRATION, SHEAR RATES AND FLOC REST TIME ON FLOCCULATION OF DEEP-SEA CLAY COLLECTED FROM CLARION CLIPPERTON ZONE

The experiments conducted to study the effect of mixing time, clay concentration, and shear rates on floc size and settling velocities have shown that:

1. It was found that deep-sea clay, collected from two different deep-sea areas in the CCZ, flocculated over time when mixed in saline water within a few minutes.
2. At low clay concentration (0.5 gL^{-1}), floc size increases with mixing time and remains smaller than the Kolmogorov microscale whereas at higher concentration (2 gL^{-1}) the median floc size decreases after 5 min of mixing when flocs exceed the Kolmogorov microscale. This is attributed to the fact that flocs larger than the Kolmogorov length will reconform or erode.
3. Flocs containing more organic material have their settling velocity increasing with mixing time, as they are more prone to reconformation.
4. The dependence of floc size upon shear leads us to conclude that there is a low affinity for both water and mineral clay, but that there is a higher affinity for clay than water, which results in the fact that flocculation is prevented at low shear, as the hydrophobic organic matter would then remain in the state of coiling that does not promote flocculation.
5. At shear rates higher than 125 s^{-1}, the organic matter is expected to uncoil, as larger median floc sizes are observed and these floc sizes increase with shear. If this hypothesis is correct, it would imply that the steady state observed for each shear corresponds to a balance between aggregation and break-up. The aggregation rate would be proportional to the collision frequency coupled to a small collision efficiency, whereas the break-up rate would be much less (or not at all) dependent on shear.
6. Results found during residence time experiments in jars seem to confirm our hypothesis. There appears to be a low affinity between organic matter and water leading to the binding of organic matter to mineral clay.
7. At long residence time in the jar, the median floc size is observed to decrease. This is attributed to a redistribution of the hydrophobic organic matter on the mineral clay
8. Flocculation with deep-sea clay was performed in a new rotating wheel, and the median floc size was compared to the one found using jar tests. It was found that the hydrodynamics in the wheel led to larger median floc sizes in the wheel than in the jar. The reason for this difference is attributed to the same reason that has been proposed to explain the residence time experiments: organic matter coming into contact with clay at very low shear will bind and lead to large flocs. Similarly to the resting time tests, this flocculation occurred very rapidly (within 2.5 minutes). After 30 minutes, the median floc size started reducing.
9. While analysing the video at 5 gL^{-1} it was found that flocs started to disintegrate during the settling process. This is in line with the hypothesis proposed for the resting time experiments: the rearrangement of the organic material on the clay (minimizing contact with water) causes the flocs to break up

It was found that deep-sea clay indeed flocculates rapidly (in 2.5 minutes) in saline conditions and that the organic matter is rather hydrophobic and has surfactant properties. This would be in line with the characteristics of organic substances like phospholipids, which are key components of cell membranes and are found in the deep sea.

7.1.4. PARAMETRIZATION OF FLOCCULATION MODELS

The thorough study of a recently published flocculation model has shown that

1. The newly proposed model reproduces the measured flocculation kinetics whereas models based on Smoluchowski do not.
2. It was shown, by fitting the model to the data, that both equilibrium floc size and flocculation rate are time-dependent, as different flocculation mechanisms are observed as a function of time. In the early stages of flocculation, flocs are predominantly formed by the aggregation of unbound mineral clay particles with polyelectrolyte strands. At later stages, flocculation is predominantly governed by the aggregation of floc-to-floc interactions.
3. It was shown that the model could be parameterized by performing a series of measurements in the lab. An easy-to-implement formulation is proposed, giving the rate of change of the median floc size as a function of clay concentration and shear rate, for a given flocculant-to-clay ratio.

The flocculation model based on logistic growth used in this thesis could indeed be parameterized and is easy to implement in a sediment transport model.

7.2. SUMMARY AND RECOMMENDATIONS

Experiments with deep-sea clay have demonstrated that flocculation indeed plays a significant role, in the large range of concentrations and shears investigated. In particular, considering the short timescales required for flocculation, and the hydrophobic nature of organic matter, it is expected that flocculation plays a noteworthy role in plumes generated by mining activities in the deep sea. The results obtained within this research are however quite generic and they are expected to be applied to other types of density currents and sediment plumes, such as the ones obtained from dredging activities. In particular, the design of mining or dredging equipment could be adapted to make use of the role of organic matter as flocculant, and hereby reduce the impact of sediment plumes. The way the flocculation model was parameterized in this thesis serves as the protocol to apply to set up similar models, for other clay suspensions. These models can easily be implemented in sediment transport models and subsequently be tested.

More specific recommendations, regarding the experiments performed in the course of this PhD work are given below.

- Due to a lack of material, the turbidity currents generated through lock exchange experiments were performed using illite clay and an ionic polyelectrolyte. Considering the peculiar nature of deep-sea organic material, as found in the jar test experiments, it would be interesting to repeat lock-exchange experiments with deep-sea clay.

- While experiments in the lock exchange were performed with a given mixing protocol, future research should consider exploring different initial mixing conditions to account for the varying states of clay within the PNMT over time.
- The experiments in the present study were constrained by the small dimensions of the lock exchange setup. Extending the length of the lock would allow for the complete evolution of turbidity current dynamics.
- Having a setup that replicates at best deep sea conditions (the action of a PNMT on the local hydrodynamics, presence of an erodable bed) would enable to study the importance of flocs and flocculation in a more realistic way. The lock exchange experiments in this thesis were performed in a lock without any deposited material. It would be very interesting, for instance, to study the influence of a sediment bed on the propagation of the sediment flow. Studying the action of a PNMT requires adjustments to the lock exchange set-up.
- Considering the influence of batch settling on the settling velocity of flocs, it is suggested to optimize the settling column's dimensions and adapt the floc transfer protocol (ideally transferring flocs one by one) to mitigate collective effects during settling. By increasing the column size hydrodynamic effects such as return flow and influence of the column walls can be minimised.
- Comparing laboratory measurements of floc size and settling velocities for naturally flocculated deep-sea clay with in-situ data is essential. A camera system similar to FLOCCAM should be deployed to the seafloor to characterise PSD better.
- Both deep-sea clay and the organic matter within it should be better characterized. In particular, it would be interesting to validate the hypothesis that the deep sea organic matter is indeed hydrophobic in nature.

A

APPENDIX A

FLOCCULATION IN TURBIDITY CURRENTS

DISTANCE TRAVELLED BY PLUME HEADS

The 10, 30, and 100 $g L^{-1}$ illite experiments with 0.25 $mg g^{-1}$ flocculant are displayed in Figure A.1 in terms of the distance travelled by the sediment plume within the video recording range. Whereas for the ACCZ case 10 and 30 $g L^{-1}$ experiments with 0.25 $mg g^{-1}$ flocculant are displayed in Figure A.2.

MEAN FLOC SIZE AS A FUNCTION OF TRAVEL DISTANCE

The mean floc size of 10, 30, and 100 $g L^{-1}$ illite experiments with 0.25 $mg g^{-1}$ flocculant are displayed in Figure A.3 and for the ACCZ case 10 and 30 $g L^{-1}$ experiments with 0.25 $mg g^{-1}$ flocculant are displayed in Figure A.4.

PARTICLE SIZE AND SETTLING VELOCITY DISTRIBUTIONS AS A FUNCTION OF TRAVEL DISTANCE

The settling velocities and the particle sizes of 100 $g L^{-1}$ illite experiment with 0.25 $mg g^{-1}$ flocculant for fresh and saltwater cases are displayed in Figures A.5 and A.6 respectively. The results for ACCZ in case of 30 $g L^{-1}$ experiments with 0.25 $mg g^{-1}$ flocculant are displayed in Figures A.7 and A.8.

A

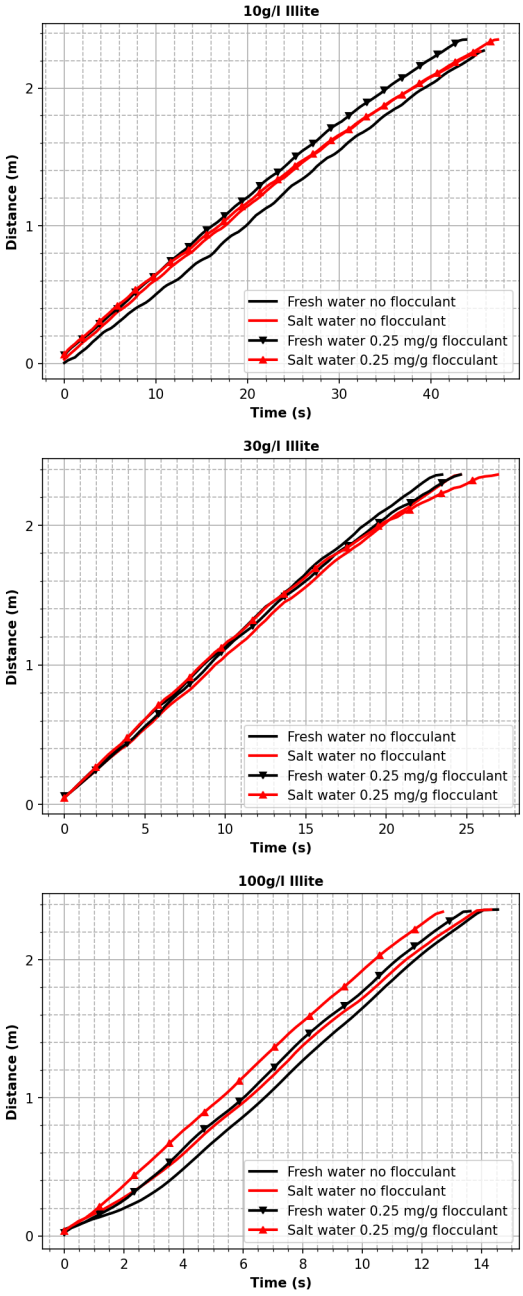


Figure A.1: Change in distance as a function of time for $10\,\mathrm{g\,L^{-1}}$ (top), $30\,\mathrm{g\,L^{-1}}$ (middle) and $100\,\mathrm{g\,L^{-1}}$ (bottom) of illite. Solid green lines represent experiments done in freshwater and dashed red lines show experiments done in saltwater. Only results with $0.25\,\mathrm{mg\,g^{-1}}$ of flocculant are shown in these figures.

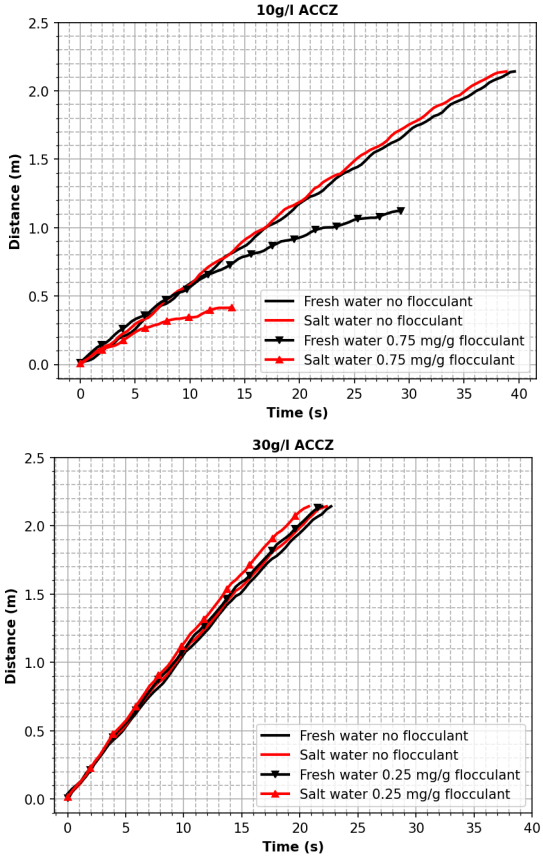


Figure A.2: Change in distance as a function of time for 10 $g L^{-1}$ (top) and 30 $g L^{-1}$ (bottom) of ACCZ. Solid green lines represent experiments done in freshwater and dashed red lines show experiments done in saltwater. Only results with 0.25 $mg g^{-1}$ of flocculant are shown in these figures.

A

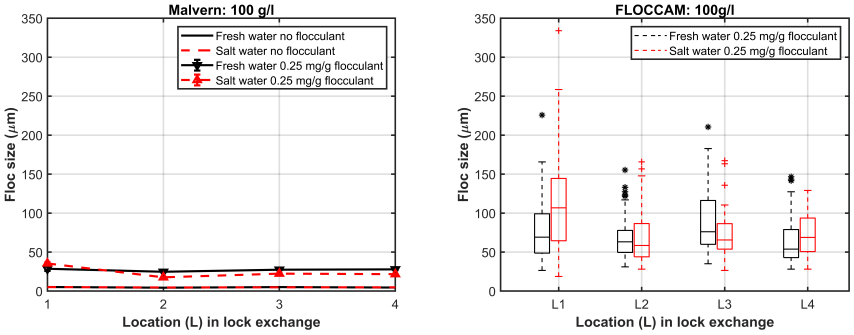


Figure A.3: Hydrodynamic diameter of illite flocs for 100 gL^{-1} experiments at different locations (L1-L4) in the lock exchange for illite. Left: results obtained by SLS (Malvern instrument) and right results obtained from FLOCCAM. Solid green lines represent experiments done in freshwater and dashed red lines show experiments done in saltwater. Only results with 0.25 mgg^{-1} of flocculant are shown in these figures.

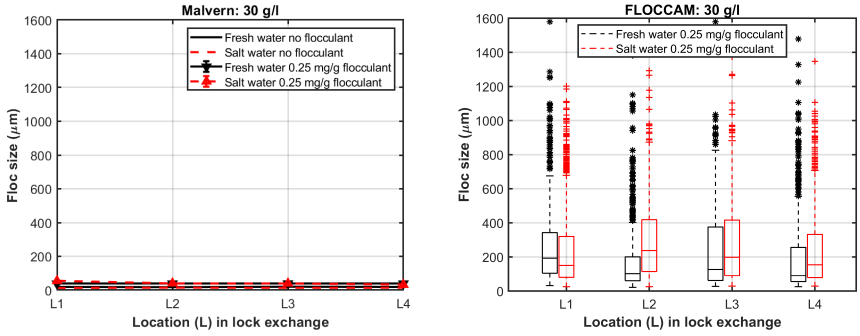


Figure A.4: Hydrodynamic diameter of illite flocs for 30 gL^{-1} experiments at different locations (L1-L4) in the lock exchange for ACCZ. Left: results obtained by SLS (Malvern instrument) and right results obtained from FLOCCAM. Solid green lines represent experiments done in freshwater and dashed red lines show experiments done in saltwater. Only results with 0.25 mgg^{-1} of flocculant are shown in these figures.

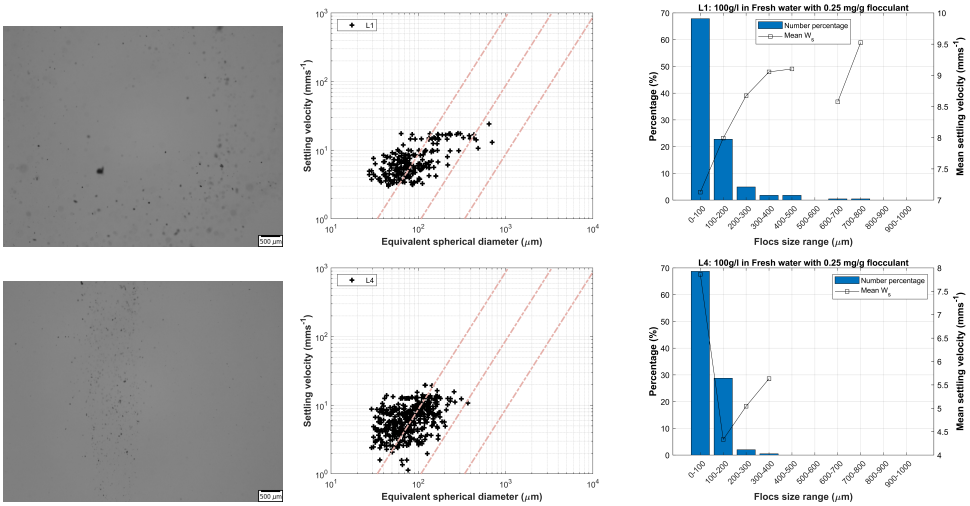


Figure A.5: Settling velocity and particle size analysis of the sub-samples collected at location L1 (top panels) and L4 (bottom panels) during lock exchange experiments with 100 gL^{-1} illite and 0.25 mgg^{-1} of flocculant in freshwater. Settling velocity is derived as a function of equivalent spherical diameter, with diagonal dashed lines representing the contours of effective density (kgm^{-3}). Dashed lines represent the iso-lines calculated by using the Stokes equation(from left to right: 1600,160,16). The right panels show the floc size range and mean settling velocity. The images of the flocs are given in the left panels.

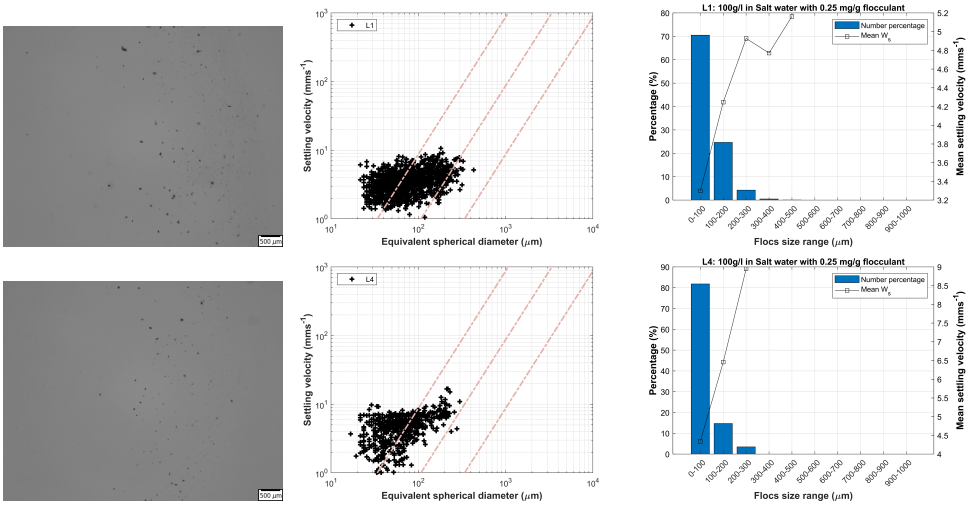


Figure A.6: Settling velocity and particle size analysis of the sub-samples collected at location L1 (top panels) and L4 (bottom panels) during lock exchange experiments with 100 gL^{-1} illite and 0.25 mgg^{-1} of flocculant in saltwater. Settling velocity is derived as a function of equivalent spherical diameter, with diagonal dashed lines representing the contours of effective density (kgm^{-3}). Dashed lines represent the iso-lines calculated by using the Stokes equation(from left to right: 1600,160,16). The right panels show the floc size range and mean settling velocity. The images of the flocs are given in the left panels.

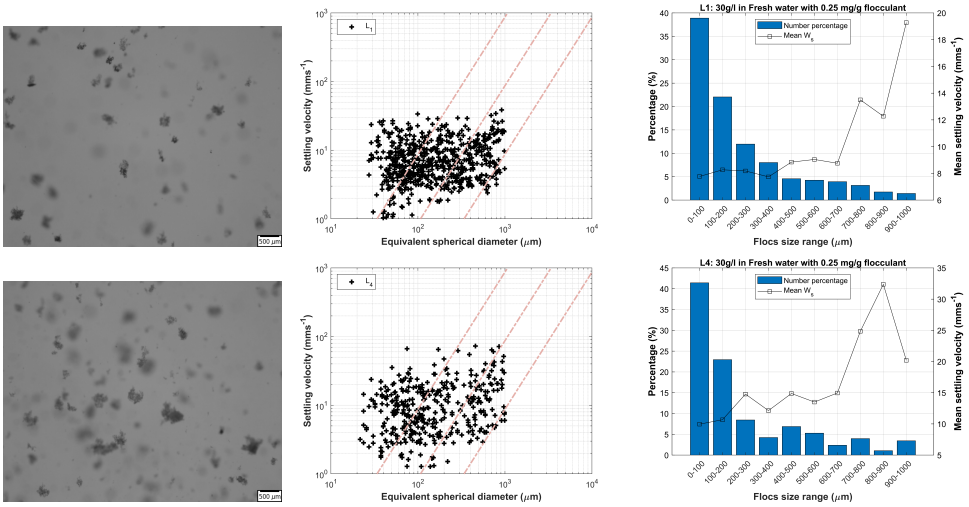


Figure A.7: Settling velocity and particle size analysis of the sub-samples collected at location L1 (top panels) and L4 (bottom panels) during lock exchange experiments with 30 gL^{-1} ACCZ and 0.25 mgg^{-1} of flocculant in freshwater. Settling velocity is derived as a function of equivalent spherical diameter, with diagonal dashed lines representing the contours of effective density (kgm^{-3}). Dashed lines represent the iso-lines calculated by using the Stokes equation(from left to right: 1600,160,16). The right panels show the floc size range and mean settling velocity. The images of the flocs are given in the left panels.

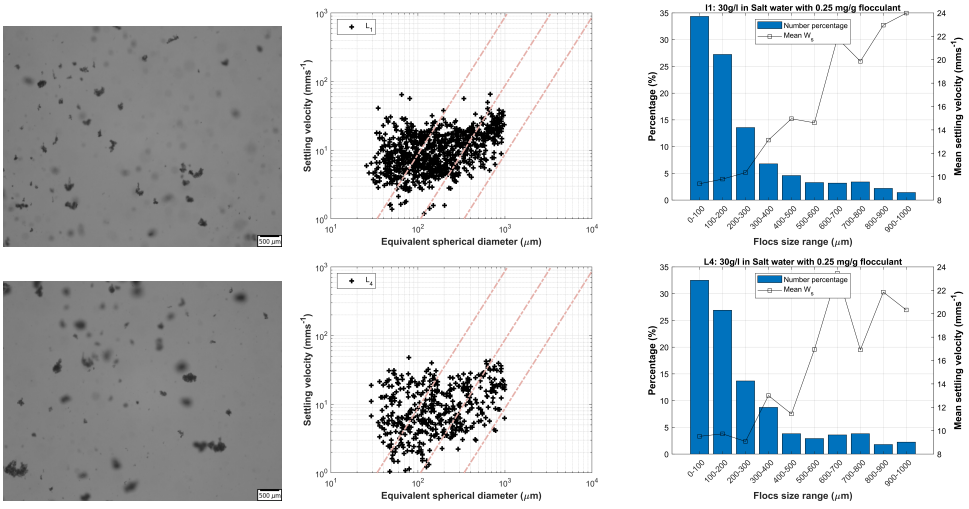


Figure A.8: Settling velocity and particle size analysis of the sub-samples collected at location L1 (top panels) and L4 (bottom panels) during lock exchange experiments with 30 gL^{-1} ACCZ and 0.25 mgg^{-1} of flocculant in saltwater. Settling velocity is derived as a function of equivalent spherical diameter, with diagonal dashed lines representing the contours of effective density (kgm^{-3}). Dashed lines represent the iso-lines calculated by using the Stokes equation(from left to right: 1600,160,16). The right panels show the floc size range and mean settling velocity. The images of the flocs are given in the left panels.

B

APPENDIX B

SETTLING VELOCITIES IN TURBIDITY CURRENTS
SETTLING VELOCITY AND PARTICLE SIZE

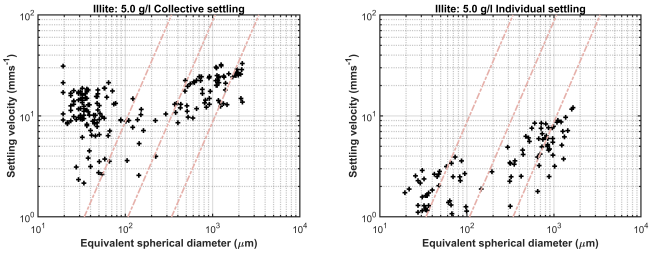


Figure B.1: Settling velocity and particle size analysis of $5\,\mathrm{gL}^{-1}$ experiment for both collective (left) and individual settling (right) cases. Settling velocity is plotted as a function of equivalent spherical diameter, with diagonal dashed lines representing effective density iso-lines calculated by using Stokes equation (from left to right: 1600,160,16 (kgm^{-3})).

B

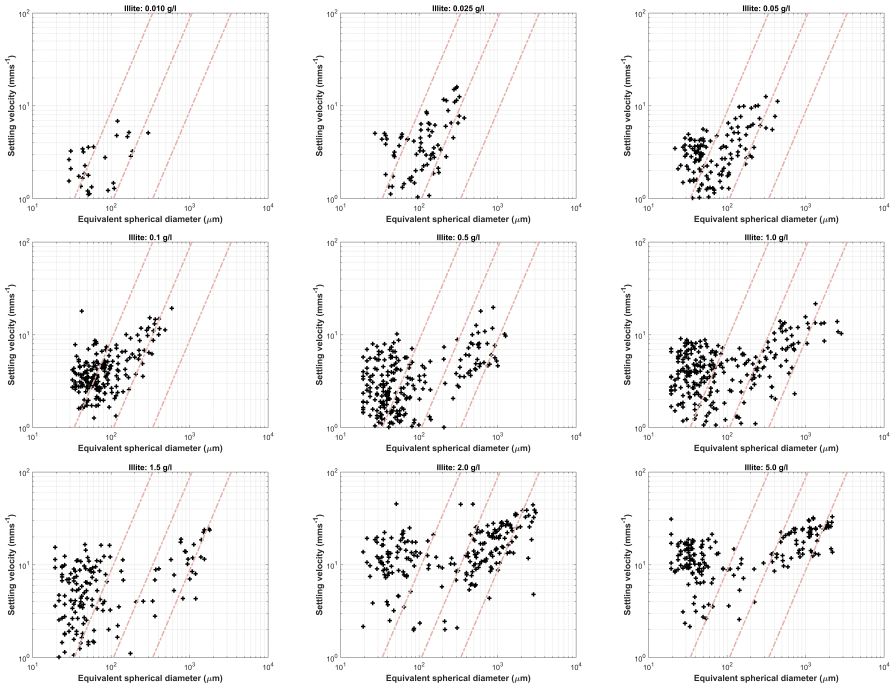


Figure B.2: Settling velocity and particle size analysis for all concentrations (0.01 to 5.0 gL^{-1}). Settling velocity is plotted as a function of equivalent spherical diameter, with diagonal dashed lines representing effective density iso-lines calculated by using Stokes equation (from left to right: 1600,160,16 (kgm^{-3})).

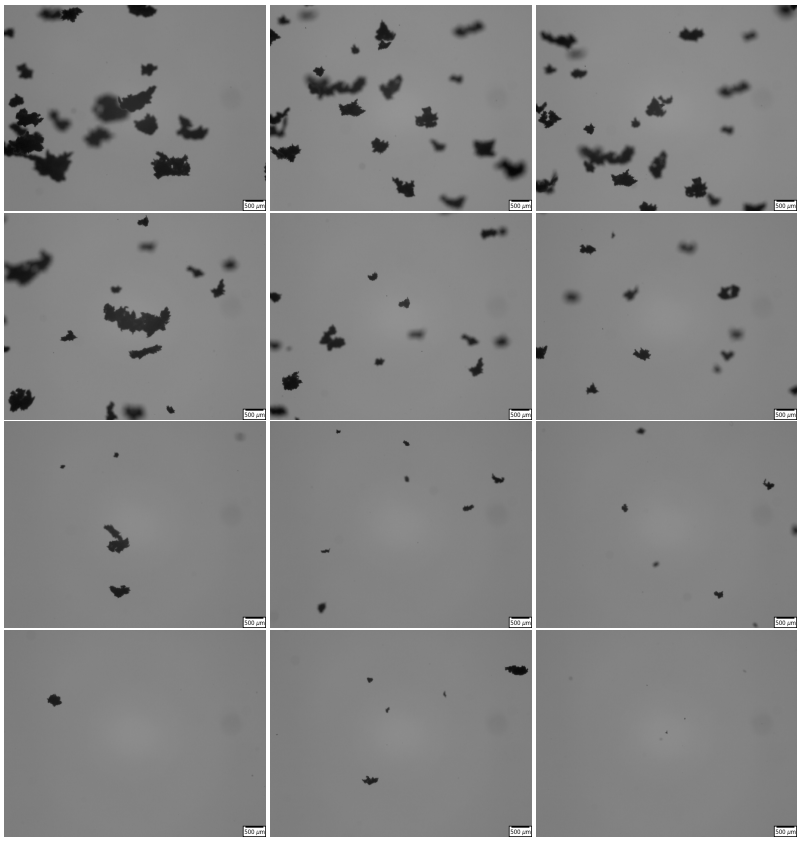


Figure B.3: Snapshots of the videos for 5.0 gL^{-1} experiment for the collective settling case. These snapshots (from top to bottom) show the transition in a number of flocs appearing in front of the camera from start to end frame.

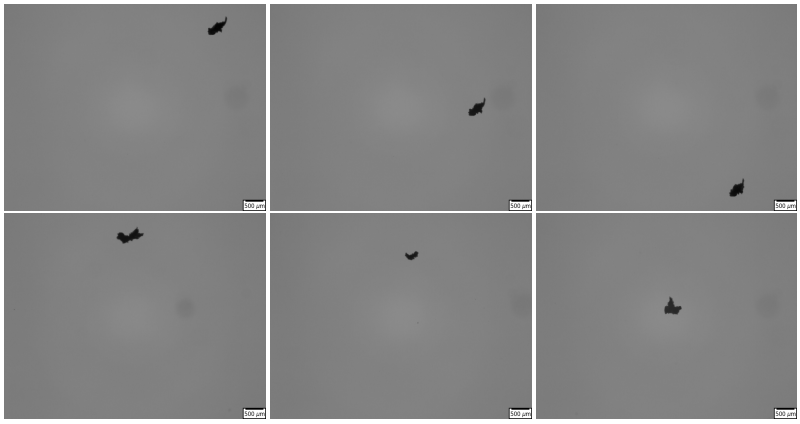


Figure B.4: Snapshots of the videos for 5.0 gL^{-1} experiment for the individual settling case. The top row displays the settling of the same particle as a function of time.

C

APPENDIX C

FLOCCULATION AND SETTLING OF DEEP-SEA CLAY

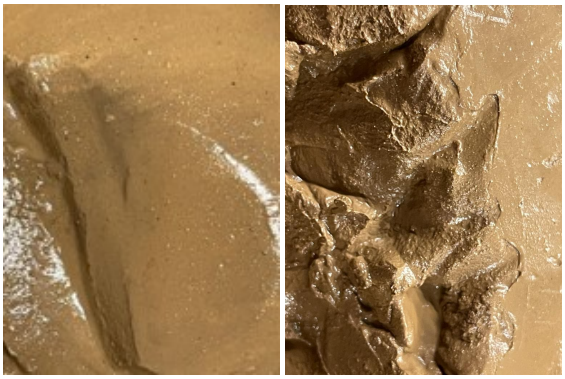


Figure C.1: Snapshots depicting the form of deep-sea clay as it was received, (Left) Clay 1, (Right) Clay 2.

C

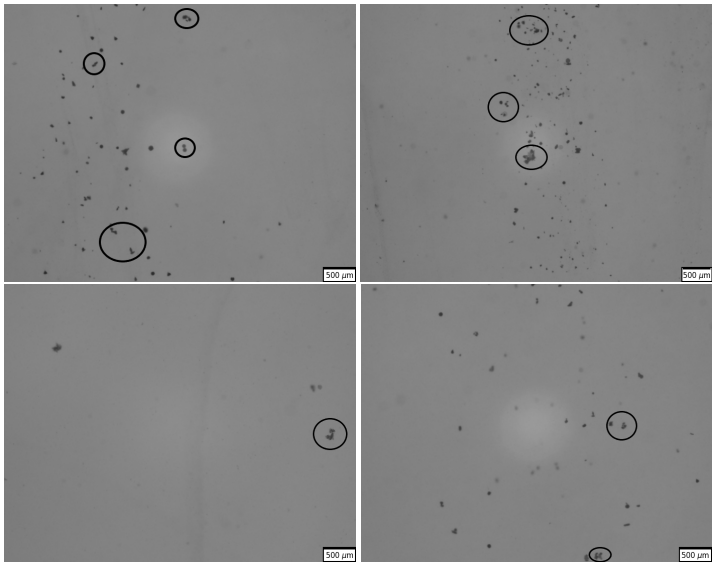


Figure C.2: Snap shot of the flocs from FLOCCAM videos showing floc-floc aggregates (highlighted in black) after different mixing times for Clay 1 at 5.0 $g L^{-1}$. (Top left) is after 2.5 minutes, (Top right) is after 30 minutes, (Bottom left) is after 60 minutes, and (Bottom right) is after 120 minutes.

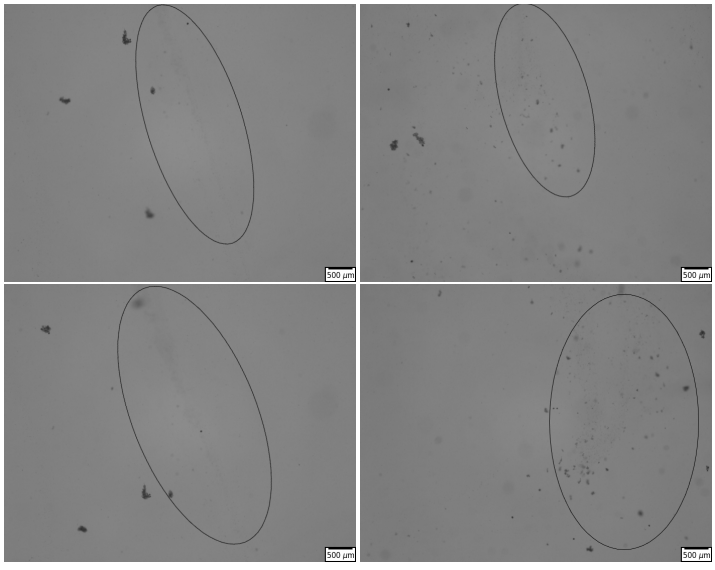


Figure C.3: Snap shot of the flocs from FLOCCAM videos showing aggregates with swirls of organic matter after 120 minutes of mixing times for Clay 1 at 2.0 $g L^{-1}$.

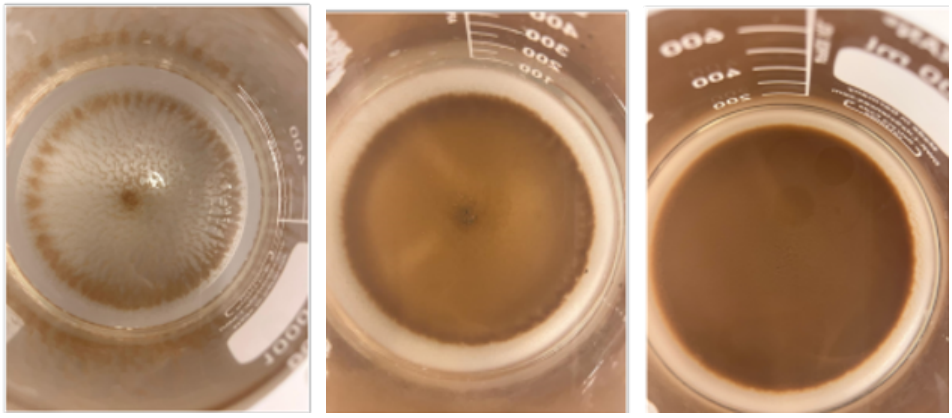


Figure C.4: Picture of resting flocs at the bottom of the jar after flocculation experiment on day 1. (Left) 0.5 gL^{-1}, (Middle) 2.0 gL^{-1}, (Right) 5.0 gL^{-1}.

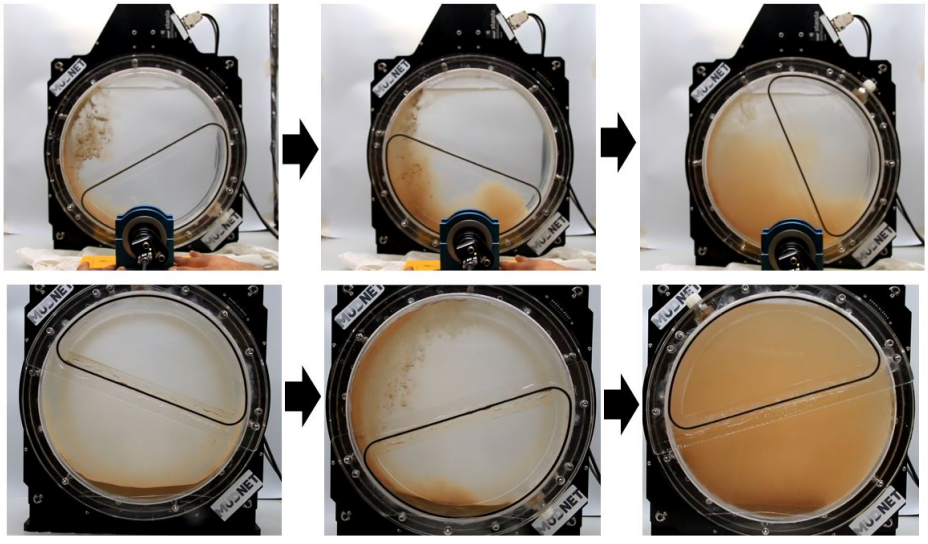


Figure C.5: Images of wheel at different intervals showing flocculation experiment. (Top figure) 0.5 gL^{-1} (Bottom figure) 2.0 gL^{-1}.

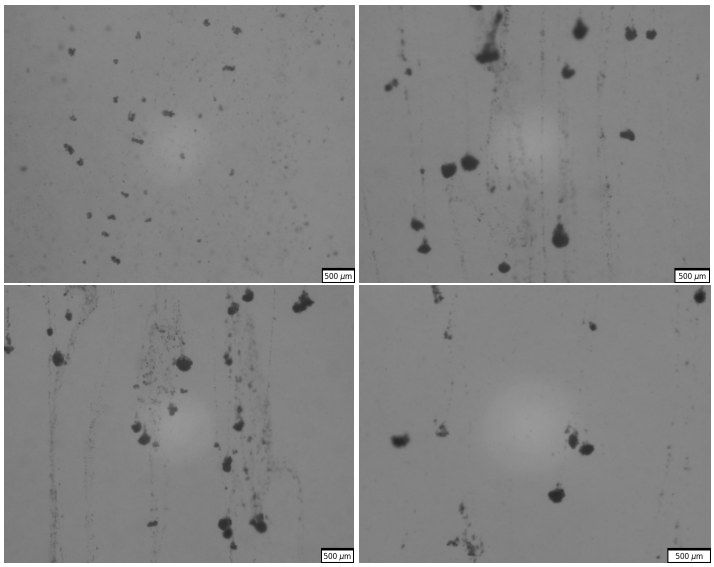


Figure C.6: Snap shot from FLOCCAM videos showing flocs breaking up after different mixing times for Clay 1 in the wheel at 5.0 gL^{-1}. (Top left) is after 2.5 minutes, (Top right) is after 30 minutes, (Bottom left) is after 60 minutes, and (Bottom right) is after 120 minutes.

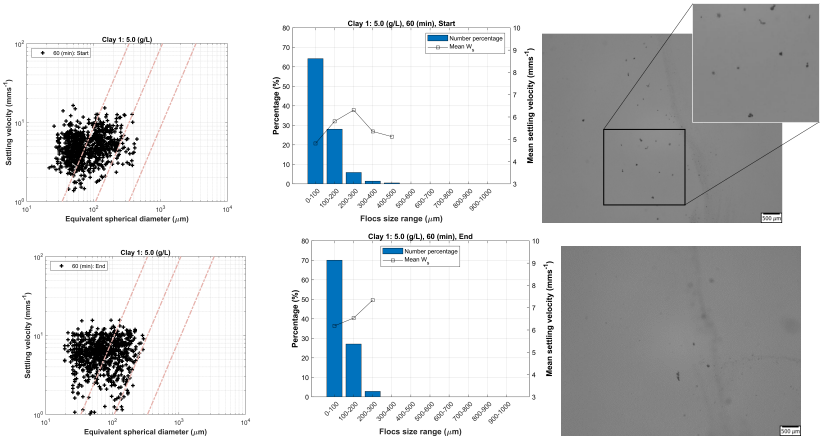


Figure C.7: (Top & Bottom left): Settling velocity and particle size analysis of Clay 1 at the start and end of the shear experiment for the concentration of 5.0 gL^{-1}. Settling velocity is derived as a function of equivalent spherical diameter, with diagonal dashed lines representing effective density contours calculated using the Stokes equation (from left to right: 1600, 160, 16 (kgm^{-3})). (Top & Bottom mid) the floc size range and mean settling velocity. (Top & Bottom right) snapshots of the videos.

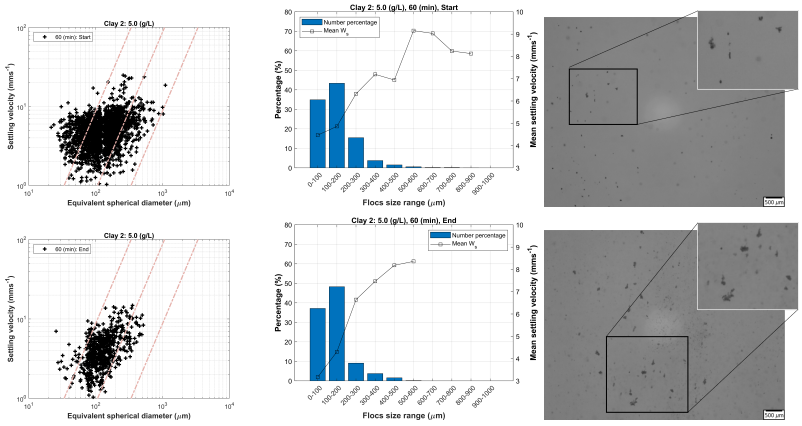


Figure C.8: (Top & Bottom left): Settling velocity and particle size analysis of Clay 2 at the start and end of the shear experiment for the concentration of 5.0 gL^{-1}. Settling velocity is derived as a function of equivalent spherical diameter, with diagonal dashed lines representing effective density contours calculated using the Stokes equation (from left to right: 1600, 160, 16 (kgm^{-3})). (Top & Bottom mid) show the floc size range and mean settling velocity. (Top & Bottom right) snapshots of the videos.

D

APPENDIX D

TOWARDS IMPLEMENTATION OF FLOCCULATION IN NUMERICAL MODELS

In this appendix, the derivations given in Winterwerp, 1998 are discussed.

AGGREGATION TERM

Combining eqs. (6.21) and (6.22) leads to

$$\frac{dn}{dt} = -\frac{8}{3}\alpha G L_i^3 n^2 \tag{D.1}$$

This equation is to be compared with eq.(11) used by Winterwerp, 1998 which reads

$$\frac{dn}{dt} = -\frac{3}{2}\pi e_c e_d G L^3 n^2 \tag{D.2}$$

The parameter e_c is defined by Winterwerp as "the efficiency parameter is a function of the physicochemical properties of the sediment and water and of the organic compounds in the sediment". The efficiency parameter e_d is defined by Winterwerp as "an (efficiency) parameter for diffusion". The product $e_c e_d$ can therefore be seen as the collision efficiency

$$\alpha = e_c e_d \tag{D.3}$$

The origin of the $\frac{3}{2}\pi$ in eq.(D.2) is unknown. Combing eqs. (6.17) and (6.18) yields

$$\phi_{\text{pp in floc}} = \frac{\rho_{floc} - \rho_w}{\rho_s - \rho_w} = \frac{c/\rho_s}{nV} \tag{D.4}$$

which is to be compared with eq.(2) of (Winterwerp, 1998), which reads

$$\phi = \frac{\rho_s - \rho_w}{\rho_{floc} - \rho_w}\frac{c}{\rho_s} = f_s n L^3 \tag{D.5}$$

where Winterwerp uses $V = f_s L^3$, the shape factor f_s being equal to $\pi/6$ for spherical flocs. Note that the ϕ defined by Winterwerp corresponds to

$$\phi = \frac{\phi_s}{\phi_{\text{pp in floc}}} \tag{D.6}$$

and not to ϕ_s as he claims. Combining eqs. (6.20), (6.22) and (6.23), gives

$$\frac{dL}{dt} = \frac{2\alpha G}{D}\frac{c}{\rho_s}\frac{L^{4-D}}{L_p^{3-D}} = k_A c G L^{4-D} \tag{D.7}$$

which corresponds with eqs.(14,15) proposed by Winterwerp but for a different prefactor originating from the difference between eqs.(D.1,D.2).

D

BREAK-UP TERM

The simplest models assume that s, defined in eq. (6.26), scales with the size of particles, i.e. $p = 1$. However, in the case of fractal flocs as the ones formed by salt-induced aggregation of hard spheres, the smaller the fractal dimension, the less particle bonds per aggregate volume, the smaller the floc strength. Therefore the breakage rate should increase with decreasing fractal dimension D, which Barthelmes (Barthelmes et al., 2003) accounts for by introducing the term:

$$V_p^{1/3}\left(\frac{L}{L_p}\right)^{3/D} \tag{D.8}$$

in eq. (6.26) to yield:

$$s = s_b\left(\frac{\eta G}{\tau^*}\right)^q V_p^{1/3}\left(\frac{L}{L_p}\right)^{3/D} \tag{D.9}$$

Note that this implies that:

$$p = 3/D \tag{D.10}$$

The break-up rate given by Winterwerp by (see eqs.(16,17) in Winterwerp, 1998) is:

$$s = \frac{a}{T}\left(\frac{\eta G}{\tau^*}\right)^{q^*}\left(\frac{L - L_p}{L_p}\right)^{p^*} \tag{D.11}$$

where we substituted the turbulence induced stress $\tau_t = \eta G$ (eq.(21) in (Winterwerp, 1998)). In our notation $\tau_y = \tau^*$ is the strength of floc. The parameters a, p^* and q^* are empirical. The parameter T is defined by Winterwerp as "the time scale of the disrupting eddies" which he assumes to be $T \simeq 1/G$.

Winterwerp furthermore follows the reasoning of Kranenburg (Kranenburg, 1994) which estimates that:

$$\tau^* \simeq n_b F \tag{D.12}$$

where F is the rupture force of a bond (N) which is implicitly assumed not to depend on L and n_b is the number of bonds per unit area. Because of the self-similarity property of fractals, it follows that $n_b = m_0/L^2$ where m_0 is a constant, and hence:

$$\tau^* \simeq \frac{m_0}{L^2} F \tag{D.13}$$

The fact that τ^* then scales with L^{-2} is, therefore purely a consequence of assuming flocs to be fractal objects. The relation between floc's rupture and size has been experimentally tested, whereby a single floc is pulled apart in tensile mode (Yeung and Pelton, 1996). It has been demonstrated that the rupture depends on the fractal dimension of the floc: it is the narrowest section cross-section in a fractal object which determines its strength, which does not need to be correlated with particle size. For compact flocs (high fractal dimension), the weak points are on the periphery; therefore, these flocs are prone to experience surface erosion. For low fractal dimension flocs, on the other hand, their narrowest cross-sections can be located anywhere, and hence they tend to break in two. This latter case is in line with the initial assumption that all flocs are assumed to have the same size at all times. It follows that eq.(D.11) can be written:

$$s = aG\left(\frac{\eta G}{F}L^2\right)^{q^*}\left(\frac{L-L_p}{L_p}\right)^{p^*} \tag{D.14}$$

For situations where $L \gg L_p$ one gets:

$$s = \frac{aG^{q^*+1}}{L_p^p}\left(\frac{\eta}{F}\right)^{q^*} L_p^{2q^*+p^*} \tag{D.15}$$

Comparing eqs.(D.9,D.15), one finds the equivalence

$$\begin{aligned} q &= q^* + 1 \\ p &= 2q^* + p^* \end{aligned} \tag{D.16}$$

Winterwerp uses $p^* = 1$ and $q^* = 0.5$ which implies that $p = 2$ and $q = 1.5$. The fragmentation exponent q is usually found to be $1.5 < q < 6.5$ (Barthelmes et al., 2003) and as discussed above one usually assumes $3 \geq p \geq 1$.

From eq. (6.15) one gets:

$$\frac{1}{n}\frac{dn}{dt} = -\frac{D}{L}\frac{dL}{dt} = e_b \times s \tag{D.17}$$

which leads to:

$$\frac{dL}{dt} = -e_b \times aG\left(\frac{\eta G}{F}L^2\right)^{q^*}\left(\frac{L-L_p}{L_p}\right)^{p^*} \times \frac{L}{D} \tag{D.18}$$

$$= -k_B G^{q^*+1}\left(L-L_p\right)^{p^*} L^{2q^*+1} \tag{D.19}$$

which is to be compared with eqs.(22, 23) of Winterwerp, 1998.

REFERENCES

Abbireddy, C., & Clayton, C. (2009). A review of modern particle sizing methods. *Proc. ICE-Geotech. Eng.*, *162*, 193–201.

Agrawal, Y. C., & Pottsmith, H. C. (2000). Instruments for particle size and settling velocity observations in sediment transport. *Marine Geology*, *168*, 89–114. https://doi.org/https://doi.org/10.1016/s0025-3227(00)00044-x

Ali, W., & Chassagne, C. (2022). Comparison between two analytical models to study the flocculation of mineral clay by polyelectrolytes. *Continental Shelf Research*, *250*, 104864. https://doi.org/10.1016/j.csr.2022.104864

Ali, W., Enthoven, D., Kirichek, A., Helmons, R., & Chassagne, C. (2022a). Can flocculation reduce the dispersion of deep sea sediment plumes? *Proceedings of the World dredging conference, Copenhagen, Denmark.*, *10*, 1–9.

Ali, W., Enthoven, D., Kirichek, A., Helmons, R., & Chassagne, C. (2022b). Effect of flocculation on turbidity currents. *Frontiers in Earth Science, 10*, 2296–6463. https://doi.org/10.3389/feart.2022.1014170

Ali, W., Kirichek, A., & Chassagne, C. (2024). Settling velocity as function of cohesive sediment particle concentration. *Applied Clay Science*.

Alldredge, A. L., & Silver, M. W. (1988). Characteristics, dynamics and significance of marine snow. *Progress in Oceanography*, *20*. https://doi.org/https://doi.org/10.1016/0079-6611(88)90053-5

Aller, R. C. (1994). Bioturbation and remineralization of sedimentary organic matter: Effects of redox oscillation. https://doi.org/https://doi.org/10.1016/0009-2541(94)90062-0

Baker, M. L., Baas, J. H., Malarkey, J., Jacinto, R. S., Craig, M. J., Kane, I. A., & Barker, S. (2017). The effect of clay type on the properties of cohesive sediment gravity flows and their deposits. *Journal of Sedimentary Research*, *87*, 1176–1195. https://doi.org/10.2110/jsr.2017.63

Barthelmes, G., Pratsinis, S. E., & Buggisch, H. (2003). Particle size distributions and viscosity of suspensions undergoing shear-induced coagulation and fragmentation. *Chemical Engineering Science*, *58*, 2893–2902. https://doi.org/http://dx.doi.org/10.1016/S0009-2509(03)00133-7

Bath, A., & Greger, B. (1988). Entwicklung von manganknollenabbau- und -gewinnungsverfahren. *Schlußbericht BMFT-Projekt*.

Bergaya, F., & Gerhard, L. (2013). *Handbook of clay science* (Second). Elsevier.

Beyond-mining. (2011). *Nature Geosci*, *4*, 653–653. https://doi.org/https://doi.org/10.1038/ngeo1291

BGR Environmental Impact Assessment, B. (2019). Environmental impact assessment for the testing of a pre-protoype manganese nodule collector vehicle in the eastern

german license area (clarion-clipperton zone) in the framework of the european jpi-o miningimpact 2 research project.

Bischoff, J. L., Heath, G. R., & Leinen, M. (1979). Geochemistry of Deep-Sea Sediments from the Pacific Manganese Nodule Province: DOMES Sites A, B, and C. In J. L. Bischoff & D. Z. Piper (Eds.), *Marine geology and oceanography of the pacific manganese nodule province* (pp. 397–436). Springer US. https://doi.org/10.1007/978-1-4684-3518-4_12

Boschen, R. E., Rowden, A. A., Clark, M. R., & Gardner, J. P. A. (2013). Mining of deep-sea seafloor massive sulfides: A review of the deposits, their benthic communities, impacts from mining, regulatory frameworks and management strategies. *Ocean Coastal Management*, *84*, 54–67. https://doi.org/https://doi.org/10.1016/j.ocecoaman.2013.07.005

Chapalain, M., Verney, R., Fettweis, M., Jacquet, M., Le Berre, D., & Le Hir, P. (2019). Investigating suspended particulate matter in coastal waters using the fractal theory. *Ocean Dynamics*, *69(1)*, 59–81. https://doi.org/https://doi.org/10.1007/s10236-018-1229-6

Chassagne, C. (2020). *Introduction to colloid science: Applications to sediment characterization*. https://doi.org/https://doi.org/10.34641/mg.16

Chassagne, C. (2021). A simple model to study the flocculation of suspensions over time. *Chemical Engineering Research and Design*, *172*, 302–311. https://doi.org/https://doi.org/10.1016/j.cherd.2021.06.006

Chassagne, C., & Safar, Z. (2020). Modelling flocculation: Towards an integration in large-scale sediment transport models. *Marine Geology*, *430*. https://doi.org/https://doi.org/10.1016/j.margeo.2020.106361

Craig, M. J., Baas, J. H., Amos, K. J., Strachan, L. J., Manning, A. J., Paterson, D. M., Hope, J. A., Nodder, S. D., & Baker, M. L. (2019). Biomediation of submarine sediment gravity flow dynamics. *Geology*, *48*, 72–76. https://doi.org/10.1130/g46837.1

Danovaro, R., Snelgrove, P. V., & Tyler, P. (2014). Challenging the paradigms of deep-sea ecology. *Trends in Ecology Evolution*.

De Wit, L., Van Rhee, C., & Keetels, G. (2014). Turbulent interaction of a buoyant jet with cross-flow. *Journal of Hydraulic Engineering*, *140(12)*.

Decrop, B., & Wachter, T. D. (2019). Detailed cfd simulations for near field dispersion of deep sea mining plumes. *In Proceedings of the World dredging conference Wodcon XXII, Shanghai, China*, 116–127.

Decrop, B., De Mulder, T., Troch, P., Toorman, E., & Sas, M. (2013). Experimental investigation of negatively buoyant sediment plumes resulting from dredging operations. *CoastLab*, 573–582. https://doi.org/https://lib.ugent.be/catalog/pug01:3130474

DEME-Group. (2021). *Deme group*. https://doi.org/https://www.deme-group.com/news/metal-rich-nodules-collected-seabed-during-important-technology-trial

Deng, Z. (2022). *The role of algae in fine cohesive sediment flocculation* (Doctoral dissertation). Delft University of Technology.

Deng, Z., He, Q., Safar, Z., & Chassagne, C. (2019). The role of algae in fine sediment flocculation: In-situ and laboratory measurements. *Marine Geology*, *413*, 71–84. https://doi.org/10.1016/j.margeo.2019.02.003

Deng, Z., Huang, D., He, Q., & Chassagne, C. (2022). Review of the action of organic matter on mineral sediment flocculation. *Front. Earth Sci.* https://doi.org/10.3389/feart.2022.965919

Diercks, A., & Asper, V. (1997). In situ settling speeds of marine snow aggregates below the mixed layer: Black sea and gulf of mexico. *Deep Sea Research Part I: Oceanographic Research Papers, 44*, 385–398.

Droppo, I. G., Walling, D., & Ongley, E. (2000). The influence of floc size, density and porosity on sediment and contaminant transport. *Journal of the National Centre for Scientific Research, 4*, 141–147.

Ducklow, H., Steinberg, D., & Buesseler, K. (2001). Upper ocean carbon export and the biological pump. *Oceanography, 14*, 50–58. https://doi.org/doi:10.5670/oceanog.2001.06

Dyer, K. (1989). Sediment processes in estuaries: Future research requirements. *Journal of Geophysical Research, 94(C10)*.

Dyer, K., & Manning, A. (1999). Observation of the size, settling velocity and effective density of flocs, and their fractal dimensions. *Journal of Sea Research, 41*, 87–95. https://doi.org/https://doi.org/10.1016/S1385-1101(98)00036-7

Elerian, M. (2023). Numerical investigation of turbidity flows generated by polymetallic nodules mining. *PhD Thesis, Delft University of Technology*.

Elerian, M., Alhaddad, S., Helmons, R., & van Rhee, C. (2021). Near-field analysis of turbidity flows generated by polymetallic nodule mining tools. *Mining, 1*, 251–278. https://doi.org/10.3390/mining1030017

Elerian, M., Helmons, R., & van Rhee, C. (2022). Experimental and numerical modelling of deep-sea-mining-generated turbidity currents. *Minerals, 12*, 558. https://doi.org/10.3390/min12050558

Elimelech, M., Gregory, J., Jia, X., & Williams, R. (1995). *Particle deposition and aggregation: Measurement, modelling and simulation*. https://doi.org/https://doi.org/10.1016/C2013-0-04548-3

Enthoven, D. (2021). Plume dispersion of low-density clayey suspension turbidity currents created by deep-sea mining. *Master thesis, Delft University of Technology*.

European Commission, D.-G. f. I. M. I. E., SMEs., Bobba, S., Claudiu, P., Huygens, D., & et al. (2018). Report on critical raw materials and the circular economy. *Publications Office*. https://doi.org/https://data.europa.eu/doi/10.2873/167813

Falkowski, P. G., Scholes, R. J., Canadell, J., Canfield, D., Elster, J., Gruber, N., & et al. (2000). The global carbon cycle: A test of our knowledge of earth as a system. *Science*, 290–296. https://doi.org/doi:10.1126/science.290.5490.291

Fall, K. A., Friedrichs, C. T., Massey, G. M., Bowers, D. G., & Smith, S. J. (2021). The importance of organic content to fractal floc properties in estuarine surface waters: Insights from video, lisst, and pump sampling. *Journal of Geophysical Research: Oceans, 126*, 1–25. https://doi.org/https://doi.org/10.1029/2020jc016787

Fettweis, M. (2008). Uncertainty of excess density and settling velocity of mud flocs derived from in situ measurements. *Estuarine, Coastal and Shelf Science, 78*, 426–436. https://doi.org/https://doi.org/10.1016/j.ecss.2008.01.007

Fettweis, M., & Baeye, M. (2015). Seasonal variation in concentration, size, and settling velocity of muddy marine flocs in the benthic boundary layer. *Journal of Geophysical Research: Oceans, 120*, 5648–5667. https://doi.org/10.1002/2014jc010644

Finkel, Z. (2014). *Marine net primary production," in global environmental change, ed. b. freedman*. Springer. https://doi.org/doi:10.1007/978-94-007-5784-4

Flesch, J. C., Spicer, P. T., & Pratsinis, S. E. (1999). Laminar and turbulent shear-induced flocculation of fractal aggregates. *AIChE, 45*, 1114–1124. https://doi.org/https://doi.org/10.1002/aic.690450518

Gillard, B. (2019). *Towards deep sea mining-impact of mining activities on benthic pelagic coupling in the clarion clipperton fracture zone* (Doctoral dissertation). University of Bremen.

Gillard, B., Purkiani, K., Chatzievangelou, D., Vink, A., Iversen, M. H., & Thomsen, L. (2019). Physical and hydrodynamic properties of deep sea mining-generated, abyssal sediment plumes in the clarion clipperton fracture zone (eastern-central pacific). *Elementa: Science of the Anthropocene, 7*(1). https://doi.org/10.1525/elementa.343

Gillard, B., & Thomsen, L. (2019). Characterization of sediment plumes behind mining vehicles in the nori area (laboratory analyses). *iSeaMC*.

Global Sea Mineral Resources NV, G. (2018). *Environmental impact statement smallscale testing of nodule collector components on the seafloor of the clarion-clipperton fracture zone and its environmental impact* (tech. rep.).

Glover, A. G., & Smith, C. R. (2003). The deep-sea floor ecosystem: Current status and prospects of anthropogenic change by the year 2025. *Environmental Conservation, 30*(3), 219–241.

Gollner, S., Kaiser, S., Menzel, L., Jones, D. O., Brown, A., Mestre, N. C., van Oevelen, D., Menot, L., Colaço, A., Canals, M., Cuvelier, D., Durden, J. M., Gebruk, A., Egho, G. A., Haeckel, M., Marcon, Y., Mevenkamp, L., Morato, T., Pham, C. K., ... Martinez Arbizu, P. (2017). Resilience of benthic deep-sea fauna to mining activities. *Marine environmental research, 129*, 76–101. https://doi.org/10.1016/j.marenvres.2017.04.010

Govoreanu, R., Saveyn, H., Van der Meeren, P., Nopens, I., & Vanrolleghem, P. A. (2009). A methodological approach for direct quantification of the activated sludge floc size distribution by using different techniques. *Water Science and Technology, 60(7)*, 1857–1867. https://doi.org/10.1016/j.marenvres.2017.04.010

Gratiot, N., & Manning, A. (2004). An experimental investigation of floc characteristics in a diffusive turbulent flow. *Journal of Coastal Research, 41*.

Green-car-congress. (2021).

Gregory, J., & O'Melia, C. R. (1989). Fundamentals of flocculation. *Critical Reviews in Environmental Control, 19(3)*. https://doi.org/DOI:10.1080/10643388909388365

Grunsven, F., Keetels, G., & Rhee, C. (2018). The initial spreading of turbidity plumes – dedicatedlaboratory experiments for model validation. *Deep-Sea Mining: Challenges of Going Further and DeeperAdvances in Marine Research and Subsea Technology Beyond Oil and Gas UMC Grieghallen, Bergen, Norway*.

Guazzelli, E., & Morris, J. F. (2011). *A physical introduction to suspension dynamics: Cambridge university press* (Vol. 45).

Guo, C., Manning, A. J., Bass, S., Guo, L., & He, Q. (2021). A quantitative lab examination of floc fractal property considering influences of turbulence, salinity and sediment concentration. *Journal of Hydrology*, *601*. https://doi.org/https://doi.org/10.1016/j.jhydrol.2021.126574

Haalboom, S., de Stigter, H., Mohn, C., Vandorpe, T., Smit, M., de Jonge, L., & Reichart, G.-J. (2023). Monitoring of a sediment plume produced by a deep-sea mining test in shallow water, málaga bight, alboran sea (southwestern mediterranean sea). *Marine Geology*, *456*. https://doi.org/https://doi.org/10.1016/j.margeo.2022.106971

Haalboom, S., Schoening, T., Urban, P., Gazis, I. Z., de Stigter, H., Gillard, B., Baeye, M., Martina, H., Kaveh, P., Gert Jan, R., Thomsen, L., Haeckel, M., Vink, A., & Greinert, J. (2022). Monitoring of anthropogenic sediment plumes in the clarion clipperton zone, ne equatorial pacific ocean. *Frontiers in Marine Science*, *9*, 76–101. https://doi.org/10.3389/fmars.2022.882155

Hage, S., Cartigny, M. J., Sumner, E. J., Clare, M. A., Clarke, J. E. H., Talling, P. J., Lintern, D. G., Simmons, S. M., Jacinto, R. S., Vellinga, A. J., Allin, J. R., Azpiroz-Zabala, M., Gales, J. A., Hizzett, J. L., Hunt, J. E., Mozzato, A., Parsons, D. R., Pope, E. L., Stacey, C. D., … Watts, C. (2019). Direct monitoring reveals initiation of turbidity currents from extremely dilute river plumes. *Geophysical research letters*, *46*, 11310–11320. https://doi.org/10.1029/2019gl084526

Hallworth, M., Hogg, A., & Huppert, H. (1998). Effects of external flow on compositional and particle gravity currents. *J. Fluid Mech.*, *359*, 109–142.

Hallworth, M., & Huppert, H. (1998). Abrupt transitions in high-concentration, particle driven gravity currents. *Physics of Fluids*, *10*, 1083–1087.

Harbour, R. P., Leitner, A. B., Ruehlemann, C., Vink, A., & K., S. A. (2020). Benthic and demersal scavenger biodiversity in the eastern end of the clarion-clipperton zone – an area marked for polymetallic nodule mining. *Frontiers in Marine Science*, *7*. https://doi.org/10.3389/fmars.2020.00458

Hein, J. R., & Koschinsky, A. (2014). Deep-ocean ferromanganese crusts and nodules. *Elsevier*, *13*, 273–291. https://doi.org/10.1016/B978-0-08-095975-7.01111-6

Hein, J. R., Koschinsky, A., & Kuhn, T. (2020). Deep-ocean polymetallic nodules as a resource for critical materials. *Nature Reviews Earth Environment*, *1*(3), 158–169. https://doi.org/10.1038/s43017-020-0027-0

Hein, J. R., & Petersen, S. (2013). The geology of cobalt–rich ferromanganese crusts. *In: Deep Sea Minerals: Cobalt-rich Ferromanganese Crusts: A physical, biological, environmental, and technical review: 1c. ; 1c , ed. by Baker, E. and Beaudoin, Y.. Secretariat of the Pacific Community (SPC), Noumea, New Caledonia*, (978-82-7701-119-6), 7–14.

Helmons, R., de Wit, L., de Stigter, H., & Spearman, J. (2022). Dispersion of Benthic Plumes in Deep-Sea Mining: What Lessons Can Be Learned From Dredging? *Frontiers in Earth Science*, *10*. https://doi.org/10.3389/feart.2022.868701

Herring, P. (2001). *The biology of the deep ocean*.

Ho, Q. N., Fettweis, M., Spencer, K. L., & Lee, B. J. (2022). Flocculation with heterogeneous composition in water environments: A review. *Water Research*, (213). https://doi.org/https://doi.org/10.1016/j.watres.2022.118147

Huppert, H. E. (2006). Gravity currents: A personal perspective. *Journal of Fluid Mechanics*, *554*(1), 299–322. https://doi.org/10.1017/s002211200600930x

ISA. (2015). *A geological model of polymetallic nodule deposits in the clarionclipperton fracture Zone* (tech. rep.).

ISA. (2019). *Current status of the reserved areas with the international seabed authority* (tech. rep.).

Iversen, M. H., & Ploug, H. (2010). Ballast minerals and the sinking carbon flux in the ocean: Carbon-specific respiration rates and sinking velocity of marine snow aggregates. *Biogeosciences*, *7*, 2613–2624. https://doi.org/doi:10.5194/bg-7-2613-2010

Jarvis, P., Jefferson, B., & Parsons, S. (2005). Measuring floc structural characteristics. *Reviews in Environmental Science and Biotechnology*, *4*.

Jones, D. O. B., Kaiser, S., Sweetman, A. K., Smith, C. R., Menot, L., Vink, A., Trueblood, D., Greinert, J., Billett, D. S. M., Arbizu, P. M., Radziejewska, T., Singh, R., Ingole, B., Stratmann, T., Simon Lledo, E., Durden, J. M., & Clark, M. R. (2017). Biological responses to disturbance from simulated deep-sea polymetallic nodule mining. *PloS one*, *12*, 1–26. https://doi.org/10.1371/journal.pone.0171750

Jones, D. O., Simon-Lledo, E., Amon, D. J., Bett, B. J., Caulle, C., Clement, L., Connelly, D. P., Dahlgren, T. G., Durden, J. M., Drazen, J. C., Felden, J., Gates, A. R., Georgieva, M. N., Glover, A. G., Gooday, A. J., Hollingsworth, A. L., Horton, T., James, R. H., Jeffreys, R. M., … Huvenne, V. A. (2021). Environment, ecology, and potential effectiveness of an area protected from deep-sea mining (clarion clipperton zone, abyssal pacific). *Progress in Oceanography*, *197*. https://doi.org/10.1016/j.pocean.2021.102653

Kaikkonen, L., Venesjärvi, R., Nygård, H., & Kuikka, S. (2018). Assessing the impacts of seabed mineral extraction in the deep sea and coastal marine environments: Current methods and recommendations for environmental risk assessment. *Marine pollution bulletin*, *135*, 1183–1197.

Kaiser, S., R. Smith, C., & Martinez Arbizu, P. (2013). Editorial: Biodiversity of the clarion clipperton fracture zone. *Marine Biodiversity*, *47*, 259–264. https://doi.org/doi:10.1007/s12526-017-0733-0

Kanzog, C., Ramette, A., Quéric, N. V., & Klages, M. (2009). Response of benthic microbial communities to chitin enrichment: An in situ study in the deep arctic ocean. *Polar Biol*, *32*, 105–112. https://doi.org/https://doi.org/10.1007/s00300-008-0510-4

Karageorgis, A., Georgopoulos, D., Gardner, W., Mikkelsen, O., & Velaoras, D. (2015). How schlieren affects beam transmissometers and lisst-deep: An example from the stratified danube river delta, nw black sea. *Mediterranean Marine Science*, *16*, 366–372. https://doi.org/https://doi.org/10.12681/mms.1116

Khelifa, A., & Hill, P. S. (2006). Models for effective density and settling velocity of flocs. *Journal of Hydraulic Research*, 390–401. https://doi.org/https://doi.org/10.1080/00221686.2006.9521690

Kim, S., Moon, B., & Lee, H. (2001). Effects of ph and dosage on pollutant removal and floc structure during coagulation. *Microchemical Journal*, 197–203.

Kiørboe, T. (2001). Formation and fate of marine snow: Small-scaleprocesses with large-scale implications. *SCIENTIA MARINA*, *57*, 57–71.

Klimpel, R. C., & Hogg, R. (1986). Effects of flocculation conditions on agglomerate structure. *Journal of colloid and interface science, 113(1)*, 121–131.

Konstantin, M., Mogollon, J. M., Picard, A., Ruhlemann, C., Kuhn, T., Nothen, K., & Kasten, S. (2014). Impact of depositional and biogeochemical processes on small scale variations in nodule abundance in the clarion-clipperton fracture zone. *Deep Sea Research Part I: Oceanographic Research Papers, 91*, 125–141. https://doi.org/10.1016/j.dsr.2014.06.001

Kranck, K. (1973). Flocculation of suspended sediment in the sea. *Nature*, 348–350. https://doi.org/https://doi.org/10.1038/246348a0

Kranenburg, C. (1994). The fractal structure of cohesive sediment aggregates. *Estuarine, Coastal and Shelf Science*, 451–460. https://doi.org/https://doi.org/10.1016/S0272-7714(06)80002-8

Kuhn, T. (2015). Low-temperature fluid circulation at seamounts and hydrothermal pits: Heat flow regime, impact on biogeochemical processes and its potential influence on the occurrence and composition of manganese nodules in the ne pacific. *Cruise Report*. https://doi.org/https://doi.org/10.2312/cr_so240

Kuhn, T., Wegorzewski, A., & Vink, A. (2017). Composition, formation, and occurrence of polymetallic nodules. *Deep-Sea Mining: Resource Potential, Technical and Environmental Considerations*, 1–535. https://doi.org/doi:10.1007/978-3-319-52557-0.

Kusters, K. (1991). *The influence of turbulence on aggregation of small particles in agitated vessels* (Doctoral dissertation). Eindhoven University of Technology.

Lang, M. A., Dasselaar, S., Aasly, K., & Larsen, E. (2019). Blue nodules deliverable report d3.4 report describing the process flow overview pu, 1–23.

Langmuir, I. (1918). The adsorption of gases on plane surface of glass, mica and platinum. *Journal of the American Chemical Society*, 1361–1402. https://doi.org/https://doi.org/10.1021/ja02242a004

Law, D. J., Bale, A. J., & Jones, S. E. (1997). Adaptation of focused beam reflectance measurement to in-situ particle sizing in estuaries and coastal waters. *Marine Geology, 140*, 47–59.

Le Quere, C., Andrew, R., Friedlingstein, P., Sitch, S., Hauck, J., Pongratz, J., & et al. (2018). Global carbon budget. *Earth Syst. Sci. Data*, 2141–2194. https://doi.org/doi:10.5194/essd-10-2141-2018

Lee, B. J., Kim, J., Hur, J., Choi, I. H., Toorman, E., Fettweis, M., & Choi, J. W. (2019). Seasonal dynamics of organic matter composition and its effects on suspended sediment flocculation in river water. *Water Resources Research, 55*, 6968–6985. https://doi.org/https://doi.org/10.1029/2018WR024486

Lesser, G., Roelvink, J., Van Kester, J., & Stelling, G. (2004). Development and validation of a three-dimensional morphological model. *Coastal engineering*, 883–915. https://doi.org/https://doi.org/10.1016/j.coastaleng.2004.07.014

Li, M., Wilkinson, D., & Patchigolla, K. (2005). Comparison of particle size distributions measured using different techniques. *Particulate Science and Technology, 23*. https://doi.org/https://doi.org/10.1080/02726350590955912

Liang, L., Peng, Y., Tan, J., & Xie, G. (2015). A review of the modern characterization techniques for flocs in mineral processing. *Minerals Engineering, 84*. https://doi.org/https://doi.org/10.1016/j.mineng.2015.10.011.

Lutz, M., Dunbar, R., & Caldeira, K. (2002). Regional variability in the vertical flux of particulate organic carbon in the ocean interior. *Global Biogeochem. Cycles, 16(3)*. https://doi.org/doi:10.1029/2000gb001383

Lyle, M. (2015). Deep-sea sediments. in: Harff, j., meschede, m., petersen, s., thiede, j. (eds) encyclopedia of marine geosciences. *Springer*.

MacIver, M. (2019). Safas: Sedimentation and floc analysis software. https://github.com/rmaciver/safas

Maggi, F. (2013). The settling velocity of mineral, biomineral, and biological particles and aggregates in water. *Journal of Geophysical Research: Oceans*, 2118–2132. https://doi.org/https://doi.org/10.1002/jgrc.20086

Malarkey, J., Baas, J. H., Hope, J. A., Aspden, R. J., Parsons, D. R., Peakall, J., Paterson, D. M., Schindler, R. J., Ye, L., Lichtman, I. D., Bass, S. J., Davies, A. G., Manning, A. J., & Thorne, P. D. (2015). The pervasive role of biological cohesion in bedform development. *Nature Communications, 6*, 6257. https://doi.org/10.1038/ncomms7257

Manning, A. J. (2004). A comparison of floc properties observed during neap and spring tidal conditions. *In: Ciavola, P., Collins, M. B. (eds.), Sediment Transport in European Estuaries, Journal of Coastal Research*, 90–104. https://doi.org/https://doi.org/10.1016/S1568-2692(02)80019-5

Manning, A. J. (2015). *LabSFLOC-2 the second generation of the laboratory system to determine spectral characteristics of flocculating cohesive and mixed sediments HR Wallingford Report* (tech. rep.).

Manning, A. J., Bass, S., & Dyer, K. (2006). Floc properties in the turbidity maximum of a mesotidal estuary during neap and spring tidal conditions. *Marine Geology, 235*(1-4), 193–211. https://doi.org/https://doi.org/10.1016/j.margeo.2006.10.014

Manning, A. J., Baugh, J. V., Soulsby, R. L., R., S. J., & Whitehouse, R. J. S. (2011). Cohesive sediment flocculation and the application to settling flux modelling. *In: Ginsberg, S.S. (ed.) Sediment Transport. Rijeka, Croatia: InTech.*

Manning, A. J., Baugh, J., Spearman, J., & Whitehouse. (2010). Flocculation settling characteristics of mud: Sand mixtures. *Ocean Dynamics*, 237–253. https://doi.org/https://doi.org/10.1007/s10236-009-0251-0

Manning, A. J., & Dyer, K. (1999). A laboratory examination of floc characteristics with regard to turbulent shearing. *Marine Geology*, 147–170. https://doi.org/https://doi.org/10.1016/S0025-3227(99)00013-4

Manning, A. J., & Dyer, K. (2002). A comparison of floc properties observed during neap and spring tidal conditions. *Proceedings in Marine Science*, 233–250. https://doi.org/https://doi.org/10.1016/S1568-2692(02)80019-5

Manning, A. J., & Dyer, K. (2007). Mass settling flux of fine sediments in northern european estuaries: Measurements and predictions. *Marine Geology*, 107–122. https://doi.org/https://doi.org/10.1016/j.margeo.2007.07.005

Manning, A. J., Friend, P., Prowse, N., & Amos, C. L. (2007). Estuarine mud flocculation properties determined using an annular mini-flume and the labsfloc system.

Continental Shelf Research, *27*(8), 1080–1095. https://doi.org/10.1016/j.csr.2006.04.011

Manning, A. J., Whitehouse, R., & Uncles, R. (2017). Suspended particulate matter: The measurement of flocs.

Many, G., Bourrin, F., de Madron, X. D., Pairaud, I., Gangloff, A., Doxaran, D., Ody, A., Verney, C., R. Menniti, Le Berre, D., & Jacquet, M. (2016). Particle assemblage characterization in the rhone river rofi. *Journal of Marine Systems*, *157*, 39–51. https://doi.org/https://doi.org/10.1016/j.jmarsys.2015.12.010

McCave, I. N. (1984). Size spectra and aggregation of suspended particles in the deep ocean. *Deep Sea Research Part A: Oceanographic Research Papers*, *31*, 329–352. https://doi.org/https://doi.org/10.1016/0198-0149(84)90088-8

McDowell, D. N., & O'Connor, B. A. (1977). Hydraulic behaviour of estuaries. *London: MacMillan*.

Mehta, A. (2013). *An introduction to hydraulics of fine sediment transport*. WORLD SCIENTIFIC. https://doi.org/10.1142/8708

Mietta, F. (2010). *Evolution of the floc size distribution of cohesive sediments* (Doctoral dissertation).

Mietta, F., Chassagne, C., Manning, A. J., & Winterwerp, J. C. (2009). Influence of shear rate, organic matter content, ph and salinity on mud flocculation. *Ocean Dynamics*, *59*, 751–763. https://doi.org/10.1007/s10236-009-0231-4

Mikkelsen, O. A., Hill, P. S., Milligan, T. G., & Chant, R. J. (2005). In situ particle size distributions and volume concentrations from a lisst-100 laser particle sizer and a digital floc camera. *Continental Shelf Research*, *25*, 1959–1978. https://doi.org/https://doi.org/10.1016/j.csr.2005.07.001

Miller, K., Brigden, K., Currie, D., Johnston, P., & Thompson, K. F. (2021). Challenging the need for deep seabed mining from the perspective of metal demand, biodiversity, ecosystems services, and benefit sharing. *Front. Mar. Sci.*, *1040*. https://doi.org/https://doi.org/10.3389/fmars.2021.706161

Miller, K., Thompson, K. F., Johnston, P., & Santillo, D. (2018). An overview of seabed mining including the current state of development, environmental impacts, and knowledge gaps. *Front. Mar. Sci.*, *4*. https://doi.org/https://doi.org/10.3389/fmars.2017.00418

Morgan, L., Odunton, N., & Charles, A. (1999). Synthesis of environmental impacts of deep seabed mining. *Marine Georesources and Geotechnology*, *17*(4), 307–356.

Munoz-Royo, C., Ouillon, R., El Mousadik, S., Alford, M. H., & Peacock, T. (2022). An in situ study of abyssal turbidity-current sediment plumes generated by a deep seabed polymetallic nodule mining preprototype collector vehicle. *Science Advances*, *8*. https://doi.org/DOI:10.1126/sciadv.abn1219

Nauru Ocean Resources Inc, N. (2021). *Collector test study: Environmental impact statement. nauru ocean resources inc.* (tech. rep.).

Newell, R. C., Seiderer, L. J., & Hitchcock, D. R. (1998). The impact of dredging works in coastal waters: A review of the sensitivity to disturbance and subsequent recovery of biological resources on the sea bed. *Oceanography and Marine Biology: an annual review*, *36(1)*, 127–178.

Nodules, B. (2020). *Environmental impact assessment (eia) components for test mining up to prototype level (trl 6)* (tech. rep.).

Nogueira, H. I. S., Adduce, C., Alves, E., & Franca, M. J. (2013). Analysis of lock-exchange gravity currents over smooth and rough beds. *Journal of Hydraulic Research*, *51*(4), 417–431. https://doi.org/10.1080/00221686.2013.798363

Normant, C. (2000). Three-dimensional modelling of cohesive sediment transport in the loire estuary. *Hydrological processes*, *14*, 2231–2243. https://doi.org/https://doi.org/10.1002/1099-1085(200009)14

Oebius, H. U., Becker, H. J., Rolinski, S., & Jankowski, J. A. (2001). Parametrization and evaluation of marine environmental impacts produced by deep-sea manganese nodule mining. *Deep. Res. Part II Top. Stud. Oceanogr.*, *48*, 3453–3467. https://doi.org/doi:10.1016/S0967-0645(01)00052-2

Ouillon, R., Kakoutas, C., Meiburg, E., & Peacock, T. (2021). Gravity currents from moving sources. *Journal of Fluid Mechanics*, *924*, 638–704. https://doi.org/10.1017/jfm.2021.654

Ozturgut, E., Lavelle, J. W., & Burns, R. E. (1981). Chapter 15 impacts of manganese nodule mining on the environment: Results from pilot-scale mining tests in the north equatorial pacific. *Elsevier Oceanogr.*, *27*, 437–474. https://doi.org/doi:10.1016/S0422-9894(08)71420-X.

Parzanini, C., Parrish, C., Hamel, J., & Mercier, A. (2018). Functional diversity and nutritional content in a deep-sea faunal assemblage through total lipid, lipid class, and fatty acid analyses. *PLOS ONE*, (13(11)). https://doi.org/https://doi.org/10.1371/journal.pone.0207395

Passow, U., & Carlson, C. A. (2012). The biological pump in a high co2 world. *Mar. Ecol. Prog. Ser.*, *470*, 249–271. https://doi.org/doi:10.3354/meps09985

Peacock, T., & Alford, M. (2018). Is deep-sea mining worth it? *Science AM*, 72–77. https://doi.org/https://doi.org/10.1038/scientificamerican0518-72

Peacock, T., & Ouillon, R. (2023). The fluid mechanics of deep-sea mining. *Annual Review of Fluid Mechanics*, *55*, 403–430. https://doi.org/https://doi.org/10.1146/annurev-fluid-031822-010257

Pennekamp, J. G. S., & Quaak, M. P. (1990). Impact on the environment of turbidity caused by dredging. *Terra et Aqua*, *42(1)*, 0-20.

Petersen, S., Kratschell, A., Augustin, N., Jamieson, J., Hein, J., & Hannington, M. (2016). News from the seabed–geological characteristics and resource potential of deep-sea mineral resources. *Marine Policy*, *70*, 175–187. https://doi.org/https://doi.org/10.1016/j.marpol.2016.03.012

Ragonnaud, G. (2023). Securing europe's supply of critical raw materials: The material nature of the eu's strategic goals. *Members Research Service*.

Ramirez-Llodra, E., Tyler, P., Baker, M., O.A., B., Clark, M., Escobar, E., & et al. (2011). Man and the last great wilderness: Human impact on the deep sea. *PLoS ONE*, *6*. https://doi.org/https://doi.org/10.1371/journal.pone.0022588

Ransom, B., Shea, K., Burkett, P., Bennett, R., & Baerwald, R. (1998). Comparison of pelagic and nephloid layer marine snow: Implications for carbon cycling. *Marine Geology*, *150*, 39–50. https://doi.org/https://doi.org/10.1371/journal.pone.0022588

Russel, W. B., Saville, D. A., & Schowalter, W. R. (1989). *Colloidal dispersions*. Cambridge university press. https://doi.org/https://doi.org/10.1017/CBO9780511608810

Rutkowska, M., Dubalska, K., Bajger-Nowak, G., Konieczka, P., & Namieśnik, J. (2014). Organomercury compounds in environmental samples: Emission sources, toxicity, environmental fate, and determination. *Critical Reviews in Environmental Science and Technology*, *44*, 638–704. https://doi.org/10.1080/10643389.2012.728825

Rzeznik, A. J., Flierl, G. R., & Peacock, T. (2019). Model investigations of discharge plumes generated by deep-sea nodule mining operations. *Ocean Engineering*, *172*, 684–696. https://doi.org/http://dx.doi.org/10.1016/j.oceaneng.2018.12.012

Safar, Z., Rijnsburger, S., Sanz, M., Chassagne, C., Manning, A., Pietrzak, J., Souza, A., van Kessel, T., Horner-Devine, A., Flores, R., & McKeon, M. (2019). Characterization and dynamics of suspended particulate matter in the near field of the rhine river plume during a neap tide. *In Geophysical Research Abstracts*, *21*.

Safar, Z. (2022). Suspended particulate matter formation and accumulation in the delta: From monitoring to modelling. *PhD Thesis, Delft University of Technology*.

Safar, Z., Deng, Z., & Chassagne, C. (2023). Applying a logistic growth equation to model flocculation of sediment in the presence of living and dead organic matter. *Front. Mar. Sci.*

Sanz, M. (2018). *Flocculation and consolidation of cohesive sediments under the influence of coagulant and flocculant* (Doctoral dissertation). Delft University of Technology.

Shakeel, A., MacIver, M. R., van Kan, P., Kirichek, A., & Chassagne, C. (2021). A rheological and microstructural study of two-step yielding in mud samples from a port area. *Colloids and Surfaces A: Physicochemical and Engineering Aspects*, *624*. https://doi.org/10.1016/j.colsurfa.2021.126827

Shakeel, A., Safar, Z., Ibanez, M., van Paassen, L., & Chassagne, C. (2020). Flocculation of clay suspensions by anionic and cationic polyelectrolytes : A systematic analysis. *Minerals*, *10*, 1–24. https://doi.org/10.3390/min10110999

Sharma, R. (2015). Environmental issues of deep-sea mining. *Procedia Earth and Planetary Science*, *11*, 204–211. https://doi.org/10.1016/j.proeps.2015.06.026

Sharma, R. (2017). Deep-sea mining. cham, switz. *Springer Int.*

Sharma, R., Nagender, B., Parthiban, N. G., & Sankar, S. J. (2001). Sediment redistribution during simulated benthic disturbance and its implications on deep seabed mining. *Deep Sea Research Part II: Topical Studies in Oceanography*, *48*, 3363–3380. https://doi.org/http://dx.doi.org/10.1016/S0967-0645(01)00046-7

Shen, X., Lee, B. J., Fettweis, M., & Toorman, E. A. (2018). A tri-modal flocculation model coupled with telemac for estuarine muds both in the laboratory and in the field. *Water research*, *145*, 473–486. https://doi.org/https://doi.org/10.1016/j.watres.2018.08.062

Skinnebach, K. H., Fruergaard, M., & Andersen, T. J. (2019). Biological effects on flocculation of fine-grained suspended sediment in natural seawater. *Estuarine, Coastal and Shelf Science*, *228*.

Smith, S. J., & Friedrichs, C. T. (2011). Size and settling velocities of cohesive flocs and suspended sediment aggregates in a trailing suction hopper dredge plume. *Continental Shelf Research*, *31*(10), 50–63. https://doi.org/10.1016/j.csr.2010.04.002

Smith, S. J., Tunnicliffe, V., Colaço, A., Drazen, J., S., G., & et al. (2020). Deep-sea misconceptions cause underestimation of seabed-mining impacts. *Trends in Ecology Evolution*, *35*(10), 853–857. https://doi.org/http://dx.doi.org/10.1016/j.tree.2020.07.002

Soulsby, R., Manning, A. J., Spearman, J., & Whitehouse, R. (2013). Settling velocity and mass settling flux of flocculated estuarine sediments. *Marine Geology*, *339*(10), 1–12. https://doi.org/https://doi.org/10.1016/j.margeo.2013.04.006

Spearman, J., Crossouard, J., N., T., Cooper, A., Turnbull, M., Manning, A. J., Lee, M., & Murton, B. J. (2020). Measurement and modelling of deep sea sediment plumes and implications for deep sea mining. *10*(1), 5075. https://doi.org/10.1038/s41598-020-61837-y

Spearman, J., Manning, A. J., & Whitehouse, R. (2011). The settling dynamics of flocculating mud sand mixtures part 2 numerical modelling. *Ocean Dynamics*, *61*, 351–370. https://doi.org/https://doi.org/10.1007/s10236-011-0385-8

Spearman, J., Taylor, J., Crossouard, N., Cooper, A., Turnbull, M., Manning, A. J., & Lee, M. (2019). The measurement and modelling of plumes resulting from deep sea mining of fe-mn crusts. *In Proceedings of the World dredging conference (WODCONXXII), Shanghai, China*.

Spencer, K., Manning, A., Droppo, I., Leppard, G., & Benson, T. (2011). Dynamic interactions between cohesive sediment tracers and natural mud. *Journal of Soils and Sediments*, *10*, 1401–1414. https://doi.org/https://doi.org/10.1007/s11368-010-0291-6

Spencer, K., Wheatland, J., Carr, S., Manning, A., Bushby, A., Gu, C., Botto, L., & Lawrence, T. (2022). Quantification of 3 dimensional structure and properties of flocculated natural suspended sediment. *Water Research*, *222*. https://doi.org/https://doi.org/10.1016/j.watres.2022.118835

Spicer, P., & Pratsinis, S. (1996). Coagulation and fragmentation: Universal steady state particle size distribution. *AIChE*, *42*, 1612–1620. https://doi.org/https://doi.org/10.1002/aic.690420612

Stemmann, L., Jackson, G. A., & Ianson, D. (2004). A vertical model of particle size distributions and fluxes in the midwater column that includes biological and physical processes. *Part I: Model formulation*. https://doi.org/https://doi.org/10.1002/aic.690420612

Sweetman, A. K., Smith, C. R., Shulse, C. N., Maillot, B., Lindh, M., & Church, M. J. e. a. (2019). Key role of bacteria in the short-term cycling of carbon at the abyssal seafloor in a low particulate organic carbon flux region of the eastern pacific ocean. *Ocean. Limnol. Oceanogr.*, *64*, 694–713. https://doi.org/https://doi.org/10.1002/lno.11069

Thiel, H. (1992). Deep-sea environmental disturbance and recovery potential. *Internationale Revue der gesamten Hydrobiologie und Hydrographie*, *77*(2), 331–339.

Thiel, H. (2003). Anthropogenic impacts on the deep sea. *Ecosystems of the World*, 427–472.

Thistle, D. (2003). *The deep-sea floor: An overview*.

Turner, J. (2015). Zooplankton fecal pellets, marine snow, phytodetritus and the ocean's biological pump. *Prog. Oceanogr., 130*, 205–248. https://doi.org/doi:10.1016/j.pocean.2014.08.005

Tyler, P. (2003). *Ecosystems of the deep oceans*.

Van Leussen, W. (1988). Aggregation of particles, settling velocity of mud flocs a review. *In Dronkers van Leussen (eds) Physical Processes in Estuaries, Springer, Berlin, Heidelberg*. https://doi.org/https://doi.org/10.1007/978-3-642-73691-9_19

Van Leussen, W. (1999). The variability of settling velocities of suspended fine-grained sediment in the ems estuary. *Journal of Sea Research*. https://doi.org/https://doi.org/10.1016/S1385-1101(98)00046-X

Van Reusel, A., Hilario, A., Ribeiro, P. A., Menot, L., & Arbizu, P. M. (2016). Threatened by mining, polymetallic nodules are required to preserve abyssal epifauna. *Scientific reports*, *6*, 26808. https://doi.org/10.1038/srep26808

Varriale, A. C., Crema, R., Galletti, M. C., & Zunarelli, R. V. (1985). Environmental impact of extensive dredging in a coastal marine area. *Marine Pollution Bulletin*, *16(12)*, 483–488.

Verney, R., Lafite, R., Brun Cottan, J. C., & Le Hir, P. (2011). Behaviour of a floc population during a tidal cycle: Laboratory experiments and numerical modelling. *Continental Shelf Research*, *31*. https://doi.org/https://doi.org/10.1016/j.csr.2010.02.005

Volz, J. B., Mogollon, J. M., Geibert, W., Arbizu, P. M., Koschinsky, A., & Kasten, S. (2018). Natural spatial variability of depositional conditions, biogeochemical processes and element fluxes in sediments of the eastern clarion-clipperton zone, pacific ocean. *Deep Sea Research Part I: Oceanographic Research Papers*, *140*, 159–172. https://doi.org/10.1016/j.dsr.2018.08.006

Weaver, P., Aguzzi, J., Boschen Rose, R., Colaco, A., de Stigter, H., Gollner, S., Haeckel, M., Hauton, C., Helmons, R., Jones, D., Lily, H., Mestre, N., Mohn, C., & Thomsen, L. (2022). Assessing plume impacts caused by polymetallic nodule mining vehicles. *Marine Policy*, *139*, 105011. https://doi.org/10.1016/j.marpol.2022.105011

Wedding, L. M., Reiter, S. M., Smith, C. R., Gjerde, K. M., Kittinger, J. N., Friedlander, A. M., Gaines, S. D., Clark, M. R., Thurnherr, A. M., Hardy, S. M., & Crowder, L. B. (2015). Managing mining of the deep seabed. *Science*, *345*, 144–145. https://doi.org/https://doi.org/10.1126/science.aac6647

Winterwerp, J. C. (1998). A simple model for turbulence induced flocculation of cohesive sediment. *Journal of hydraulic research*, *36*, 309–326. https://doi.org/https://doi.org/10.1080/00221689809498621

WOR. (2014). *Mineral resources: Wor 3 marine resources opportunities and risks* (tech. rep.).

Xu, R., & Guida, O. A. D. (2003). Comparison of sizing small particles using different technologies. *Powder Technology*, *132*. https://doi.org/https://doi.org/10.1016/S0032-5910(03)00048-2

Ye, L., Manning, A. J., & Hsu, T.-J. (2020). Corrigendum to "oil-mineral flocculation and settling velocity in saline water" [water research, 173(2020), 115569]. *Water research*, *184*. https://doi.org/10.1016/j.watres.2020.116180

Yeo, I. A., Howarth, S., Spearman, J., Cooper, A., Crossouard, N., Taylor, J., Turnbull, M., & Murton, B. (2019). Distribution of and hydrographic controls on ferromanganese crusts: Tropic seamount, atlantic. *Ore Geology Reviews, 114*. https://doi.org/https://doi.org/10.1016/j.oregeorev.2019.103131

Yeung, A., & Pelton, R. (1996). Micromechanics: A new approach to studying the strength and breakup of flocs. *Journal of Colloid and Interface Science, 184*, 579–585. https://doi.org/https://doi.org/10.1006/jcis.1996.0654

Zawadzki, D., Macicag, L., Abramowski, T., & McCartney, K. (2020). Fractionation trends and variability of rare earth elements and selected critical metals in pelagic sediment from abyssal basin of ne pacific (clarion-clipperton fracture zone). *Minerals, 10*. https://doi.org/10.3390/min10040320

Zhao, L., Boufadel, M. C., King, T., Robinson, B., Conmy, R., & Lee, K. (2018). Impact of particle concentration and out-of-range sizes on the measurements of the lisst. *Measurement Science and Technology, 29*(5), 055302.

Zhou, Y., & Franks, G. V. (2006). Flocculation mechanism induced by cationic polymers investigated by light scattering. *Langmuir, 22*. https://doi.org/https://doi.org/10.1021/la060281+

ACKNOWLEDGEMENTS

Amidst the upheaval of a global pandemic, I embarked on a journey that would lead me to unexpected twists and turns, culminating in a doctorate from the esteemed Delft University of Technology. In Winston Churchill's words, "Success is not final, failure is not fatal: it is the courage to continue that counts," echoed in my heart, propelling me forward through the ups and downs of my academic pursuit.

With my sights set on a PhD at Queensland University of Technology, Brisbane, Australia, I eagerly prepared to embark on this new chapter. However, the unexpected arrival of COVID-19 threw my plans into disarray, delaying my visa application and casting a shadow of uncertainty over my future.

Undeterred, I decided to explore other options and applied for PhD programs in France, Norway, and, yes, the Netherlands. When offers from multiple universities arrived, I was torn between excitement and confusion. While the opportunity to pursue my research interests abroad was enticing, the positive connection I had forged with my potential supervisor, Claire, at TU Delft held me back.

I sought advice from my close friends, who encouraged me to stay and chase my dreams in the Netherlands. As I contemplated my decision, a new twist emerged: funding for my proposed project at TU Delft was placed on hold due to COVID-related concerns. Uncertainty clouded my path once again, and I found myself questioning my choice of TU Delft.

Meanwhile, a PhD offer from Stavanger University in Norway, a place I liked, beckoned me. Despite the allure of Norway, Claire's unwavering belief in my potential and her confidence in the project's funding swayed me to stay the course. Her support proved pivotal, and as fate would have it, the funding for the project was secured, paving the way for my journey to TU Delft.

My decision to persevere, fueled by Claire's encouragement and Winston Churchill's inspiring words, has led me to this remarkable milestone. The path to a doctorate has been filled with unexpected challenges and unforeseen detours, but it is the courage to continue, the unwavering belief in one's dreams, and the support of those who believe in us that ultimately shape our destinies.

I want to express my deep gratitude to my daily supervisor and promotor, Claire Chassagne, for granting me the opportunity to pursue my PhD studies under her guidance. Throughout this journey, you have not only imparted invaluable lessons on critical thinking, independence, and structure but also provided support that fueled my research endeavours with passion. Our discussions have been instrumental in enhancing my skills in critical thinking and articulating ideas in a structured manner. Your consistent pres-

ence during challenging times, and active participation in finding solutions, have been invaluable. I would also like to express my gratitude to my co-promotor Alex Kirichek for his supervision and guidance, not only related to my PhD but also various aspects of life in the Netherlands. I would like to thank my committee members for taking the time to review my dissertation and being part of my defence committee.

I extend my gratitude to our industrial partners, including Allseas, Boskalis, Deltares, Royal IHC, and NIOZ, for their involvement in the PLUMEFLOC project. Special thanks to individuals who actively contributed and shared valuable knowledge: Britt Blankenaar, Frans van Grunsven, Henko de Stigter, Laurens de Jonge, Lynyrd de Wit, Mark Biesheuvel, Melanie Diaz, Rudy Helmons, Shaheen Wahab and Wiebe Boomsma. Also, I would like to thank the Mudnet consortium for arranging many academic and recreational activities.

I appreciate the support and assistance from everyone who contributed in any way during my PhD journey. I would also like to thank Clemens Smeenk and Kees Wesdorp for their help with the Dutch translation of the summary. Special mentions to Otti Kievits and Sandra Verkouter from TU Delft for organizational assistance and Saskia Huisman from Deltares for guidance in FCL lab of Deltares.

My heartfelt thanks to current and former colleagues, friends, and fellow researchers at TU and FCL lab Deltares, especially Adarsh Shajimon, Ahmad Shakeel, Alejandra Gijón Mancheño, Ana Colina Alonso, Anna Enge, Arash Sepehri, Atha Bampatzeliou, Chit yan Toe, Clàudia Ylla Arbós, Dolf Enthoven, Fatemeh Chamanmotlagh, Fiorenza Doen, Heng Li, Ismail Myouri, Jan William, Jelle Dercksen, Jianwei Sun, Jill Hanssen, Kifayath Chowdhury, Kshitiz Gautam, Menno Buisman, Mohamed Elerian, Nazeir Elnaker, Patricia Buffon, Pavan Goda, Said Alhaddad, Saghar Ahmadian, Shaheen Wahab, Shelby Ahrendt, Stefano Lovato, Ujala Farooq and Zeinab Safar for making these four years enjoyable. In addition to our work-related discussions, I have consistently relished the times we shared together on numerous occasions.

For four years, I've been in the company of truly brilliant researchers, wonderful individuals, and exceptional engineers and I feel blessed for this. The collaborative endeavours with Ahmad Shakeel, Anne van der Wilk, Celine Taymans, Dolf Enthoven, Louise Delhaye, Mubbasher Nazeer, Shaheen Wahab, and Sjoukje de Lange proved to be highly productive, and I express my gratitude for their contributions. I am also thankful to colleagues from Deltares for the nice discussion and being always welcoming especially Britt Wittekoek, Erik Hendriks, Floris van Rees, Jeroen Ouwerling, Kees Wesdorp, Miguel de Lucas Pardo, Mourad Chalkhane, Stefano Gamberoni and Thijs van Kessel. I have always enjoyed the data analysis discussions with Kees, political discussions with Miguel, investing discussions with Jan William & Clemens Smeek and fitness topics with Britt in Deltares. Engaging in post-work runs was consistently enjoyable and fun with Atha, Britt, Fatemeh, and Ismail.

Students who worked with me, especially Christian de los Santos, Clemens Smeenk, Laurien Korteweg, Vincent Kindermann and Wouter Waasdorp thank you for your commitment and attitude, I learnt a lot from you.

I would like to take this opportunity to thank a few more people without whom my stay in

the Netherlands wouldn't have been the same, thank you Ajay Gautam, Asif Jan, Bilal Khan Yusufi, Haider Sultan, Hassan Azhar, Masood Ahmad, Mubariz Zafar, Mohammad Mohsan, Najeeb Aslam, Qasim Lone, Rai Mujtaba, Samad Shah, Safwan Shurieh. This list would be incomplete if I didn't mention the time I spent with wonderful friends from Enschede (and now scattered in the Netherlands and around the world). Thank you, Adeel Zafar, Ali Asghar, Arka Bhakta, Bharath Kumar, Erik Krammer, Ghazarfar Ali, Ghyoor Gillani, Guillaume Vincent, Hamza Khalid, Iqbal Rasheed, Ismet Baran, Jagadeesh Swamy, Lily Liu, Logendra Dilli, Mohammed Amin Hosseini, Mohammad Irshad, Mohammad Saad Suhail, Onur Yuksel, Owais Ahmad, Ozan Celik, Ozan Erartsin, Ramona Sitohang, Rehman, Sam Benou, Sanjeet Kumar, Senem Aktas, Sikander Naseem Afridi, Tanuj Madaan, Tamoor Mughal, Vanessa Marinosci, Waseem Khan, Yannick Buser, Yash Guha and Zion Moses. In addition, I want to thank my friends Abdul Rehman Basra from Paris and Muhammad Tahir from Nantes for their constant love and support over the years. I find joy in playing cricket and extend my gratitude to my friends from TU and Concordia Club for the wonderful times we've shared together while playing cricket.

I express my gratitude to my two paranymphs, for their assistance during the defence. Your friendship and support throughout the years hold immense significance, and I truly appreciate your presence on this special day.

Lastly, I extend my heartfelt gratitude to my family for their unwavering support and steadfast belief in me. I am truly blessed to be surrounded by such a loving and supportive family. Their kindness and encouragement have been instrumental in my journey, and I am deeply appreciative of their presence in my life.

Waqas Ali
The Hague, April 2024

CURRICULUM VITÆ

Waqas ALI

EDUCATION

2020–2024	PhD. Delft University of Technology, The Netherlands **Thesis:** FLOCCULATION AND DEEP-SEA MINING PLUMES **Promotor** Dr. C. Chassagne **Co-Promotor** Dr. A. Kirichek
2015–2016	Masters in Environmental Fluid Mechanics University Grenoble Alpes, Grenoble, France
2012–2014	Masters in Mathematics International Islamic University Islamabad, Pakistan

EXPERIENCE

2016–2020	Researcher University of Twente, The Netherlands
2013–2014	Mathematics Lecturer Govt. Graduate College, Satellite Town, Rawalpindi, Pakistan

List of Publications

Journal publications

1. **W. Ali**, A. Kirichek, C. Chassagne *Natural flocculation of deep-sea clay from Clarion Clipperton fracture zone*, Under review Applied Ocean Research (2024).

2. **W. Ali**, A. Kirichek, C. Chassagne *Collective effects on the settling of clay flocs*, Under review Applied Clay Science (2024).

3. S.I. de Lange, A. van der Wilk, C. Chassagne, **W. Ali**, T. Hoitink, M. P. Born, K. Brodersen, H. Schuttrumpf, K. Waldschläger *Migrating subaqueous dunes capture clay flocs*, Under review Nature Communications (2024).

4. S.A. Wahab, **W. Ali**, C. Chassagne, R.L.J. Helmons *Role of Organic Matter present in the Water Column on Turbidity flows*, In Preparation (2024).

5. **W. Ali**, D. Enthoven, A. Kirichek, R. Helmons, C. Chassagne *Effect of flocculation on turbidity currents*, Front. Earth Sci. 10:1014170. (2022).

6. **W. Ali**, C. Chassagne *Comparison between two analytical models to study the flocculation of mineral clay by polyelectrolytes*, Continental Shelf Research, Volume 250, 104864, ISSN 0278-4343, (2022).

7. A. Shakeel, **W. Ali**, C. Chassagne, A. Kirichek *The rheological properties of kaolinite suspensions in the presence of different biopolymers*, Colloids and Surfaces A: Physicochemical and Engineering Aspects (2022).

Oral and Poster Presentations and Conference papers

1. **W. Ali**, A. Kirichek, R. Helmons, C. Chassagne. Bridging the depths: lessons from deep-sea mining for better predicting turbidity plumes, **CEDA Dredging Days 2024**, Rotterdam, Netherlands, 27 – 29 May, 2024.

2. S.I. de Lange, A. van der Wilk, C. Chassagne, **W. Ali**, T. Hoitink, M. P. Born, K. Brodersen, H. Schuttrumpf, K. Waldschläger. The capturing of flocs by migrating subaqueous dunes, **EGU**, Vienna, Austria & Online, 14–19 April, 2024.

3. **W. Ali**, A. Kirichek, A.J. Manning, C. Chassagne. Comparison between two Techniques for Floc analysis, **AGU Fall Meeting**, San Francisco, CA, USA, 11 – 15 December, 2023.

4. **W. Ali**, A. Kirichek, C. Chassagne. Potential of Natural Flocculation in Reduction of Deep Sea Mining Plumes, **Underwater Minerals Conference**, Rotterdam, Netherlands, 1 – 6 October, 2023.

5. **W. Ali**, A. Kirichek, C. Chassagne. Measuring the settling velocity of flocs, **AGU Fall Meeting**, Chicago, IL, USA, 12 – 16 December, 2022.

6. **W. Ali**, A. Shakeel, D. Enthoven, A. Kirichek, R. Helmons, C. Chassagne. Yield stress and floc size of sediment collected from lock exchange experiments, **AGU Fall Meeting**, Chicago, IL, USA, 12 − 16 December, 2022.

7. **W. Ali**, D. Enthoven, A. Kirichek, R. Helmons, C. Chassagne. Can Flocculation Reduce the Dispersion of Deep Sea Sediment Plumes?, **WODCON XXIII Conference**, Copenhagen, Denmark, 16 − 20 May, 2022.

8. **W. Ali**, C. Chassagne. Flocculation study with the help of a model based on logistic growth theory, **INTERCOH Conference**, Delft, the Netherlands, 13 − 17 September, 2021.

9. **W. Ali**, A. Kirichek, C. Chassagne. Potential of bio flocculant for flocculating deep sea mining plumes, **MudNet Conference**, Delft, the Netherlands, 29 − 30 March, 2021.